Uenzelmann-Neben, G., Bohaty, S.M., Childress, L.B., and the Expedition 392 Scientists
Proceedings of the International Ocean Discovery Program Volume 392
publications.iodp.org

Site U1580[1]

Keywords
International Ocean Discovery Program, IODP, *JOIDES Resolution*, Expedition 392, Agulhas Plateau Cretaceous Climate, Climate and Ocean change, Earth Connections, Site U1580, Cretaceous/Paleogene boundary, K/Pg boundary, Paleocene/Eocene Thermal Maximum, PETM, large igneous province, LIP, zeolite authigenesis, igneous sill intrusion, Campanian, Oligocene pelagic carbonates, paleoceanography, African–Southern Ocean gateway

Core descriptions

Supplementary material

References (RIS)

MS 392-104
Published 19 August 2023

Funded by NSF OCE1326927

S.M. Bohaty, G. Uenzelmann-Neben, L.B. Childress, O.A. Archontikis, S.J. Batenburg, P.K. Bijl, A.M. Burkett, H.C. Cawthra, P. Chanda, J.J. Coenen, E. Dallanave, P.C. Davidson, K.E. Doiron, J. Geldmacher, D. Gürer, S.J. Haynes, J.O. Herrle, Y. Ichiyama, D. Jana, M.M. Jones, C. Kato, D.K. Kulhanek, J. Li, J. Liu, J. McManus, A.N. Minakov, D.E. Penman, C.J. Sprain, A.C. Tessin, T. Wagner, and T. Westerhold[2]

[1] Bohaty, S.M., Uenzelmann-Neben, G., Childress, L.B., Archontikis, O.A., Batenburg, S.J., Bijl, P.K., Burkett, A.M., Cawthra, H.C., Chanda, P., Coenen, J.J., Dallanave, E., Davidson, P.C., Doiron, K.E., Geldmacher, J., Gürer, D., Haynes, S.J., Herrle, J.O., Ichiyama, Y., Jana, D., Jones, M.M., Kato, C., Kulhanek, D.K., Li, J., Liu, J., McManus, J., Minakov, A.N., Penman, D.E., Sprain, C.J., Tessin, A.C., Wagner, T., and Westerhold, T., 2023. Site U1580. In Uenzelmann-Neben, G., Bohaty, S.M., Childress, L.B., and the Expedition 392 Scientists, Agulhas Plateau Cretaceous Climate. Proceedings of the International Ocean Discovery Program, 392: College Station, TX (International Ocean Discovery Program). https://doi.org/10.14379/iodp.proc.392.104.2023
[2] **Expedition 392 Scientists' affiliations.**

1. Background and objectives

Site U1580 is located on the southern central Agulhas Plateau (40°47.1535′S, 26°36.4137′E) at 2560 m water depth. The site lies about 100 km southeast of Site U1579. Bathymetric data show Site U1580 to be located on the flank of a bathymetric high that is underlain by a number of basement highs, as revealed by seismic data. A rugged topography characterizes the top of the interpreted basement. Below this horizon, reflections have been observed dipping away from the basement highs in all directions. The basement highs have thus been interpreted as extrusion centers. The seismic data show a chaotic layer topped by green Reflector M with a strong reflection amplitude. Another strong seismic horizon, Reflector LE, can be observed (magenta, Figure F1). Both Reflec-

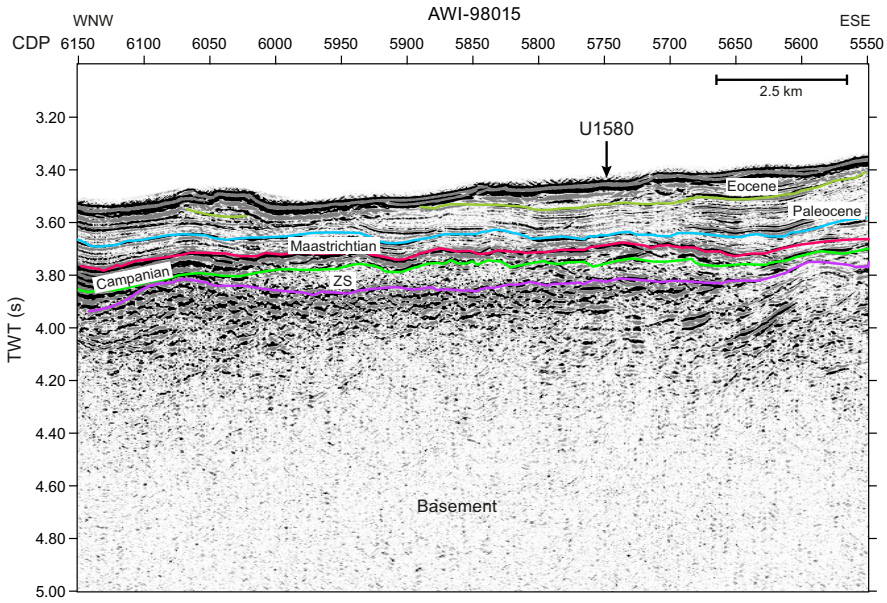

Figure F1. Seismic Line AWI-98015 showing Site U1580. Preliminary interpretation of seismic units according to the drilled lithologic units is shown. The marked bright green reflection corresponds in structure to Reflector M of the precruise seismostratigraphic model (see Figure F4 in the Expedition 392 summary chapter [Uenzelmann-Neben et al., 2023b]), the magenta reflection to Reflector LE, and the blue reflection to Reflector LO. CDP = common depth point, TWT = two-way traveltime. ZS = zeolitic silicified sediments.

tors M and LE follow the basement topography. The sequence above Reflector LE shows parallel to subparallel continuous reflections of middle to strong amplitude. The youngest part of this sequence is affected by erosion at the seafloor (Figure **F1**).

Site U1580 was chosen to recover both Cretaceous and Paleogene sedimentary records and basement samples. This site was especially dedicated to recovering an extended record of basement material to unravel the nature of the basement and provide information on its formation age. Potential late-stage magmatism and its effect on sedimentary sequences and the environment were additional objectives. Integration of seismic profiles with the drilling results will allow direct dating of the observed Seismic Unconformities M and LE and interpreting their causes, and recovery of the sediment/basement interface will provide information on the age of the oldest sediments above the basement as well as the water depth and environment at the time of deposition. At this site, a sediment sequence from the mid-Cretaceous to mid-Paleogene was expected to be drilled, spanning the long-term climate transition from the Cretaceous greenhouse to the mid-Paleogene icehouse. Critical intervals of ocean–climate transitions such as the Eocene–Oligocene transition (EOT), the Paleocene/Eocene Thermal Maximum (PETM), the Cretaceous/Paleogene (K/Pg) boundary, and Oceanic Anoxic Events (OAEs) 2 and 3 were expected to be documented in the sedimentary record. The nature and age of the basement would also be unraveled by drilling at this site.

2. Operations

Site U1580 hole locations, water depths, and the number of cores recovered are listed in Table **T1**. All times are provided in local ship time (UTC + 2 h).

2.1. Hole U1580A

The 53 nmi transit from Site U1579 concluded with the arrival at Site U1580 at 1306 h on 25 February 2022. The thrusters were lowered, and the vessel switched from cruise mode to dynamic positioning (DP) mode at 1326 h. The bottom-hole assembly (BHA) was assembled, and the pipe was tripped to the seafloor, tagging at 2560.3 meters below sea level (mbsl). Hole U1580A was spudded, and Core 1R was recovered at 2015 h (recovery = 6.82 m). For the next several days, rotary core barrel (RCB) coring continued through Core 42R, advancing from 9.7 to 407.4 m core depth below seafloor, Method A (CSF-A), and recovering 250.38 m (63%).

At ~1700 h on 1 March, the rate of penetration (ROP) for Core 392-U1580A-43R slowed to almost zero and no noticeable progress was being made. The core was pulled at the 2 h mark with an advance of only 0.2 m and recovery of only a few cobbles (0.15 m). Core 44R was also cut by time (2 h), and the 1.0 m advance resulted in no recovery. The bit deplugger (a core barrel with a pointed metal tip) was dropped twice in an attempt to clear any material blocking the bit. Core 45R then advanced 3.2 m and recovered 3.25 m. It was determined from recovered pieces that a chert layer of loosened rock was slowing ROP and preventing recovery.

The sediment/basalt contact was difficult to determine based on coring parameters, likely due to multiple chert/silicified horizons in the sediments immediately overlying the basalts that resulted in very low overall ROP. Although core recovery was low, pieces of basalt were recovered in Cores 392-U1580A-43R and 45R. A good basalt contact was cored at ~419–420 m CSF-A in Core 47R on 2 March. The ROP was 1.0 m/h for Cores 47R–49R. Coring continued until 1630 h on 5 March with Core 68R at a final depth of 533.9 m CSF-A. The basalt below ~495 m CSF-A was cored with good recovery at an ROP of 3–5 m/h, which is very fast for hard rock. The overall ROP for RCB coring in Hole U1580A was 4.4 m/h.

At 1630 h on 5 March, the driller pumped a final sweep to clean the hole, flushing the mud completely out of the hole. The mechanical bit release was lowered, and the bit was dropped at 1715 h. A few words of respect were said to honor the bit's courage and fortitude. The bit had 120.3 h overall drilling time, ~58.8 m of which was in hard rock.

Table T1. Core summary, Site U1580. DRF = drilling depth below rig floor, DSF = drilling depth below seafloor. APC = advanced piston corer, HLAPC = half-length APC, XCB = extended core barrel. R = RCB. (Continued on next page.) **Download table in CSV format.**

Hole U1580A
Latitude: 40°47.1535′S
Longitude: 26°36.4137′E
Water depth (m): 2560.33
Date started (UTC): 1130 h; 25 Feb 2022
Date finished (UTC): 0500 h; 07 Mar 2022
Time on hole (days): 9.73
Seafloor depth DRF (m): 2571.5
Seafloor depth est. method: Tag
Rig floor to sea level (m): 11.17
Penetration DSF (m): 533.9
Cored interval (m): 533.9
Recovered length (m): 351.03
Recovery (%): 66
Drilled interval (m): NA
Drilled interval (no.): 0
Total cores (no.): 68
APC cores (no.): 0
HLAPC cores (no.): 0
XCB cores (no.): 0
RCB cores (no.): 68
Other cores (no.): 0

Hole U1580B
Latitude: 40°47.1542′S
Longitude: 26°36.4282′E
Water depth (m): 2560.33
Date started (UTC): 0500 h; 07 Mar 2022
Date finished (UTC): 1230 h; 08 Mar 2022
Time on hole (days): 1.31
Seafloor depth DRF (m): 2571.5
Seafloor depth est. method: Offset
Rig floor to sea level (m): 11.17
Penetration DSF (m): 77.8
Cored interval (m): 37.8
Recovered length (m): 23.78
Recovery (%): 63
Drilled interval (m): 40
Drilled interval (no.): 1
Total cores (no.): 4
APC cores (no.): 0
HLAPC cores (no.): 0
XCB cores (no.): 0
RCB cores (no.): 4
Other cores (no.): 0

Core	Top depth drilled DSF (m)	Bottom depth drilled DSF (m)	Interval advanced (m)	Recovered length (m)	Curated length (m)	Core recovery (%)	Core on deck date (2022)	Core on deck time UTC (h)	Sections (*N*)
392-U1580A-									
1R	0.0	9.7	9.7	6.82	6.82	70	25 Feb	1935	6
2R	9.7	19.4	9.7	7.08	7.08	73	25 Feb	2130	6
3R	19.4	29.1	9.7	4.25	4.25	44	25 Feb	2345	4
4R	29.1	38.8	9.7	8.11	8.11	84	26 Feb	0200	7
5R	38.8	48.5	9.7	6.74	6.74	69	26 Feb	0430	6
6R	48.5	58.2	9.7	7.03	7.03	72	26 Feb	0655	6
7R	58.2	67.9	9.7	7.89	7.89	81	26 Feb	0915	7
8R	67.9	77.6	9.7	4.92	4.92	51	26 Feb	1130	5
9R	77.6	87.3	9.7	10.02	10.02	103	26 Feb	1345	8
10R	87.3	97.0	9.7	4.71	4.71	49	26 Feb	1555	5
11R	97.0	106.7	9.7	0.23	0.23	2	26 Feb	1730	1
12R	106.7	116.4	9.7	5.45	5.45	56	26 Feb	2015	5
13R	116.4	126.1	9.7	5.50	5.50	57	26 Feb	2325	5
14R	126.1	135.8	9.7	3.22	3.22	33	27 Feb	0250	4
15R	135.8	145.5	9.7	3.01	3.01	31	27 Feb	0530	3
16R	145.5	155.2	9.7	2.37	2.37	24	27 Feb	0655	3
17R	155.2	164.9	9.7	3.92	3.92	40	27 Feb	0815	4
18R	164.9	174.6	9.7	8.29	8.29	85	27 Feb	1000	7
19R	174.6	184.3	9.7	2.73	2.73	28	27 Feb	1130	3
20R	184.3	194.0	9.7	3.51	3.51	36	27 Feb	1330	4
21R	194.0	203.7	9.7	8.17	8.17	84	27 Feb	1530	7
22R	203.7	213.4	9.7	9.34	9.34	96	27 Feb	1720	8
23R	213.4	223.1	9.7	4.20	4.20	43	27 Feb	1945	4
24R	223.1	232.8	9.7	4.65	4.65	48	27 Feb	2135	5
25R	232.8	242.5	9.7	2.74	2.74	28	27 Feb	2330	3
26R	242.5	252.2	9.7	3.51	3.51	36	28 Feb	0140	4
27R	252.2	261.9	9.7	3.99	3.99	41	28 Feb	0405	4
28R	261.9	271.6	9.7	5.89	5.89	61	28 Feb	0630	5
29R	271.6	281.3	9.7	8.74	8.74	90	28 Feb	0940	7
30R	281.3	291.0	9.7	4.49	4.49	46	28 Feb	1205	5
31R	291.0	300.7	9.7	9.83	9.83	101	28 Feb	1340	8
32R	300.7	310.4	9.7	9.42	9.42	97	28 Feb	1520	8
33R	310.4	320.1	9.7	6.29	6.29	65	28 Feb	1630	5
34R	320.1	329.8	9.7	10.07	10.07	104	28 Feb	1810	9
35R	329.8	339.5	9.7	9.63	9.63	99	28 Feb	1935	8
36R	339.5	349.2	9.7	8.15	8.15	84	28 Feb	2100	7
37R	349.2	358.9	9.7	10.17	10.17	105	28 Feb	2240	8
38R	358.9	368.6	9.7	8.40	8.40	87	1 Mar	0110	8
39R	368.6	378.3	9.7	8.94	8.94	92	1 Mar	0355	8
40R	378.3	388.0	9.7	8.56	8.56	88	1 Mar	0740	7
41R	388.0	397.7	9.7	1.33	1.33	14	1 Mar	1105	2
42R	397.7	407.4	9.7	4.89	4.89	50	1 Mar	1435	5
43R	407.4	407.6	0.2	0.15	0.15	75	1 Mar	1800	1
44R	407.6	408.6	1.0	0.00	0.00	0	1 Mar	2115	0

Table T1 (continued).

Core	Top depth drilled DSF (m)	Bottom depth drilled DSF (m)	Interval advanced (m)	Recovered length (m)	Curated length (m)	Core recovery (%)	Core on deck date (2022)	Core on deck time UTC (h)	Sections (*N*)
45R	408.6	411.8	3.2	3.25	3.29	102	2 Mar	0245	3
46R	411.8	417.6	5.8	1.50	1.50	26	2 Mar	0905	2
47R	417.6	422.4	4.8	1.95	1.97	41	2 Mar	1505	2
48R	422.4	427.2	4.8	6.73	7.05	139	2 Mar	2125	6
49R	427.2	432.1	4.9	4.09	4.19	83	3 Mar	0305	4
50R	432.1	436.9	4.8	5.27	5.48	110	3 Mar	1110	5
51R	436.9	441.8	4.9	2.52	2.63	51	3 Mar	1505	3
52R	441.8	446.6	4.8	4.61	4.78	96	3 Mar	1915	4
53R	446.6	451.5	4.9	6.21	6.67	127	3 Mar	2240	5
54R	451.5	456.3	4.8	3.46	3.50	72	4 Mar	0120	3
55R	456.3	461.2	4.9	4.77	5.00	97	4 Mar	0405	5
56R	461.2	466.0	4.8	5.39	5.72	112	4 Mar	0810	5
57R	466.0	470.9	4.9	1.24	1.24	25	4 Mar	0950	2
58R	470.9	475.8	4.9	1.57	1.59	32	4 Mar	1230	2
59R	475.8	480.6	4.8	2.77	2.91	58	4 Mar	1430	3
60R	480.6	485.4	4.8	1.17	1.17	24	4 Mar	1610	2
61R	485.4	490.3	4.9	1.04	1.04	21	4 Mar	1750	2
62R	490.3	495.1	4.8	2.41	2.39	50	4 Mar	2030	2
63R	495.1	500.0	4.9	6.59	6.69	134	4 Mar	2320	6
64R	500.0	504.8	4.8	4.15	4.21	86	5 Mar	0150	4
65R	504.8	509.7	4.9	2.55	2.63	52	5 Mar	0430	2
66R	509.7	514.5	4.8	6.35	6.79	132	5 Mar	0810	5
67R	514.5	524.2	9.7	9.98	10.24	103	5 Mar	1140	8
68R	524.2	533.9	9.7	4.11	4.38	42	5 Mar	1435	4
		Hole U1580A totals:	533.9	351.03	354.41				324
392-U1580B-									
11	0.0	40.0	40.0	*****Drilled interval*****			7 Mar	1920	0
2R	40.0	48.7	8.7	7.52	7.52	86	7 Mar	2100	6
3R	48.7	58.4	9.7	4.82	4.82	50	7 Mar	2330	5
4R	58.4	68.1	9.7	5.40	5.40	56	8 Mar	0150	6
5R	68.1	77.8	9.7	6.04	6.04	62	8 Mar	0400	5
		Hole U1580B totals:	77.8	23.78	23.78				22
		Site U1580 totals:	611.7	374.81	378.19				346

The drill string was tripped up to 80.7 m CSF-A in preparation for downhole logging. At 2145 h, the triple combination (triple combo) tool string was assembled. It consisted of the Hostile Environment Natural Gamma Ray Sonde (HNGS), Hostile Environment Litho-Density Sonde (HLDS), and Magnetic Susceptibility Sonde (MSS). The tools were run into Hole U1580A starting at 2330 h. The triple combo continued downlogging to 524.2 m wireline log depth below seafloor (WSF). The logging run was completed, and the tool string was out of the hole at 0630 h on 6 March. For the next downhole logging run, the Formation MicroScanner (FMS)-sonic tool string was assembled and deployed at 0900 h. It consisted of the Dipole Shear Sonic Imager (DSI) and FMS. Two passes were conducted, and both tools tagged the bottom of the hole at ~521.5 m WSF. The tools were back at the surface at 1535 h. For the final downhole logging run, the Ultrasonic Borehole Imager (UBI) tool string was made up; it consisted of the General Purpose Inclinometry Tool (GPIT) and UBI.

The UBI tool string was run in the hole beginning at 1610 h. One pass was completed to 504.5 m WSF. The second pass was aborted after difficulties with the tool, and it was later determined that the transducer subassembly motor was sticking. The UBI logging run was completed, and the tools were back on the rig floor at 0020 h on 7 March. The pipe was then tripped out, clearing the seafloor at 0150 h and the rig floor at 0705 h, ending Hole U1580A. RCB coring averaged 4.4 m/h overall ROP with rates less than 1.0 m/h at times. A total of 68 cores were taken in Hole U1580A over a 533.9 m interval (recovery = 65.7%). Total time on Hole U1580A was 233.52 h (9.73 days).

2.2. Hole U1580B

A new C-4 RCB bit was prepared, and the BHA was run to 172.1 meters below rig floor (mbrf) before damage to the drilling line was observed in a routine inspection. The line was slipped and cut (150 ft), and on 7 March 2022 the pipe trip resumed and the drill pipe was lowered to near the

seafloor before the vessel completed the 20 m east offset. An RCB core barrel was installed with a center bit, and Hole U1580B was spudded at 1710 h from a seafloor depth of 2571.5 mbrf. The hole was drilled to 40.0 m CSF-A, where the center bit was retrieved, and coring commenced with Core 2R. RCB coring continued through Core 5R to the final depth of 77.8 m CSF-A at 0615 h on 8 March. We then began tripping the pipe back to the vessel, clearing the seafloor at 0710 h and the rig floor at 1430 h, ending Hole U1580B. The rig floor was secured for transit, the thrusters were raised, and the transit to Site U1581 began at 1524 h. The ROP for RCB coring averaged 7.2 m/h, and the 40 m drill down averaged 14.6 m/h. A total of four cores were taken in Hole U1580B over a 37.8 m interval (recovery = 62.9%). Total time on Hole U1580B was 31.44 h (1.31 days).

3. Lithostratigraphy

Site U1580 consists of a 528.58 m sequence of calcareous and siliciclastic sediments that are interbedded with basalt in the lowermost ~130 m of the sequence. Lithostratigraphic unit and subunit boundaries are largely defined using macroscopic core descriptions and smear slides, which are supplemented by X-ray diffraction (XRD) analyses, portable X-ray fluorescence (pXRF) spectrometer analyses, physical properties (see **Physical properties**), and geochemical data (see **Geochemistry**). The sequence recovered at Site U1580 is divided into fourteen lithostratigraphic units, and Lithostratigraphic Units II and III are divided into five subunits (IIa–IIc, IIIa, and IIIb) (Table **T2**). Lithostratigraphic Units I–III, V, VII, IX, XI, and XIII are largely composed of calcareous chalks and siliciclastic sandstones, siltstones, and claystones (Figures **F2**, **F3**, **F4**, **F5**), whereas Lithostratigraphic Units IV, VI, VIII, X, XII, and XIV are basalt (see **Igneous petrology**). In the lowermost ~50 m of Hole U1580A, there are several occurrences of likely out of place basalt fragments in otherwise sedimentary units or sedimentary rock fragments in otherwise basaltic units, which are interpreted as fall-in material. The fragments are deemed to be fall-in if (1) the fragments occur at core breaks, (2) the fragments are composed of material that is recognizable as occurring in an overlying unit, (3) there are no preserved contacts between the fragments and adjacent units above or below, and (4) the diameter of the fragment is <6 cm (i.e., narrower than the internal diameter of the core liner). Occurrences of fall-in are not classified as distinct units but are instead noted in the broader units in which they were observed. Postcruise integration of core descriptions and logging data may help refine the true stratigraphic placement of the sedimentary and basalt sections.

3.1. Lithostratigraphic Unit I

Interval: 392-U1580A-1R-1, 0 cm, to 1R-3, 112 cm
Depth: 0.00–3.42 m CSF-A (0.00–3.42 m core composite depth below seafloor [CCSF])
Age: Pleistocene
Major lithologies: foraminiferal ooze with nannofossils

Lithostratigraphic Unit I is 3.42 m thick and characterized by light gray to light brown foraminiferal ooze with nannofossils (Figures **F3**, **F6**). There are dark sand-sized grains of pyrite and glauconite throughout the unit. The lithology of this unit at Site U1580 is similar to that of Lithostratigraphic Unit I at Site U1579 (see **Lithostratigraphy** in the Site U1579 chapter [Bohaty et al., 2023]). Bedding is massive, and drilling disturbance has resulted in a soupy to mousse-like texture throughout most of the unit. The upper contact of Lithostratigraphic Unit I in Hole U1580A (Section 392-U1580A-1R-1, 0 cm) is placed at the seafloor, and the lower contact with Lithostratigraphic Unit II is marked by a lithologic change from light brown foraminiferal ooze above to white nannofossil ooze below in Section 1R-3, 112 cm (3.42 m CSF-A). The contact, however, is severely deformed by drilling disturbance.

3.2. Lithostratigraphic Unit II

Interval: 392-U1580A-1R-3, 112 cm, to 31R-2, 102 cm
Depth: 3.42–293.51 m CSF-A (3.43–293.51 m CCSF)
Age: lower Eocene to Campanian
Major lithologies: nannofossil ooze with foraminifera, nannofossil chalk and clayey calcareous chalk

Lithostratigraphic Unit II is a ~290 m thick sequence of Eocene–Campanian nannofossil oozes and chalks that is divided into three subunits (IIa–IIc). In Section 392-U1580A-31R-2 (293.51 m CSF-A), the Lithostratigraphic Unit II/III contact is marked by a gradational change from reddish white calcareous chalk to green zeolitic siliciclastic sediments, as well as a notable decrease in carbonate content from >80 wt% $CaCO_3$ in the upper part of Lithostratigraphic Unit II to <10 wt% $CaCO_3$ at ~294 m CSF-A (Figure **F2**).

3.2.1. Lithostratigraphic Subunit IIa

Interval: 392-U1580A-1R-3, 112 cm, to 2R-CC, 19 cm
Depth: 3.42–16.73 m CSF-A (3.43–16.73 m CCSF)
Age: lower Eocene
Major lithologies: nannofossil ooze with foraminifera

Lithostratigraphic Subunit IIa is 13.31 m thick and characterized by massively bedded white or pale yellow to light greenish gray nannofossil ooze (Figure **F3**). Finely disseminated framboidal pyrite is present in low abundance throughout the unit. Clay, volcanic glass, radiolarians, foraminifera, and glauconite are occasionally present in smear slides (Figures **F6**, **F7**). Foraminifera are rare to common throughout Lithostratigraphic Subunit IIa. Carbonate content is typically ~75–80

Table T2. Lithostratigraphic unit and subunit boundaries, Site U1580. **Download table in CSV format.**

Lith. unit	Generalized lithology	Hole U1580A Depth CSF-A (m)	Depth CCSF (m)	Core, section, interval (cm)
				392-U1580A-
I	Foraminiferal ooze with nannofossils	0.00–3.42	0.00–3.42	1R-1, 0, to 1R-3, 112
IIa	Nannofossil ooze with foraminifera	3.42–16.73	3.42–16.73	1R-3, 112, to 2R-CC, 19
IIb	Nannofossil chalk	19.40–207.11	19.40–207.11	3R-1, 0, to 22R-3, 59
IIc	Clayey calcareous chalk	207.11–293.51	207.11–293.51	22R-3, 59, to 31R-2,102
IIIa	Green zeolitic sandstone/siltstone/claystone with glauconite	293.51–349.975	293.51–349.975	31R-2,102, to 37R-1, 77.5
IIIb	Light to dark green glauconitic siltstone and sandstone, and light green calcareous chalk	349.975–407.46	349.975–407.46	37R-1, 77.5, to 43R-CC, 6
IV	Basalt	407.46–411.76	407.46–411.76	43R-CC, 6, to 45R-3, 64
V	Silicified limestone, calcareous siltstone, and chert	411.76–412.82	411.76–413.16	45R-3, 64, to 46R-1, 102
VI	Basalt	412.82–426.25	413.16–423.78	46R-1, 102, to 48R-4, 66
VII	Calcareous limestone	426.25–426.27	423.78–423.80	48R-4, 66, to 48R-4, 68
VIII	Basalt	426.27–438.97	423.80–439.90	48R-4, 68, to 51R-2, 67
IX	Chert	438.97–439.49	439.90–440.42	51R-3, 0, to 51R-3, 52
X	Basalt	439.49–466.63	440.42–467.09	51R-3, 52, to 56R-4, 142
XI	Calcareous chalk, silicified limestone, and nannofossil-rich claystone	466.63–471.60	467.09–471.60	56R-5, 0, to 58R-1, 70
XII	Basalt	471.60–478.53	471.60–478.53	58R-1, 70, to 59R-2, 123
XIII	Calcareous chalk, claystone, siltstone, and rubbles of basalt	478.53–490.54	478.53–490.54	59R-CC, 0, to 62R-1, 24
XIV	Basalt	490.54–528.58	490.54–529.59	62R-1, 24, to 68R-4, 31

Lith. unit	Generalized lithology	Hole U1580B Depth CSF-A (m)	Depth CCSF (m)	Core, section, interval (cm)
				392-U1580B-
I	Foraminiferal ooze with nannofossils			
IIa	Nannofossil ooze with foraminifera			
IIb	Nannofossil chalk	40.00–74.10		2R-1, 0, to 5R-CC, 19
IIc	Clayey calcareous chalk			
IIIa	Green zeolitic sandstone/siltstone/claystone with glauconite			
IIIb	Light to dark green glauconitic siltstone and sandstone, and light green calcareous chalk			
IV	Basalt			
V	Silicified limestone, calcareous siltstone, and chert			
VI	Basalt			
VII	Calcareous limestone			
VIII	Basalt			
IX	Chert			
X	Basalt			
XI	Calcareous chalk, silicified limestone, and nannofossil-rich claystone			
XII	Basalt			
XIII	Calcareous chalk, claystone, siltstone, and rubbles of basalt			
XIV	Basalt			

wt% throughout (Figure **F2**). The Lithostratigraphic Subunit IIa/IIb contact, representing the ooze to chalk transition, was not recovered.

3.2.2. Lithostratigraphic Subunit IIb

Intervals: 392-U1580A-3R-1, 0 cm, to 22R-3, 59 cm; 392-U1580B-2R-1, 0 cm, to 5R-CC, 19 cm
Depths: Hole U1580A = 19.40–207.11 m CSF-A (19.40–207.11 m CCSF); Hole U1580B = 40.00–74.10 m CSF-A
Age: Eocene to lower Paleocene
Major lithologies: nannofossil chalk

Lithostratigraphic Subunit IIb consists of ~188 m of white to light greenish gray nannofossil chalk, sometimes with clay (Figure **F3**), and shares many characteristics with Lithostratigraphic Subunit IIb recovered at Site U1579 (see **Lithostratigraphy** in the Site U1579 chapter [Bohaty et al., 2023]). Lithostratigraphic Subunit IIb is chalk, whereas Lithostratigraphic Subunit IIa is ooze. In general, Lithostratigraphic Subunit IIb also has higher carbonate content than Lithostratigraphic Subunit IIa; it gradually increases downcore from ~80–85 to ~90–95 wt% at ~150 m CSF-A (Figure **F2**). Carbonate content is more variable between ~150 and 207 m CSF-A (bottom of Lithostratigraphic Subunit IIb), which correlates with a gradual increase in clay abundance (Figures **F2**, **F7**). This subunit is moderately to highly bioturbated, with occasional *Planolites* burrows and common *Zoophycos* burrows. Faint mottles of gray/black pyrite are observed throughout. The Lithostratigraphic Subunit IIb/IIc contact is placed within a bioturbated horizon in Section 392-U1580A-22R-3, 59 cm (207.11 m CSF-A).

The Paleocene/Eocene boundary was recovered in Sections 392-U1580A-7R-4 (~63 m CSF-A) and 392-U1580B-4R-4 (~62 m CSF-A). In these sections, light greenish gray nannofossil chalk progressively darkens downcore to greenish gray nannofossil chalk with clay over ~50 cm, culminating with the darkest sediment occurring immediately above the boundary in Sections 392-U1580A-7R-4, 61.5 cm, and 392-U1580B-4R-4, 49 cm (Figure **F8**). The upper greenish gray sedi-

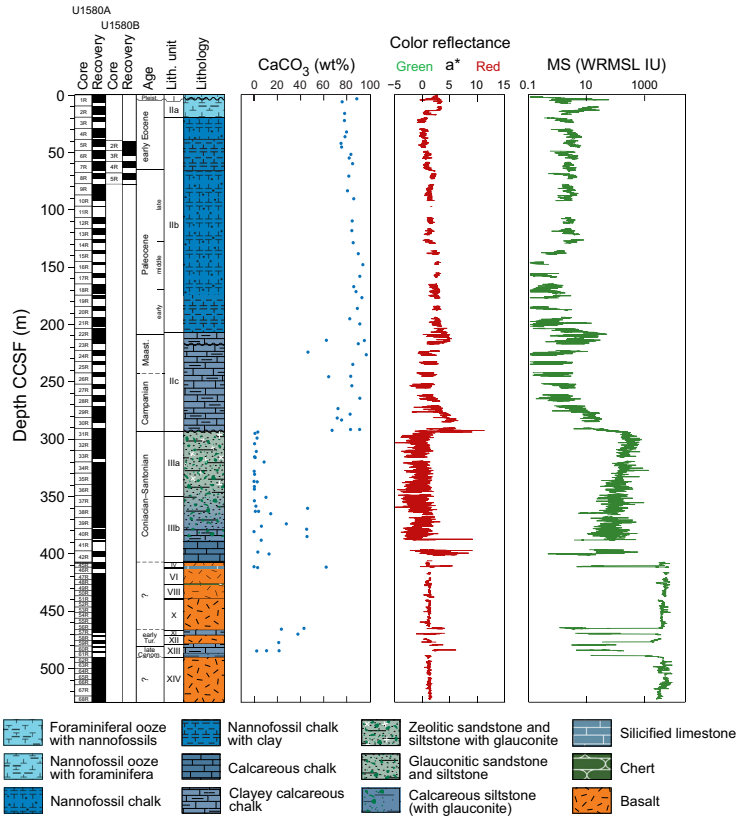

Figure F2. Lithostratigraphic summary, Site U1580.

ment interval overlies white nannofossil chalk immediately below the boundary, which is as thick as 10 cm in Hole U1580A and ~30 cm thick in Hole U1580B, before gradually transitioning downcore into nannofossil chalk with clay. In both holes, the contact between greenish gray chalk and white chalk is bioturbated and the burrows below the contact are infilled with dark material.

3.2.3. Lithostratigraphic Subunit IIc

Interval: 392-U1580A-22R-3, 59 cm, to 31R-2, 102 cm
Depth: 207.11–293.51 m CSF-A (207.11–293.51 m CCSF)
Age: lower Paleocene to Campanian
Major lithologies: clayey calcareous chalk

Lithostratigraphic Subunit IIc is 86.40 m thick and consists of light greenish gray calcareous chalk with cyclic bands of greenish gray or reddish brown clayey calcareous chalk with a downcore increase in chert abundance (Figure **F3**). Consistent with Site U1579, the Lithostratigraphic Subunit IIb/IIIc boundary at this site is defined by an increase in magnetic susceptibility (MS) and natural gamma radiation (NGR) from ~200 to 220 m CSF-A (Figure **F2**) (see **Physical properties**). Carbonate content in Lithostratigraphic Subunit IIc is generally high (~80%–95%); however, it is more variable between samples than in Lithostratigraphic Subunits IIa and IIb, which likely reflects lower carbonate content in the brown and green clay-rich intervals (Figure **F2**). Bulk sediment XRD analysis from Lithostratigraphic Subunit IIc (Sample 392-U1580A-31R-1, 84–86 cm) confirms that calcite is the dominant mineral in this unit, with trace amounts of interstratified clay (Figure **F9**). In Sections 27R-1 and 27R-2 (252.79–253.87 m CSF-A), there are out of place angular clasts of white calcareous clay in a matrix of greenish gray calcareous chalk that suggest this interval is a mass transport deposit (Figure **F10**).

Based on the microfossil biostratigraphy (see **Micropaleontology**), the K/Pg boundary occurs in Lithostratigraphic Subunit IIc between Sections 392-U1580A-22R-3, 55 cm (207.10 m CSF-A), and 22R-4, 135 cm (209.25 m CSF-A), which is an intensely bioturbated interval of alternating bands of darker reddish brown clayey nannofossil chalk and lighter greenish gray nannofossil

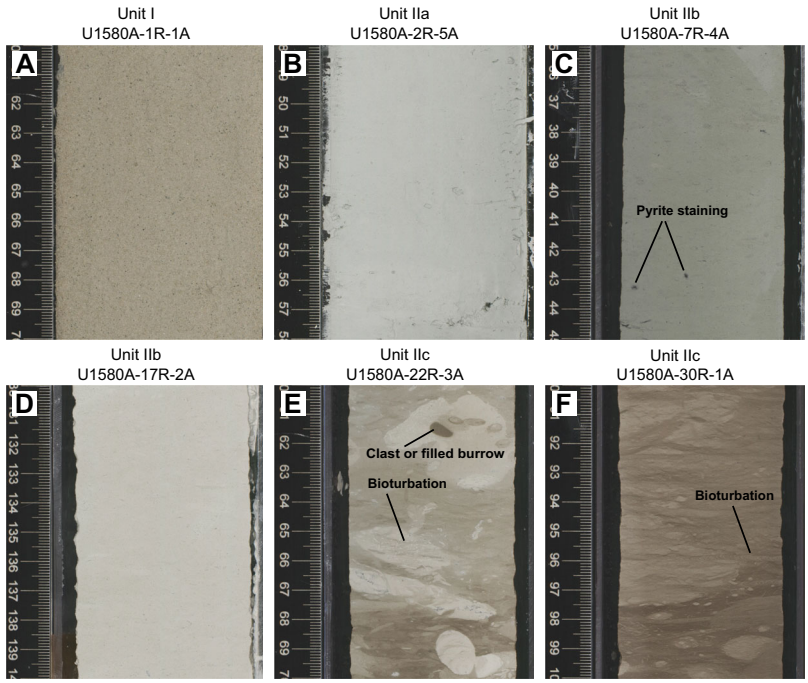

Figure F3. Major lithologies of Lithostratigraphic Units I and II, Hole U1580A. A. Foraminiferal ooze with nannofossils (1R-1, 60–70 cm). B. Nannofossil ooze with foraminifera (2R-5, 48–58 cm). C. Nannofossil chalk with clay (7R-4, 35–45 cm). D. Nannofossil chalk (17R-2, 130–140 cm). E. Reddish brown nannofossil chalk with clay (22R-3, 60–70 cm). F. A highly bioturbated interval of reddish brown clayey calcareous chalk with *Zoophycos* traces (30R-1, 90–100 cm). Lithologies are also representative of 392-U1580B-2R through 5R.

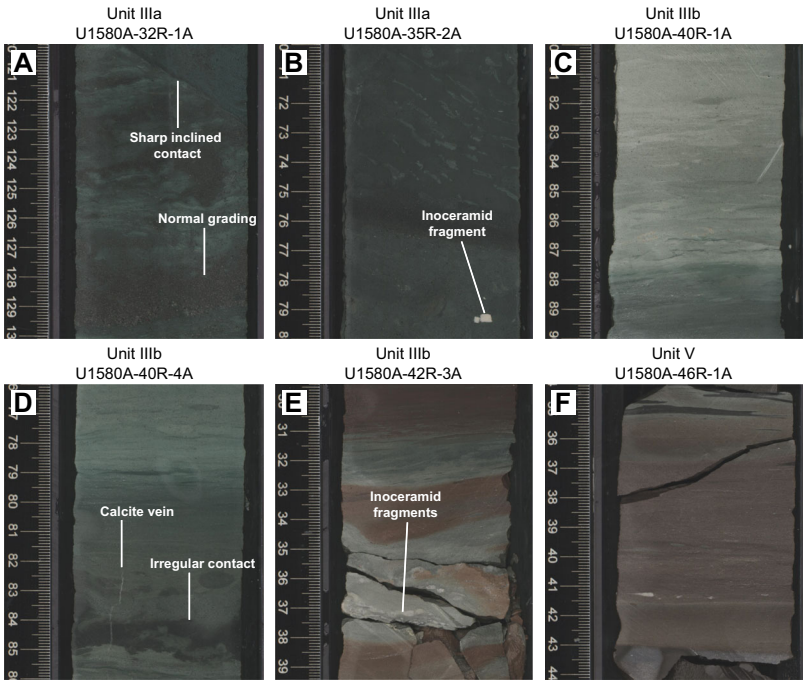

Figure F4. Major lithologies of Lithostratigraphic Units III–V, Hole U1580A. A. Dark green zeolitic siltstone with glauconite showing sharp contact between layers and bioturbation (32R-1, 120–130 cm). B. Dark green zeolitic siltstone and sandstone with glauconite and an inoceramid fragment (35R-2, 70–80 cm). C. Light green clayey calcareous chalk (40R-1, 80–90 cm). D. Calcareous siltstone with glauconite (40R-4, 76–86 cm). E. Calcareous siltstone and chalk (42R-3, 29.5–39.5 cm). F. Calcareous siltstone (46R-1, 34–44 cm).

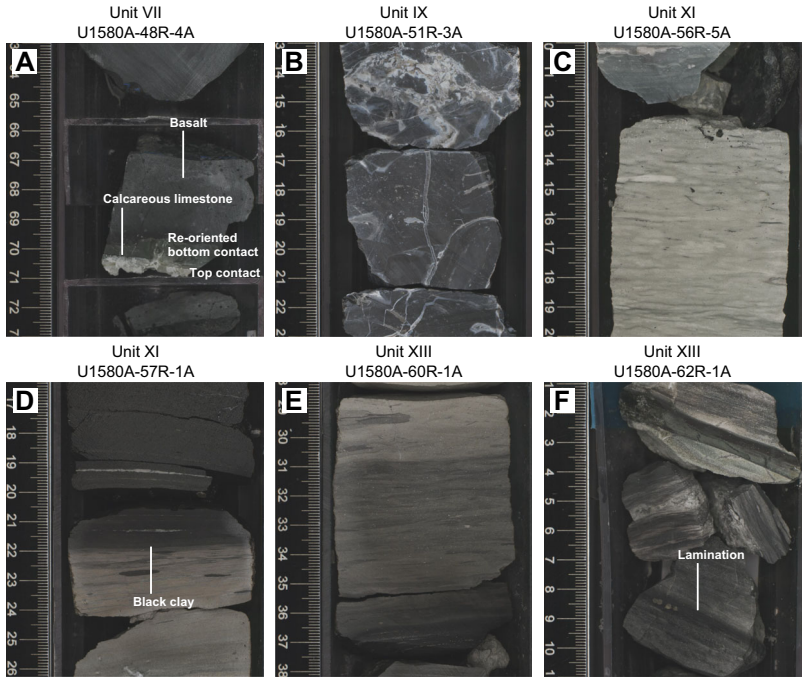

Figure F5. Major lithologies of Lithostratigraphic Units VII–XIII, Hole U1580A. A. Calcareous limestone (48R-4, 63–73 cm). B. Black chert (51R-3, 13–23 cm). C. Silicified limestone (56R-5, 10–20 cm). D. Black nannofossil-rich claystone overlying calcareous chalk (57R-1, 16.4–26.4 cm). E. Calcareous chalk with black clay (60R-1, 28–38 cm). F. Laminated siltstone (62R-1, 1–11 cm).

chalk with clay (Figure **F11**). Distinct color banding patterns and comparison with Hole U1579D suggests that Section 22R-4, ~120 cm (~209.10 m CSF-A), represents the K/Pg boundary (see **Chronostratigraphy**). Below the boundary level to Section 22R-5, 144 cm (210.84 m CSF-A), there is an interval of alternating layers of clayey calcareous chalk and calcareous chalk with clay. The degree of microfossil recrystallization increases downcore in the K/Pg interval, and the lithol-

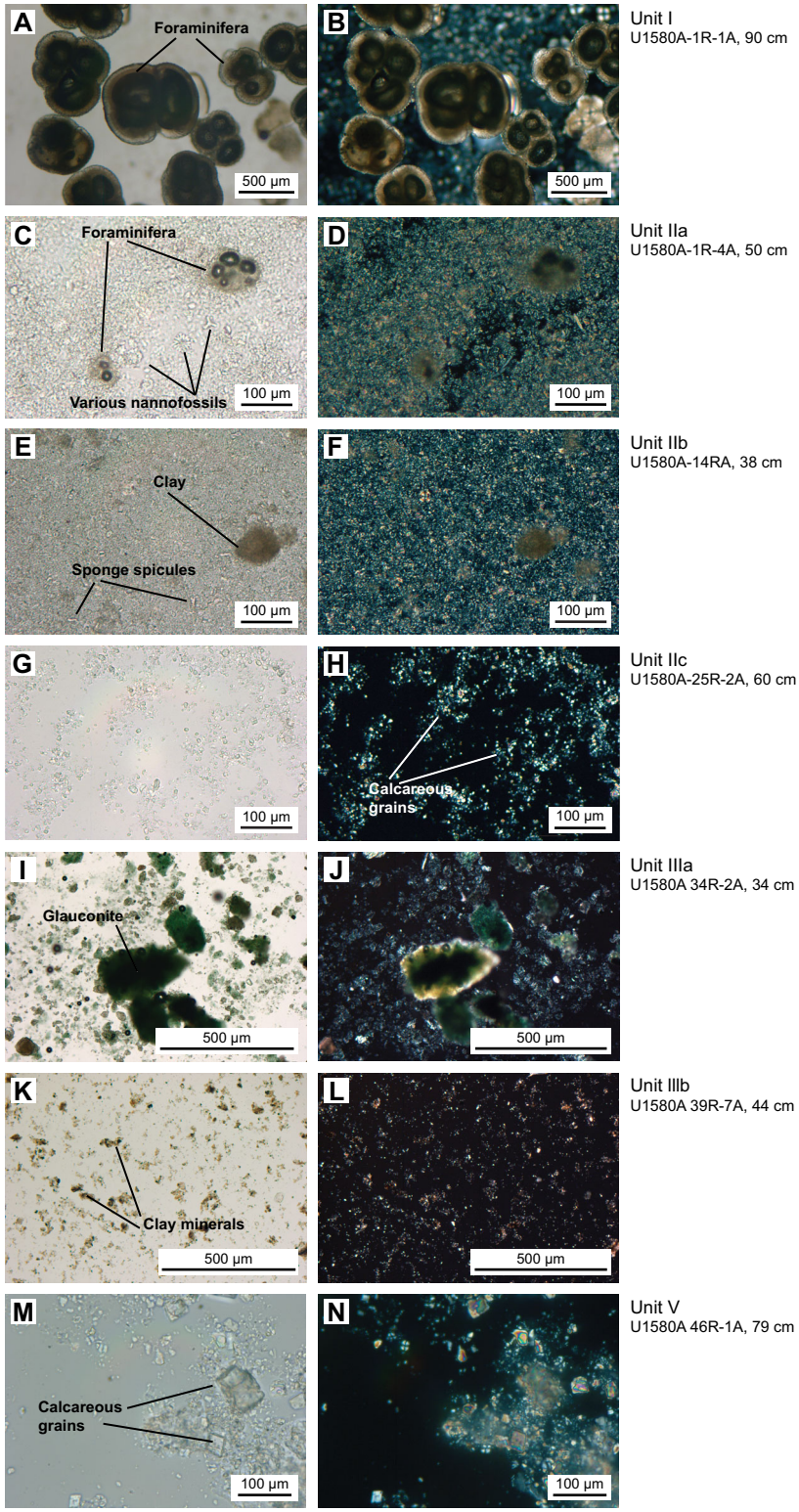

Figure F6. Major sedimentary lithologies, Site U1580. Left: plane-polarized light (PPL), right: cross-polarized light (XPL).

ogy gradually changes from nannofossil chalk to calcareous chalk (i.e., nannofossils become too rare or too poorly preserved to be distinguished from other calcareous material) from the top of Section 23R-1 to Section 31R-2, 102 cm. Recrystallized inoceramid (bivalve) fragments and prisms are present in Cores 27R, 28R, and 31R. Lithostratigraphic Subunit IIc has a gradational boundary with the green Lithostratigraphic Unit III.

3.3. Lithostratigraphic Unit III

Interval: 392-U1580A-31R-2, 102 cm, to 43R-CC, 6 cm
Depth: 293.51–407.46 m CSF-A (293.51–407.46 m CCSF)
Age: Santonian–Coniacian
Major lithologies: green zeolitic sandstone, siltstone, and claystone with glauconite

Lithostratigraphic Unit III is a 113.95 m thick interval characterized by dark green/dark bluish green zeolitic sandstone, siltstone, claystone with glauconite, glauconitic siltstone and sandstone, and light green calcareous chalk. Carbonate content is generally low (<10 wt%) in the uppermost ~50 m of Lithostratigraphic Unit III but increases over narrow intervals throughout the rest of the unit into more nannofossil-rich intervals (Figures **F2**, **F7**). The upper boundary of Lithostratigraphic Unit III also correlates with a sharp increase in MS, a drop in thermal conductivity, and an increase in porosity (see **Physical properties**).

3.3.1. Lithostratigraphic Subunit IIIa

Interval: 392-U1580A-31R-2, 102 cm, to 37R-1, 77.5 cm
Depth: 293.51–349.98 m CSF-A (293.51–349.98 m CCSF)
Age: Santonian/Coniacian
Major lithologies: green zeolitic sandstone, siltstone, and claystone

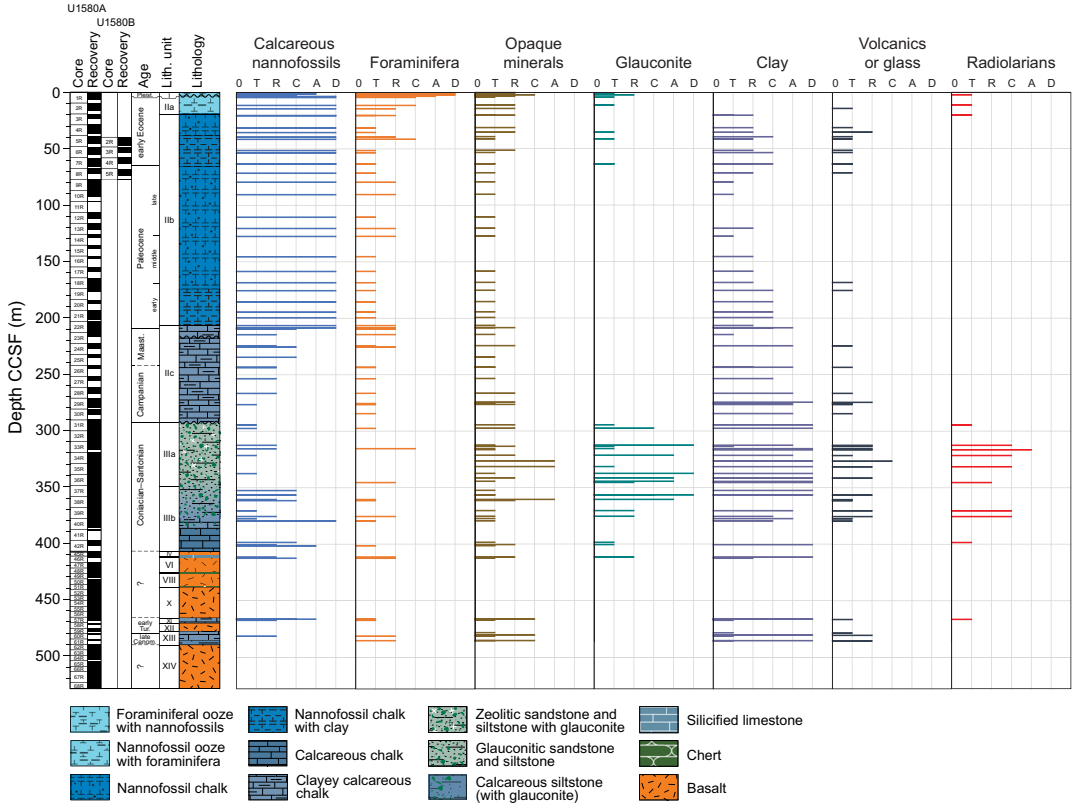

Figure F7. Abundance compilation, Site U1580. 0 = not present, T = trace (0%–1%), R = rare (1%–10%), C = common (10%–25%), A = abundant (25%–50%), D = dominant (>50%).

Lithostratigraphic Subunit IIIa is a 56.47 m interval characterized by green zeolitic sandstones, siltstones, and claystones (Figure **F4**). Smear slides from Lithostratigraphic Subunit IIIa show lower abundance and more sporadic occurrences of calcareous microfossils relative to overlying units (Figure **F7**), which is consistent with a decrease in carbonate content (<10 wt% $CaCO_3$) (Figure **F2**). Clay is common to abundant throughout the subunit, glauconite is trace to abundant, and volcanic grains, such as glass, are present throughout. Opaque minerals, such as pyrite, are present throughout (trace to abundant), and radiolarians are abundant in some intervals; however, they are often pyritized or heavily altered by diagenesis.

Three bulk sediment XRD samples were taken from Lithostratigraphic Subunit IIIa. In Sample 392-U1580A-31R-3, 79–80 cm, which is dark greenish gray zeolitic sandstone with glauconite, the main components are montmorillonite and clinoptilolite (Ca and Na). In Sample 31R-6, 42–43 cm, which is a grayish green zeolitic sandstone with glauconite, the major minerals are montmorillonite, clinoptilolite-Ca, and heulandite. In Sample 33R-5, 89–90 cm, which is a greenish black zeolitic siltstone, the main clay components are montmorillonite, glauconite, Fe^{2+}-celadonite (a mica), and several zeolite minerals including clinoptilolite (Ca and Na) and heulandite-Ca. The overall mineralogy of Lithostratigraphic Subunit IIIa is dominated by montmorillonite, clinoptilolite, and heulandite (Figure **F9**). In Sample 33R-5, 89–90 cm, the presence of ferrous celadonite, a potassium-rich phyllosilicate, corresponds to an increase in NGR (see **Physical properties**).

Bedding in Lithostratigraphic Subunit IIIa is massive, graded (in repeated intervals of normal grading), or laminated with thin to medium laminae. This unit has soft-sediment deformation features throughout, including load casts (most common), flame structures, flute casts, and rip-up clasts (Figure **F12**). Soft-sediment deformation is best defined in the green sections of the unit. Most of the unit is moderately to slightly bioturbated. Microfaulting is pervasive throughout this subunit (Figure **F13**). Faults have both planar and curved fault planes, with millimeter- to centimeter-scale offsets. Several larger scale, lower angle faults with slickensides are visible on the fault planes cut across the cores. In interval 392-U1580A-38R-7, 88–124 cm, there is a conglomerate horizon with pebble-sized bluish gray or gray clasts that are subrounded and elongated. Some of these clasts have been crosscut and elongated by microfaulting.

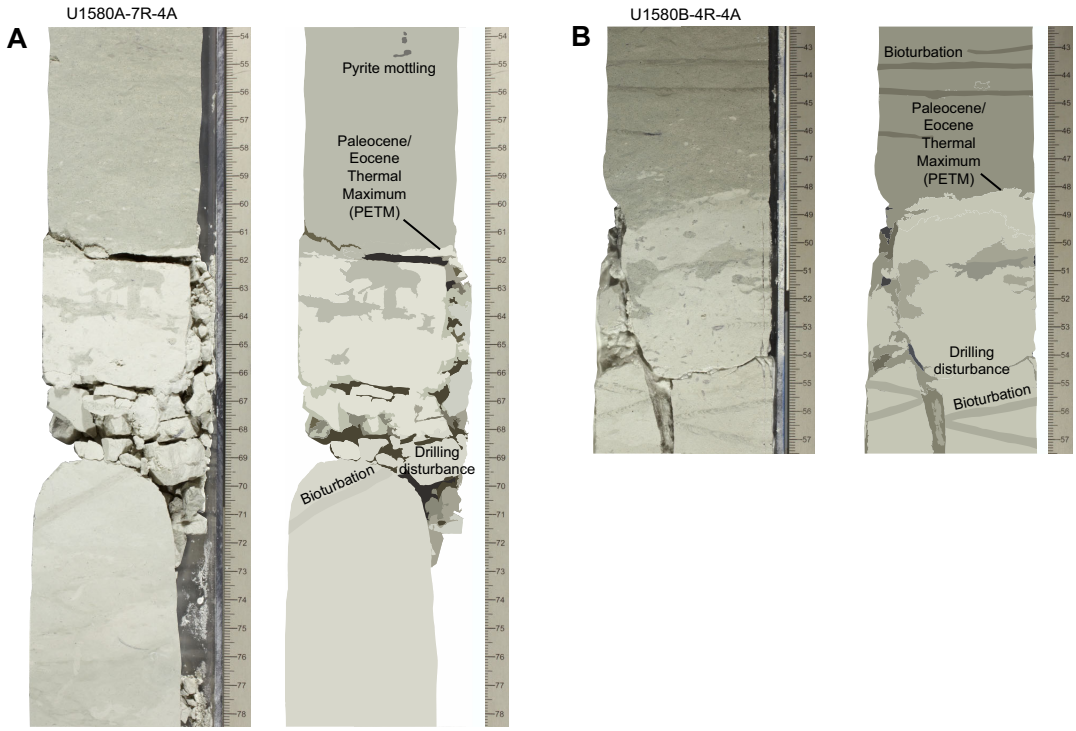

Figure F8. Paleocene/Eocene boundary, Site U1580.

pXRF analysis was done on three samples from Lithostratigraphic Subunit IIc and eight samples from Lithostratigraphic Subunit IIIa. Relative to Lithostratigraphic Subunit IIc, Lithostratigraphic Subunit IIIa generally has lower Ca content and higher Al, Fe, Mg, Mn, and Si content (Table **T3**). Three measurements from the upper portion of the green Lithostratigraphic Subunit IIIa (294.10–295.37 m CSF-A) also have higher Fe and slightly higher Hg than Lithostratigraphic Subunit IIc or the rest of Lithostratigraphic Subunit IIIa.

Although Lithostratigraphic Subunit IIIa is similar to Lithostratigraphic Unit III at Site U1579 in terms of soft-sediment deformation and grain size distribution (see **Lithostratigraphy** in the Site U1579 chapter [Bohaty et al., 2023]), Lithostratigraphic Subunit IIIa at Site U1580 is generally darker in color (dark gray, bluish gray, bluish green, dark greenish gray, and black layers are common) and lower in weight percent $CaCO_3$, has higher MS, exhibits more signs of faulting, and has a distinct mineralogical assemblage compared to Lithostratigraphic Unit III at Site U1579. Bulk sediment XRD analyses at Site U1579 suggest that Na-rich zeolite minerals (e.g., analcime and chabazite) and secondary carbonates (e.g., siderite and dolomite) are the major mineral components, whereas at Site U1580 the bulk mineralogy is dominated by a slightly variable zeolite assemblage (clinoptilolite-Ca, heulandite-Ca, and clinoptilolite-Na) and montmorillonite (Figure **F9**).

The Lithostratigraphic Subunit IIIa/IIIb contact is gradational and marked by a gradual lightening downcore due to the increased carbonate content of Lithostratigraphic Subunit IIIb.

3.3.2. Lithostratigraphic Subunit IIIb

Interval: 392-U1580A-37R-1, 77.5 cm, to 43R-CC, 6 cm
Depth: 349.975–407.46 m CSF-A (349.98–407.46 m CCSF)
Age: Santonian/Coniacian
Major lithologies: glauconitic siltstone and sandstone as well as calcareous chalk

Lithostratigraphic Subunit IIIb is a 57.48 m thick interval that is largely composed of green glauconitic siltstone and sandstone as well as light green calcareous chalk and dark green and light red calcareous sandstones, siltstones, and claystones (Figure **F4**). Relative to Lithostratigraphic Sub-

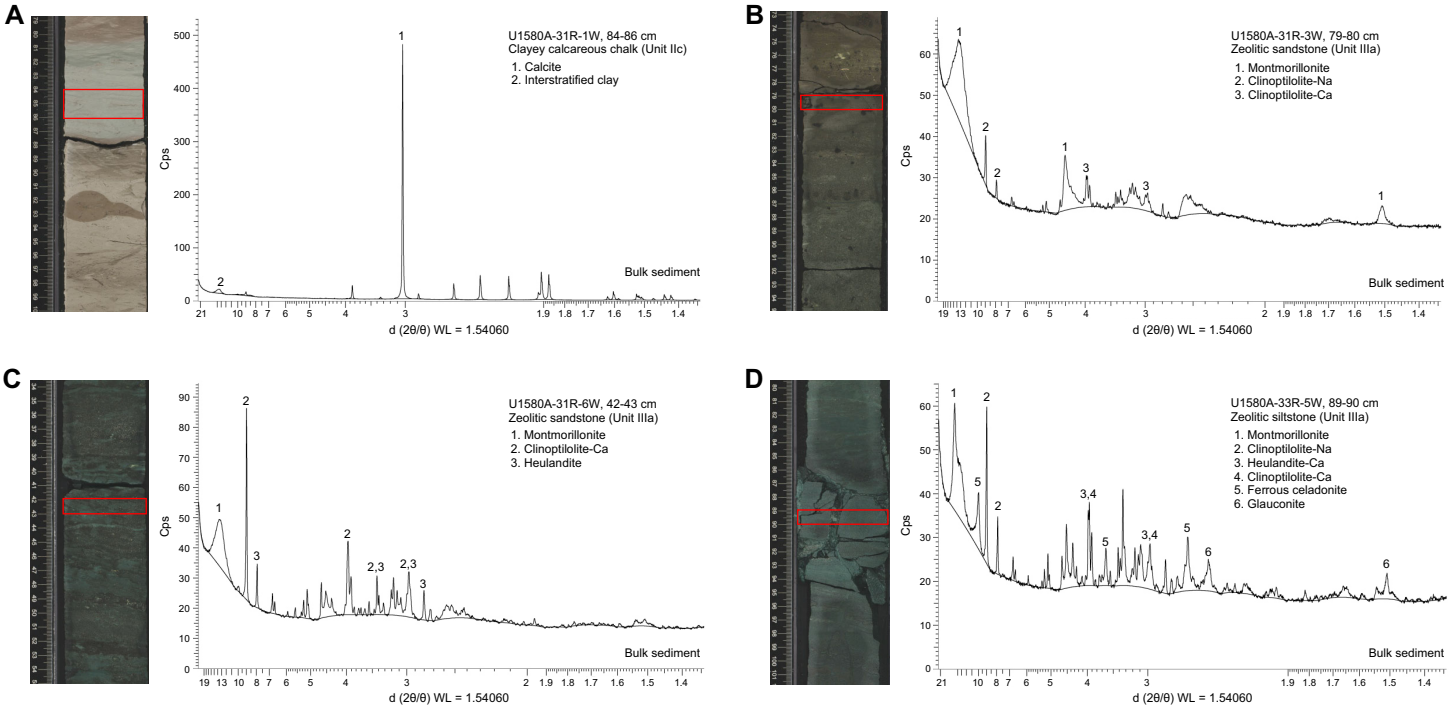

Figure F9. Bulk sediment XRD. A. Clayey calcareous chalk. Dominant mineral is calcite. B. Dark greenish gray zeolitic sandstone. Dominant minerals are montmorillonite and clinoptilolite (Na, Ca). C. Grayish green zeolitic sandstone. Dominant minerals are montmorillonite, clinoptilolite-Ca, and heulandite. D. Greenish black zeolitic siltstone. Dominant minerals are montmorillonite, clinoptilolite-Na, clinoptilolite-Ca, heulandite-Ca, ferrous celadonite, and glauconite.

unit IIIa, Lithostratigraphic Subunit IIIb contains less abundant radiolarians (Figures **F6**, **F7**). Glauconite grains become less abundant toward the lower part of the subunit where the light green intervals become more frequent (Figure **F7**). The light green intervals are calcareous chalk and contain common to abundant calcareous microfossils as well as carbonate mineral grains. Carbonate content varies throughout Lithostratigraphic Subunit IIIb, but the intervals of highest carbonate content correlate with the light green intervals (e.g., Samples 392-U1580A-23R-1, 36–37 cm; 24R-1, 102–103 cm; and 26R-3, 62–63 cm), which all have >40 wt% $CaCO_3$ (Figure **F2**). Light green calcareous intervals alternate with dark green clay-rich intervals at the decimeter scale, with gradational contacts between the alternating lithologies. The lowermost part of Lithostratigraphic Subunit IIIb (interval 43R-CC, 0–6 cm) is chert. The contact between Lithostratigraphic Subunit IIIb and basaltic Lithostratigraphic Unit IV was not recovered.

3.4. Lithostratigraphic Unit IV

Interval: 392-U1580A-43R-CC, 6 cm, to 45R-3, 64 cm
Depth: 407.46–411.76 m CSF-A (407.46–411.76 m CCSF)

Lithostratigraphic Unit IV (Igneous Unit 1) consists of 4.30 m of basalt that has a chilled lower margin where it was in contact with sediments from Lithostratigraphic Unit V (see **Igneous petrology**).

3.5. Lithostratigraphic Unit V

Interval: 392-U1580A-45R-3, 64 cm, to 46R-1, 102 cm
Depth: 411.76–412.82 m CSF-A (411.76–413.16 m CCSF)
Age: uncertain, between the lower Turonian and Coniacian
Major lithologies: silicified limestone, calcareous siltstone, and chert

Table T3. pXRF measurements of elemental concentrations, Site U1580. All measurements were completed using the pXRF device in Geochemistry mode. LE = light elements (estimated concentration of elements with X-ray energies that were not targeted by pXRF). BDL = below detection limit. **Download table in CSV format.**

Core, section, interval (cm)	Mg (ppm)	Al (ppm)	Si (ppm)	P (ppm)	S (ppm)	Cl (ppm)	K (ppm)	Ca (ppm)	Ti (ppm)	V (ppm)	Cr (ppm)	Mn (ppm)	Fe (ppm)	Co (ppm)	Ni (ppm)	Cu (ppm)	Zn (ppm)	As (ppm)
392-U1580A-																		
26R-1, 12	BDL	BDL	1,746	BDL	BDL	BDL	BDL	286,202	617	BDL	BDL	287	1,469	BDL	BDL	BDL	14	BDL
26R-1, 34	BDL	5,982	36,889	BDL	568	BDL	5,311	196,716	2,504	736	BDL	292	15,857	BDL	57	32	58	4
31R-2, 19	BDL	3,795	43,656	849	BDL	BDL	2,315	265,495	2,690	1,202	BDL	2,480	29,392	BDL	47	74	62	8
31R-3, 20	14,397	16,292	111,805	BDL	BDL	BDL	2,371	9,921	3,596	340	BDL	2,449	71,119	BDL	59	28	153	BDL
31R-3, 81	BDL	8,291	65,909	BDL	198	BDL	2,904	9,673	2,527	BDL	BDL	5,620	65,358	BDL	51	BDL	99	6
31R-4, 2	BDL	9,878	115,277	BDL	BDL	BDL	2,870	10,494	3,117	BDL	BDL	8,085	78,655	BDL	43	BDL	71	BDL
31R-6, 48	BDL	21,354	122,508	246	BDL	BDL	7,638	14,428	5,507	270	BDL	1,924	56,117	BDL	24	88	50	BDL
31R-6, 118	BDL	18,297	129,557	BDL	BDL	BDL	13,559	21,035	4,609	409	BDL	1,052	49,105	BDL	15	71	45	BDL
35R-1, 104	12,016	16,913	99,715	BDL	BDL	BDL	2,978	13,684	3,701	99	BDL	1,054	56,929	BDL	23	24	49	BDL
35R-1, 143	BDL	16,823	117,195	509	3,860	BDL	5,228	60,553	5,637	704	BDL	1,090	37,452	BDL	39	54	107	16
35R-7, 41	10,126	15,835	99,339	BDL	BDL	BDL	7,103	81,853	4,351	165	BDL	1,289	47,305	BDL	30	44	20	BDL

Core, section, interval (cm)	Se (ppm)	Rb (ppm)	Sr (ppm)	Y (ppm)	Zr (ppm)	Nb (ppm)	Mo (ppm)	Ag (ppm)	Cd (ppm)	Sn (ppm)	Sb (ppm)	W (ppm)	Hg (ppm)	Pb (ppm)	Bi (ppm)	Th (ppm)	U (ppm)	LE (ppm)
392-U1580A-																		
26R-1, 12	BDL	3	411	22	19	20	24	BDL	BDL	BDL	BDL	BDL	BDL	BDL	BDL	45	BDL	709,123
26R-1, 34	BDL	37	629	48	67	14	10	BDL	BDL	BDL	BDL	BDL	BDL	11	BDL	28	BDL	734,149
31R-2, 19	BDL	13	518	38	42	13	15	BDL	BDL	BDL	BDL	BDL	BDL	14	BDL	28	BDL	647,253
31R-3, 20	BDL	8	276	16	52	BDL	10	BDL	BDL	BDL	BDL	BDL	6	5	BDL	BDL	BDL	767,096
31R-3, 81	BDL	10	239	20	43	BDL	BDL	BDL	BDL	BDL	BDL	BDL	8	5	4	BDL	BDL	839,034
31R-4, 2	BDL	4	407	12	51	BDL	19	BDL	BDL	BDL	BDL	BDL	5	BDL	BDL	BDL	BDL	771,010
31R-6, 48	BDL	17	1,347	22	85	6	6	BDL	BDL	BDL	BDL	BDL	BDL	BDL	BDL	14	BDL	768,350
31R-6, 118	BDL	29	918	12	68	8	4	BDL	BDL	BDL	BDL	BDL	BDL	BDL	BDL	BDL	BDL	761,205
35R-1, 104	BDL	9	433	22	111	12	9	BDL	BDL	BDL	BDL	BDL	BDL	BDL	BDL	BDL	BDL	792,221
35R-1, 143	BDL	15	623	37	90	12	7	BDL	BDL	BDL	BDL	BDL	BDL	7	BDL	12	BDL	749,928
35R-7, 41	BDL	19	420	21	59	8	7	BDL	BDL	BDL	BDL	BDL	BDL	BDL	BDL	BDL	BDL	732,007

Lithostratigraphic Unit V is a 1.06 m sequence of bluish gray to light reddish gray, thinly laminated silicified limestone and chert with some calcareous siltstone (Figure **F4**). There are common veins throughout the unit that are likely infilled with calcite. This unit includes a baked horizon in interval 392-U1580A-46R-1, 96–102 cm (412.76–412.82 m CSF-A), just above the top of basalt Lithostratigraphic Unit VI. The immediate contacts between the silicified limestone and basalt

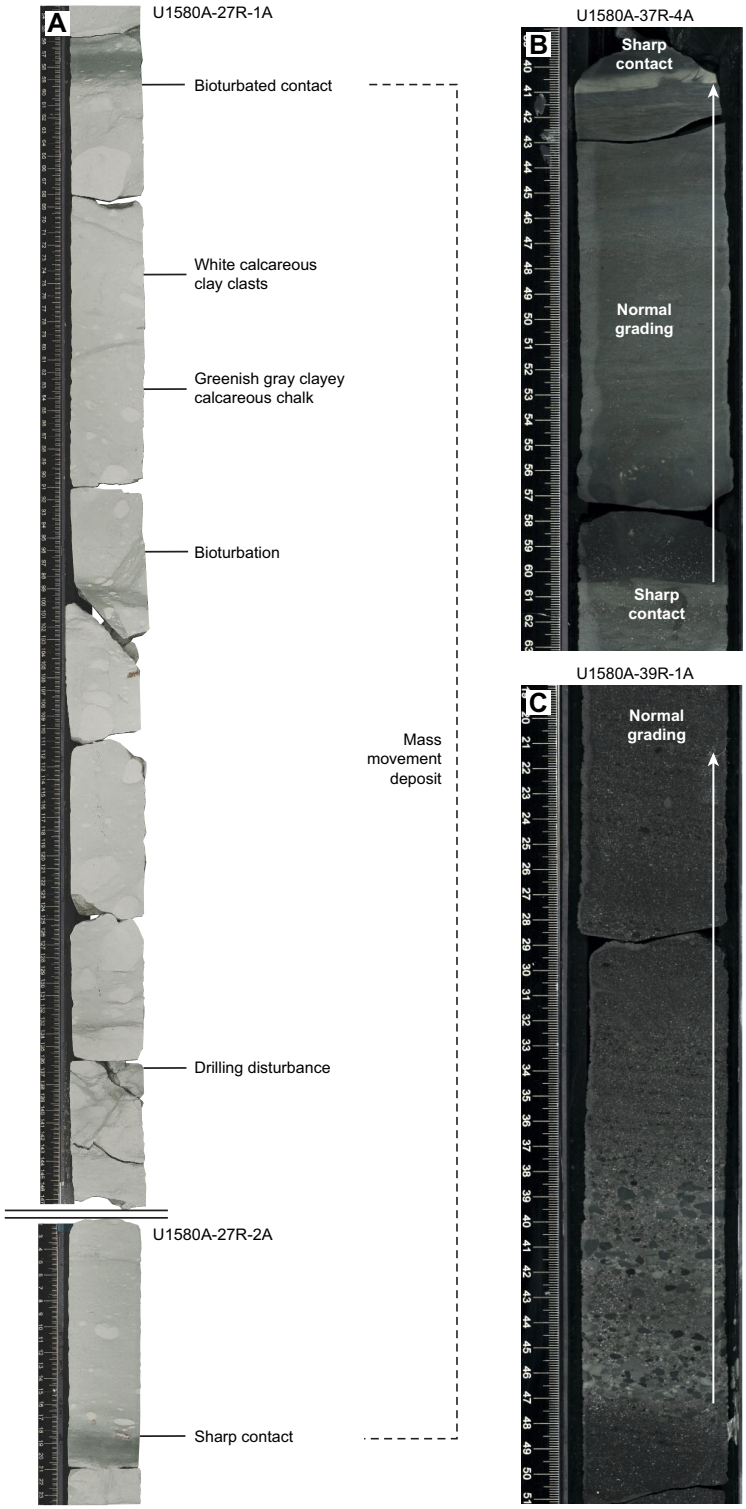

Figure F10. Examples of mass movement, Hole U1580A. A. Clasts of white calcareous clay in a matrix of greenish gray calcareous chalk. B. Fining-upward deposit, showing normal grading, ranging from coarse sand to silt. C. Fining-upward deposit showing normal grading and ranging from gravel to fine sand. Images (A, B) have been enhanced for brightness.

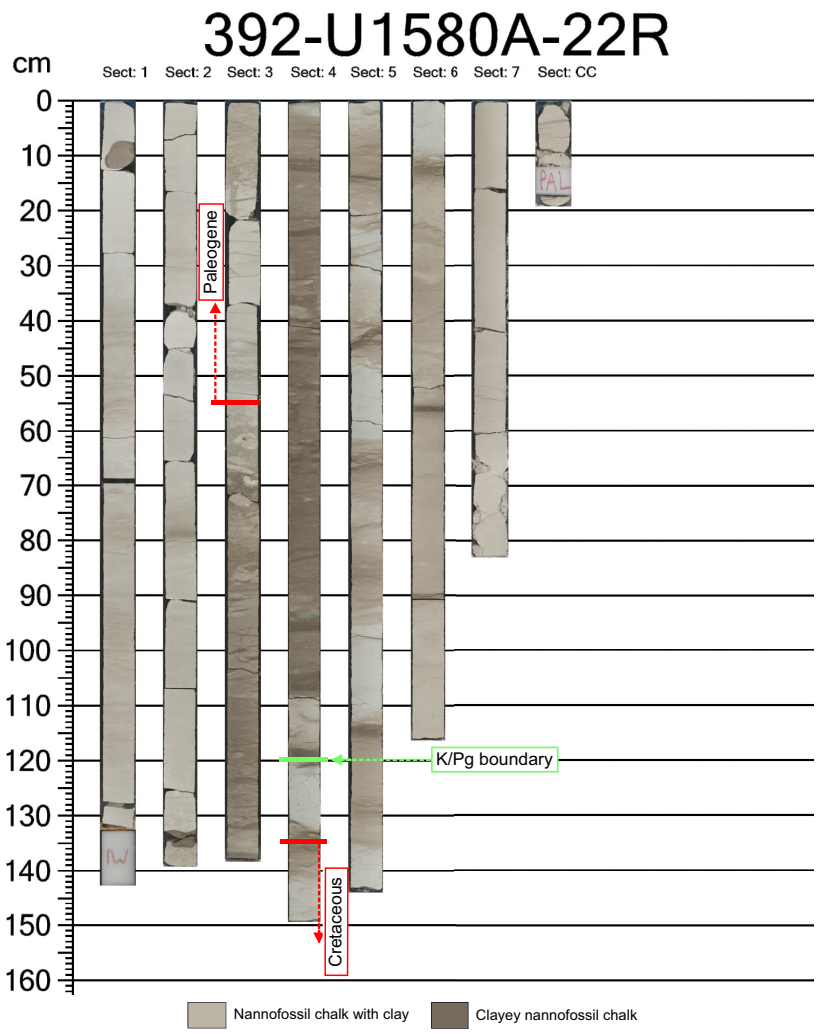

Figure F11. Core images of the K/Pg boundary, Hole U1580A. The annotations in red are based on micropaleontological observations and the green annotation is the location of the K/Pg boundary based on distinct color banding patterns and correlation with Hole U1579D.

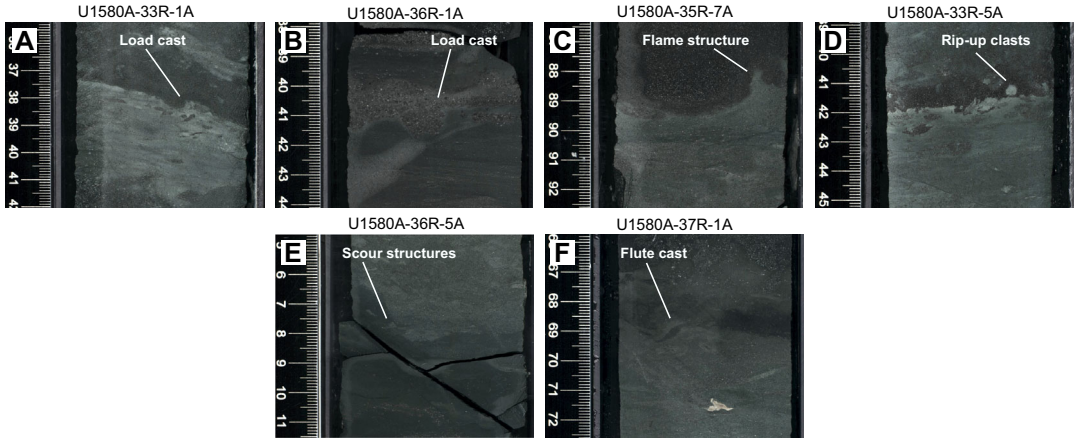

Figure F12. Examples of soft-sediment deformation encountered, Hole U1580A. A. 33R-1, 35–42 cm. B. 36R-1, 38–44 cm. C. 35R-7, 86.5–92.5 cm. D. 33R-5, 39–45 cm. E. 36R-5, 4.5–11.5 cm. F. 37R-1, 65.5–72.5 cm. The images in these panels have been enhanced for brightness.

Lithostratigraphic Units IV and VI, respectively, were not recovered, and the entirety of Lithostratigraphic Unit V is severely disturbed by drilling.

3.6. Lithostratigraphic Unit VI

Interval: 392-U1580A-46R-1, 102 cm, to 48R-4, 66 cm
Depth: 412.82–426.25 m CSF-A (413.16–423.78 m CCSF)

Lithostratigraphic Unit VI (Igneous Unit 2) consists of 13.43 m of basalt (see **Igneous petrology**).

3.7. Lithostratigraphic Unit VII

Interval: 392-U1580A-48R-4, 66 cm, to 48R-4, 68 cm
Depth: 426.25–426.27 m CSF-A (423.78–423.80 m CCSF)
Age: uncertain, between the lower Turonian and Coniacian
Major lithology: calcareous limestone

Lithostratigraphic Unit VII is a ~2 cm interval of calcareous chalk that is bounded by basalt above and below (Figure **F5**). The vertical orientation of this 2 cm thick unit is not known because it may have been rotated during drilling; however, a contact between the limestone and basalt is preserved, and there appears to be continuity between the attached basalt and intact basaltic Lithostratigraphic Unit VIII. Therefore, we have described Lithostratigraphic Unit VII with the preserved contact to be the bottom of Lithostratigraphic Unit VII (Section 392-U1580A-48R-4, 68 cm) and the top to be the thin white lamination in Section 48R-4, 66 cm (see annotations on Figure **F5A**). The remainder of Lithostratigraphic Unit VII is grayish green calcareous limestone. The recovered portion of this unit is too small to identify other bedding structures or lithologic constituents. Preliminary well log data show changes in several parameters, including a decrease in density, MS, and *P*-wave velocity (see **Downhole measurements**), and suggest that this unit is thicker (total = ~1–2 m).

3.8. Lithostratigraphic Unit VIII

Interval: 392-U1580A-48R-4, 68 cm, to 51R-2, 67 cm
Depth: 426.27–438.97 m CSF-A (423.80–439.90 m CCSF)

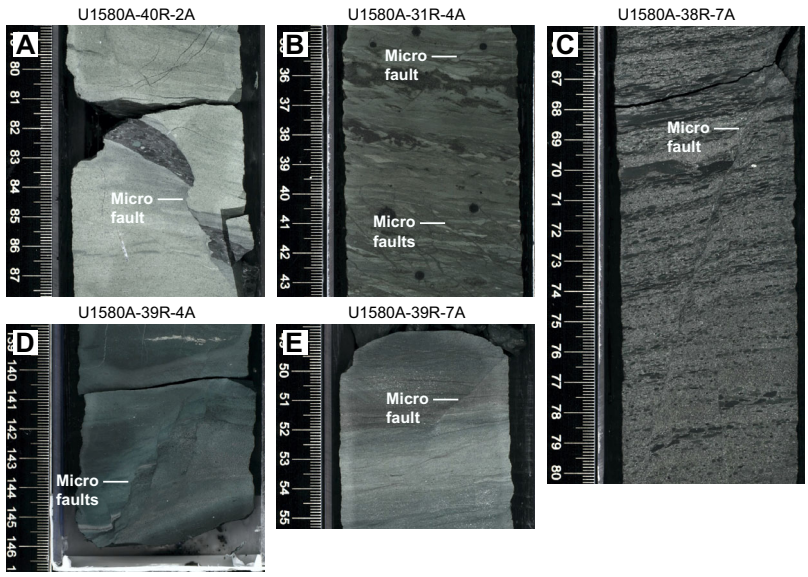

Figure F13. Microfaults, Hole U1580A. A. 40R-2, 78.5–87.5 cm. B. 31R-4, 34.5–43.5 cm. C. 38R-7, 65.5–80.5 cm. D. 39R-4, 138.5–147 cm. E. 39R-7, 48.5–55.5 cm. The images in these panels have been enhanced for brightness.

Lithostratigraphic Unit VIII (Igneous Units 3–5) consists of 12.70 m of basalt with a chilled upper margin (see **Igneous petrology**). In the uppermost 6 cm of Core 392-U1580A-49R, there are a few pebble-sized fragments of brown sandstone that are likely fall-in.

3.9. Lithostratigraphic Unit IX

Interval: 392-U1580A-51R-3, 0 cm, to 51R-3, 52 cm
Depth: 438.97–439.49 m CSF-A (439.90–440.42 m CCSF)
Age: uncertain, between the lower Turonian and Coniacian
Major lithology: chert

Lithostratigraphic Unit IX is a 52 cm interval of black chert that contains several white intersecting calcite veins (Figure **F5**). No upper or lower contacts were recovered because of drilling disturbance, which also resulted in severe brecciation of the recovered chert.

3.10. Lithostratigraphic Unit X

Interval: 392-U1580A-51R-3, 52 cm, to 56R-4, 142 cm
Depth: 439.49–466.63 m CSF-A (440.42–467.09 m CCSF)

Lithostratigraphic Unit X (Igneous Units 6 and 7) consists of 27.14 m of basalt (see **Igneous petrology**).

3.11. Lithostratigraphic Unit XI

Interval: 392-U1580A-56R-5, 0 cm, to 58R-1, 70 cm
Depth: 466.63–471.60 m CSF-A (467.09–471.60 m CCSF)
Age: lower Turonian to upper Cenomanian
Major lithologies: variable

Lithostratigraphic Unit XI is 4.97 m thick and consists of gray to black calcareous chalk, nannofossil-rich claystone, silicified limestone, and chert (Figure **F5**). Thin laminations are common in chalk intervals. Bioturbation is variable and ranges from absent to intense. There are abundant inoceramid (bivalve) fragments and prisms in interval 392-U1580A-57R-1, 20–78 cm, and there are black clay-rich intervals in intervals 57R-1, 12–22 cm; 57R-1, 45–53 cm (see annotation in Figure **F5D**); 58R-1, 13–18 cm; and 58R-1, 30–35 cm. Recovery was poor, and the recovered material was severely fragmented by drilling.

3.12. Lithostratigraphic Unit XII

Interval: 392-U1580A-58R-1, 70 cm, to 59R-2, 123 cm
Depth: 471.60–478.53 m CSF-A (471.60–478.53 m CCSF)

Lithostratigraphic Unit XII (Igneous Unit 8) consists of 6.93 m of basalt (see **Igneous petrology**).

3.13. Lithostratigraphic Unit XIII

Interval: 392-U1580A-59R-CC, 0 cm, to 62R-1, 24 cm
Depth: 478.53–490.54 m CSF-A (478.53–490.54 m CCSF)
Age: upper Cenomanian
Major lithologies: variable

Lithostratigraphic Unit XIII (Igneous Unit 9) is 12.01 m thick and consists of various lithologies including greenish gray, light brownish gray, and gray calcareous chalk; black claystone; siltstone; clayey calcareous chalk; and a few pieces of basalt (Igneous Unit 9; see **Igneous petrology**). Distinct black claystone horizons occur in intervals 392-U1580A-60R-1, 8–15 cm, and 61R-1, 51–58 cm. Bioturbation is common throughout the sedimentary intervals of Lithostratigraphic Unit XIII, and the entire unit is fractured or fragmented by drilling disturbance.

In Lithostratigraphic Unit XIII, there is a 4.86 m interval between Sections 392-U1580A-61R-1, 28 cm, and 62R-1, 24 cm, that has been severely brecciated by drilling and includes pebble- and cobble-sized pieces of both sedimentary and basaltic rocks. As such, the vertical orientation of the individual pieces in this 4.86 m interval are largely unknown. The sedimentary pieces are typically ~2–4 cm in diameter and largely consist of thinly laminated dark gray, black, green, and reddish brown calcareous chalk, siltstones, and claystones. In interval 61R-1, 28–74 cm, there are claystones with prominent pyritic features. In Section 61R-CC, there are scattered sediment pebble- and cobble-sized pieces with an oxidized appearance, which suggest a baked contact with a basaltic unit. The vertical distribution of basaltic fragments has been greatly disturbed by drilling, but basalts are documented in intervals 61R-1, 70–74 cm; 61R-CC, 6–15 cm; 61R-CC, 25–30 cm; and 62R-1, 17–19 cm.

3.14. Lithostratigraphic Unit XIV

Interval: 392-U1580A-62R-1, 24 cm, to 68R-4, 31 cm
Depth: 490.54–528.58 m CSF-A (490.54–529.59 m CCSF)

Lithostratigraphic Unit XIV (Igneous Unit 10) consists of 38.04 m of basalt. Fragments of sedimentary rocks occur in several core breaks in Lithostratigraphic Unit XIV and are interpreted as fall-in from overlying sedimentary units. Specifically, they are observed in intervals 392-U1580A-64R-1, 0–7.5 cm (pebbles of various lithologies); 64R-4, 70–73 cm (pebbles of light greenish gray siltstone, chert, and basalt); and 68R-1, 0–3 cm (3 cm clast of siltstone).

4. Igneous petrology

Igneous rocks were first reached at 407.46 m CSF-A (basaltic fragments in Section 392-U1580A-43R-CC), below sedimentary Lithostratigraphic Subunit IIIb (see **Lithostratigraphy**; Figure **F14**). Subsequently, a series of igneous units of varying thickness and often intercalated with sedimentary intervals was recovered in Hole U1580A to 528.58 m CSF-A. Each transition between sedimentary and igneous lithologies (except for pebbles interpreted as fall-in at the top of cores) defines a new lithostratigraphic unit boundary (Table **T4**). Overall, coring through continuous igneous intervals yielded excellent recovery rates (average = ~84%) (Figure **F14**).

4.1. Lithostratigraphic and igneous units

4.1.1. Lithostratigraphic Unit IV

Interval: 392-U1580A-43R-CC, 6 cm, to 45R-3, 64 cm
Depth: 407.46–411.76 m CSF-A (407.46–411.76 m CCSF)
Lithology: olivine phyric basalt
Igneous unit: 1

Lithostratigraphic Unit IV (Igneous Unit 1) is composed of slightly olivine phyric basalt. All olivine crystals, however, are completely replaced by dark secondary clay minerals with pseudomorphs averaging 1–2 mm. No other phenocrysts were detected, neither in hand specimens nor by microscopic (thin section) investigation. The groundmass is fine grained and composed of plagioclase and altered clinopyroxenes and likely altered olivine, as well as oxides. Alteration is high throughout the entire unit, although the degree of alteration is difficult to determine by the naked eye because the alteration products are dark/black clay minerals, giving the basalts the appearance of being fairly fresh. The rock is sparsely to moderately vesicular, and all vesicles are entirely filled with calcite and pyrite. Several highly elongated vesicles at the base of the unit are interpreted as pipe vesicles (traces of ascending gas bubbles), as often observed near the bottom of volcanic bodies (e.g., Philpotts and Lewis, 1987). Although the main portion of the unit is fine grained, the grain sizes at the uppermost (interval 392-U1580A-43R-CC, 6–15 cm) and lowermost (interval 45R-3A, 50–64 cm) portions of the unit decrease to aphanitic, and the latter interval is clearly recognizable as a chilled margin. Therefore, although neither the upper nor lower contacts was recovered, we assume that the recovered 3.24 m of igneous core material (recovery = 75%) roughly reflects the real thickness of this unit.

4.1.2. Lithostratigraphic Unit VI

Interval: 392-U1580A-46R-1, 102 cm, to 48R-4, 66 cm
Depth: 412.82–426.25 m CSF-A (413.16–423.78 m CCSF)
Lithology: sparsely plagioclase phyric basalt
Igneous unit: 2

The igneous rocks of Lithostratigraphic Unit VI were encountered beneath a thin sedimentary interval (recovery = 115 cm) of calcareous siltstone with cherts (Lithostratigraphic Unit V; see **Lithostratigraphy**) and are composed of sparsely plagioclase phyric basalt. The plagioclase phenocrysts range as large as 2 mm but constitute only ~1% of the rock, although the numerous glomerocrysts of groundmass feldspar laths make the rock appear more phyric than it actually is. Other groundmass constituents include relatively large oxides, plagioclase, and altered clinopyroxene and olivine. The basalt is pervasively altered, although it can be difficult to tell from hand sample because the alteration products are largely dark/black clay minerals. In general, the rock is nonvesicular, but the few small vesicles that appear (<1%) are always filled with calcite or clay minerals. Small pipe vesicles can be found at the base of the unit (interval 392-U1580A-48R-4, 60–63 cm). Although the upper and lower portions of the unit are fine grained, the rock grades to a medium grain size in its center (between Section 48R-1 and the upper part of Section 48R-3). Although 6.33 m of core material was recovered from this unit, no abrupt lithologic changes (e.g., different mineralogy or multiple cooling units) could be recognized, and therefore Lithostratigraphic Unit VI was not further divided and comprises only one igneous unit (Igneous Unit 2), which is confined by a chilled margin at its base in interval 48R-4, 54–66 cm. The igneous rock recovery for this unit yielded 47%.

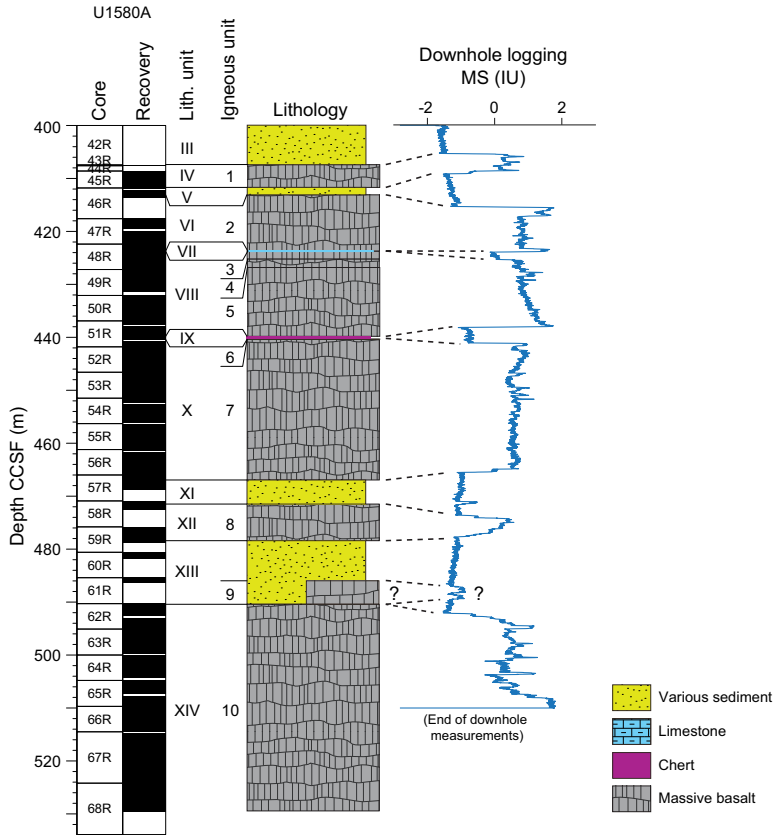

Figure F14. Stratigraphic summary of the lowermost ~130 m of Hole U1580A compared with corrected downhole logging MS results. ? = unverified unit thickness.

4.1.3. Lithostratigraphic Unit VIII

Interval: 392-U1580A-48R-4, 68 cm, to 51R-2, 67 cm
Depth: 426.27–438.97 m CSF-A (423.80–439.90 m CCSF)
Lithology: aphyric and olivine phyric basalt
Igneous units: 3–5

Lithostratigraphic Unit VIII comprises Igneous Units 3–5. The upper boundary of Igneous Unit 3 is defined by an igneous contact with a rim of contact-metamorphically altered white carbonate, of which only 2 cm was recovered (Lithostratigraphic Unit VII), although downhole logging results suggest that this carbonate layer could be as thick as ~1–2 m (see MS data in Figure **F14** and further details in **Downhole measurements**). The igneous rock is classified as aphyric basalt, although small, sparse plagioclase phenocrysts are present, and the fine-grained groundmass is composed of plagioclase, replaced olivine, oxides, and altered subophitic clinopyroxenes (bladed crystals of plagioclase surrounded by large subhedral pyroxenes). The upper portion of the unit (Section 392-U1580A-48R-4) contains highly spherical vesicles that are completely filled with clay minerals. The rock is predominantly fine grained except for its aphanitic (chilled) margins at the top and base of the unit. A well-defined chilled margin in interval 48R-5, 65–78 cm, marks the base of Igneous Unit 3 and the top of Igneous Unit 4. The upper contact of Igneous Unit 4 was not recovered, but the uppermost rocks of Igneous Unit 4 show a fine-grained groundmass grain size. Defining these rocks as a new igneous unit is further justified by the different petrological composition of Igneous Unit 4. Whereas Igneous Unit 3 basalts are aphyric, Igneous Unit 4 basalts contain up to 5% of relatively large (as large as 3 mm) olivine pseudomorphs filled with black clay minerals. In contrast, no petrological differences could be detected between Igneous Units 4 and 5, which are separated by a 4 cm piece of baked white limestone found at the base of Core 48R. If this piece represents fall-in material (perhaps from the white limestone sequence of Lithostrati-

Table T4. Lithostratigraphic and igneous unit summaries, Hole U1580A. Includes subdivisions for Igneous Unit 10. **Download table in CSV format.**

Lith. unit	Igneous unit/subunit	Core, section, interval (cm)	Depth CSF-A (m)	Thickness CSF-A (m)	Depth CCSF (m)	Thickness CCSF (m)	Lithology
		392-U1580A-					
IV	1	43R-CC, 6, to 45R-3, 64	407.46–411.76	4.30	407.46–411.76	4.30	Olivine (altered)-phyric basalts with vesicles
V		45R-3, 64, to 46R-1, 102	411.76–412.82	1.06	411.76–413.16	1.40	Calcareous siltstone with chert
VI	2	46R-1, 102, to 48R-4, 66	412.82–426.25	13.43	413.16–423.78	10.62	Plagioclase phyric basalt
VII		48R-4, 66, to 48R-4, 68	426.25–426.27	0.02	423.78–423.80	0.02	Baked carbonate (limestone/marble)
VIII	3	48R-4, 68, to 48R-5, 78	426.27–427.79	1.51	423.80–425.32	1.51	Aphyric basalt
	4	48R-5, 78, to 48R-6, 126	427.79–429.37	1.58	425.32–426.90	1.58	Olivine (altered)-phyric basalt
	5	49R-1, 6, to 51R-2, 67	427.26–438.97	11.71	427.26–439.90	12.64	Olivine (altered)-phyric basalt
IX		51R-2, 67, to 51R-3, 52	438.97–439.49	0.52	439.90–440.42	0.52	Cherts
X	6	51R-3, 52, to 51R-3, 56	439.49–439.53	0.04	440.42–440.46	0.06	Aphyric basalt with flow texture
	7	52R-1, 3, to 56R-4, 142	441.83–466.63	24.80	440.74–467.09	26.35	Plagioclase phyric basalt
XI		56R-4, 142, to 58R-1, 70	466.63–471.60	4.97	467.09–471.60	4.51	Chert, limestone, calcareous chalk, claystone
XII	8	58R-1, 70, to 59R-2, 123	471.60–478.53	6.93	471.60–478.53	6.93	Plagioclase phyric basalt
XIII		59R-CC, 0, to 62R-1, 24	478.53–490.54	12.01	478.53–490.54	12.01	Calcareous chalk, claystone, siltstone, clayey calcareous chalk
	9	61R-1, 70, to 62R-1, 19	486.10–490.49	4.39	486.10–490.49	4.39	Aphyric basalt rubble within sediment rubble of aphanitic, microvesicular, or flow texture basalt (apophysis?)
XIV	10a	62R-1, 24, to 63R-1, 66	490.54–495.76	5.22	490.54–493.72	3.18	Plagioclase phyric basalt
	10b	63R-1, 66, to 63R-2, 16	495.76–495.98	0.22	493.72–493.94	0.22	Aphyric basalt
	10a	63R-2, 16, to 63R-6, 18	495.98–501.28	5.30	493.94–499.24	5.30	Plagioclase phyric basalt
	10b	63R-6, 18, to 63R-6, 69.5	501.28–501.79	0.52	499.24–499.75	0.52	Aphyric basalt
	10c	64R-1, 8, to 64R-1, 19	500.08–500.19	0.19	500.08–500.19	0.19	Subophitic basalt
	10a	64R-1, 19, to 64R-3, 68	500.19–502.96	2.76	500.19–502.96	2.76	Plagioclase phyric basalt
	10b	64R-3, 68, to 64R-3, 113	502.96–503.41	0.45	502.96–503.41	0.45	Aphyric basalt
	10a	64R-3, 113, to 65R-1, 98	503.41–505.78	2.38	503.41–505.78	2.38	Plagioclase phyric basalt
	10b	65R-1, 98, to 65R-2, 58	505.78–506.78	1.00	505.78–506.78	1.00	Aphyric basalt
	10c	65R-2, 58, to 66R-1, 45	506.78–510.15	3.37	506.78–508.13	1.35	Subophitic basalt
	10b	66R-1, 45, to 67R-3, 33	510.15–517.48	7.33	508.13–517.70	9.57	Doleritic basalt
	10c	67R-3, 33, to 67R-4, 100	517.48–518.77	1.29	517.70–518.99	1.29	Dolerite
	10b	67R-4, 100, to 67R-5, 24	518.77–519.47	0.70	518.99–519.69	0.70	Dolerite
	10c	67R-5, 24, to 67R-5, 55	519.47–519.78	0.31	519.69–520.00	0.31	Dolerite
	10b	67R-5, 55, to 68R-1, 100	519.78–525.20	5.42	520.00–526.21	6.21	Dolerite
	10a	68R-1, 100, to 68R-3, 96	525.20–527.97	2.77	526.21–528.98	2.77	Doleritic plagioclase phyric basalt
	10c	68R-3, 96, to 68R-4, 11	527.97–528.38	0.41	528.98–529.39	0.72	Doleritic basalt
	10a	68R-4, 11, to 68R-4, 31	528.38–528.58	0.20	529.39–529.59	0.20	Doleritic basalt

graphic Unit VII above), then the 1.58 m Igneous Unit 4 and the 11.71 m Igneous Unit 5 (Sections 49R-1 through 51R-2) should be treated as a single igneous unit. Occurrence of fall-in material, however, is uncommon at the bottom of a core. Both Igneous Units 4 and 5 are nonvesicular, sparsely olivine (pseudomorphs) phyric basalts (Figure **F15A**). The clay-filled pseudomorphs are 2–3 mm, whereas groundmass plagioclase can form glomerocrysts as large as 5 mm. Other groundmass minerals include plagioclase laths, relatively well preserved clinopyroxenes, altered olivine, and oxides. Both units are predominantly medium grained, and the base of Igneous Unit 5 shows a well-defined chilled margin with systematic gradation of groundmass grain size from medium to fine grained to aphanitic in Section 51R-2, 0–67 cm. The recovered 1.52 m (Igneous Unit 3), 1.58 m (Igneous Unit 4), and 11.24 m (Igneous Unit 5) of material correspond to a recovery of 100% for Igneous Units 3 and 4 and 96% for Igneous Unit 5.

4.1.4. Lithostratigraphic Unit X

Interval: 392-U1580A-51R-3, 52 cm, to 56R-4, 142 cm
Depth: 439.49–466.63 m CSF-A (440.42–467.09 m CCSF)
Lithology: aphyric and slightly plagioclase phyric basalt
Igneous units: 6 and 7

Lithostratigraphic Unit X rests below a thin interval (recovery = 52 cm) of predominantly black chert in Section 392-U1580A-51R-3 (Lithostratigraphic Unit IX) that could be as thick as ~3 m according to downhole logging measurements (see Figure **F14** and further details in **Downhole measurements**). Below this interval, a single 4 cm long piece of aphyric basalt was recovered and defined as Igneous Unit 6. The groundmass of the rock shows a distinct trachytic (flow) fabric, a feature not observed in the igneous units above or below, and this piece was therefore defined as a distinct igneous unit. No vesicles could be recognized. The top of subsequent Core 52R contains a small piece of fall-in that is interpreted to represent a piece of the overlying Igneous Unit 5 based on petrographic evidence (nonvesicular, sparsely olivine [pseudomorphs] phyric, groundmass plagioclase glomerocrysts). The underlying basalt shows an aphanitic and aphyric chilled margin at its top and therefore marks the beginning of Igneous Unit 7. Considering its aphanitic grain size and similar lack of phenocrysts, the single piece of Igneous Unit 6 could be associated with this chilled margin of Igneous Unit 7; its fundamental different trachytic texture, however, makes this unlikely. Aside from its uppermost aphyric 17 cm, Igneous Unit 7 is sparsely plagioclase phyric with plagioclase glomerocrysts averaging about 3 mm in size but ranging as large as 8 mm. The groundmass is composed of large subophitic clinopyroxenes (Figure **F15B**) with plagioclase, replaced olivine, and oxides. Igneous Unit 7 is 24.80 m thick with a well-defined chilled margin at the bottom of Section 56R-4, which is similar to that observed at the top of the unit. The recovered 25.4 m of Igneous Unit 7 corresponds to a recovery of 102%.

4.1.5. Lithostratigraphic Unit XII

Interval: 392-U1580A-58R-1, 70 cm, to 59R-2, 123 cm
Depth: 471.60–478.53 m CSF-A (471.60–478.53 m CCSF)
Lithology: plagioclase phyric basalt
Igneous unit: 8

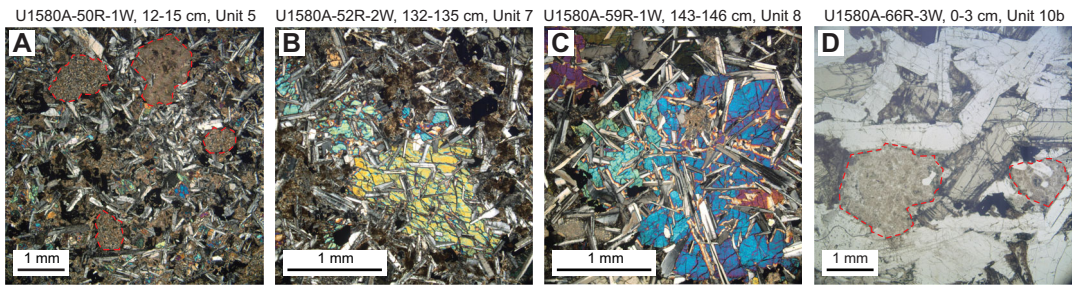

Figure F15. Igneous rocks, Hole U1580A. A. Olivine pseudomorphs (red dashed lines) (50R-1, 12–15 cm; XPL). B. Subophitic clinopyroxene (several bladed plagioclase crystals fully or partly enclosed by a large clinopyroxene crystal) (52R-2, 132–135 cm; XPL). C. Subophitic clinopyroxene (59R-1, 143–146 cm; XPL). D. Olivine pseudomorphs (66R-3, 0–3 cm; PPL).

Below a sedimentary succession of cherts, limestone, calcareous chalk, and claystone (Lithostratigraphic Unit XI), the top of Lithostratigraphic Unit XII is defined in Section 392-U1580A-58R-1, 70 cm, and continues to the base of Section 59R-2. The entire lithostratigraphic unit comprises Igneous Unit 8, and there is evidence of chilled margins at both the top and bottom of the unit. A single piece of aphanitic, aphyric, vesicular basalt is present in the bottom 2 cm of Section 58R-1. This lithology is continued in the top 12 cm of Section 58R-2, below which the grain size increases and becomes fine grained. The top of the unit begins as highly vesicular, with all vesicles filled with calcite or white zeolites and clay minerals, and then it decreases in vesicularity to Section 59R-1, 112 cm, below which no more vesicles are found. The rock contains 2% plagioclase phenocrysts 2–3 mm in size, and the groundmass is composed of large subophitic clinopyroxene (Figure **F15C**), plagioclase, oxides, and altered olivine and interstitial material. Toward the bottom of the unit, the grain size again becomes systematically finer, and another chilled margin is found in interval 59R-2, 121–122 cm. The aphanitic contact approaches a glassy texture. The material in the core catcher below this section is sedimentary (Lithostratigraphic Unit XIII). A total of 3.62 m of rock was obtained from Igneous Unit 8 (recovery = 52%).

4.1.6. Lithostratigraphic Unit XIII

Interval: 392-U1580A-59R-CC, 0 cm, to 62R-1, 24 cm
Depth: 478.53–490.54 m CSF-A (478.53–490.54 m CCSF)
Lithology: sediment mixed with aphyric basalt
Igneous unit: 9 (392-U1580A-61R-1, 70 cm, to 62R-1, 19 cm; 486.10–490.49 m CSF-A [486.10–490.49 m CCSF])

Lithostratigraphic Unit XIII comprises several pieces of basaltic rubble throughout sedimentary rubble (many without determinable upward or downward orientation). This lithostratigraphic unit therefore includes both igneous and sedimentary lithologies. In total, four small basaltic pieces are dispersed throughout this unit (intervals 392-U1580A-61R-1, 70–74 cm; 61R-CC, 11–15 cm; 61R-CC, 25–30 cm; and 62R-1, 17–19 cm), likely dislocated during the drilling process. Based on petrological similarity, the individual basaltic pieces together constitute Igneous Unit 9. The depth where these fragments were found in the core sections does not reflect the true location or thickness of this basaltic unit, which would, shifted together, span only about 14 cm. Considering that Lithostratigraphic Unit XIII spreads over a total drilling advancement of ~12 m, the basalts could either stem from a single igneous sheet located somewhere in the sedimentary package (and dissected by drilling disturbance) or represent small finger-like igneous intrusions (termed apophyses) that occasionally emanate from the margins of larger intrusive bodies (such as the exceptionally thick Igneous Unit 10 located directly below).

The individual basalt clasts are composed of vesicular, aphyric basalt that is moderately to highly altered. Two pieces, one in interval 392-U1580A-61R-1, 70–74 cm, and the other in interval 61R-CC, 11–15 cm, show a trachytic (flow) texture. Their aphanitic to fine-grained groundmass grain size would either fit with them being apophyses or representing a thin igneous sheet. Both would cool rapidly, leaving no time for the minerals to grow to larger sizes during the crystallization process. The poor recovery rate of just 22% over the entire interval of Lithostratigraphic Unit XIII, however, leaves this question open. Downhole logging data show two small peaks in MS (possibly indicating igneous material) at ~488 m CCSF (Figure **F14**), which support the view that the recovered rock reflects thin apophyses.

4.1.7. Lithostratigraphic Unit XIV

Interval: 392-U1580A-62R-1, 24 cm, to 68R-4, 31 cm
Depth: 490.54–528.58 m CSF-A (490.54–529.59 m CCSF)
Lithology: aphyric basalt/dolerite
Igneous unit: 10

Lithostratigraphic Unit XIV comprises the single massive basaltic Igneous Unit 10 that is divided into three distinct facies (Subunits 10a, 10b, and 10c). Note that these subunits have no stratigraphic relevance because they repeatedly recur within Igneous Unit 10. The subunit divisions are based on differences in macro- and microscopic texture and appearance (Table **T4**), and the

breakdown into igneous subunits (rather than introducing new units) is founded on the generally gradual transitions (over several centimeters) between subunits and the reoccurrence of the individual subunits throughout the entire igneous succession. In addition, no significant grain size change, which would indicate separate cooling units, is observed at these transitions. Overall, Igneous Unit 10 shows a clearly defined chilled margin at its top with an apparent igneous contact to the overlying sediment (2 mm thin baked sediment rind in Section 392-U1580A-62R-1, 24 cm [Piece 2a]). Below this level, the basalt is aphanitic for 8 cm (interval 62R-1, 24–32 cm) and then underlain by a fine-grained groundmass (interval 62R-1, 32–98 cm). Interval 62R-1, 24–40 cm, is moderately vesicular grading to sparsely vesicular below. These vesicles are all filled with dark clay minerals and/or zeolites and average 4 mm at the top and 1 mm lower down. Farther downhole, the remainder of Igneous Unit 10 is nonvesicular.

Igneous Subunit 10a, which recurs six times in Igneous Unit 10 (see Table **T4**), is defined by the presence of plagioclase phenocrysts as large as 10 mm, which are particularly noticeable on the back side (drilled surface) of the core. The abundance and average size range 3%–8% and 3–6 mm, respectively. Thin section examinations reveal that many of these phenocrysts are glomerocrysts of several (but still larger than groundmass) plagioclase crystals (Figure **F16**). Pseudomorphs of presumed olivine phenocrysts are found in lesser abundances (~4%) and are completely replaced by clay minerals, resulting in an overall moderate alteration of Igneous Subunit 10a basalts. The groundmass is medium grained and composed of plagioclase, clinopyroxene, oxides, chloritized olivine, and altered interstitial material.

The uppermost occurrence of Igneous Subunit 10b is in Section 392-U1580A-63R-1, 66 cm. In total, seven intervals of this subunit are identified in Igneous Unit 10. Igneous Subunit 10b is characterized by a lack of plagioclase phenocrysts and a high degree of alteration (Figure **F16**) and appears slightly coarser grained than the other subunits. The groundmass is composed of plagioclase, clinopyroxene, oxides, olivine pseudomorphs (Figure **F15D**), and altered interstitial material. Substituting clay minerals often form centimeter-sized dark patches on the rock surface

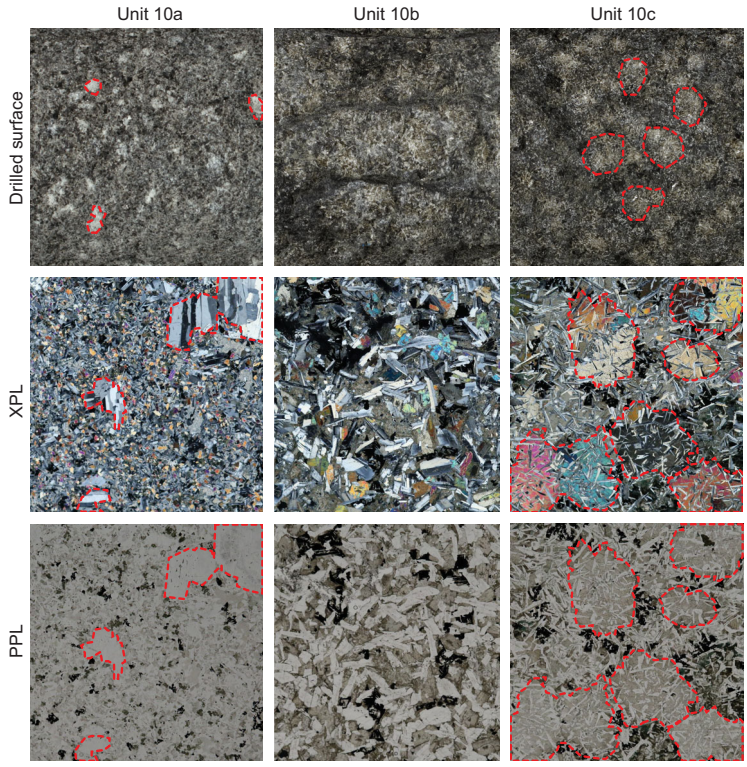

Figure F16. Defining characteristics of Igneous Subunits 10a–10c (Lithostratigraphic Unit XIV), Hole U1580A. Top row: outside (drilled) surface of the split section half of representative samples. Middle (XPL) and bottom (PPL) rows: thin section images. Red dashed lines = plagioclase glomerocrysts in Igneous Subunit 10a and subophitic clinopyroxenes in Igneous Subunit 10c.

(particularly noticeable on the split surface of the core). It is suspected that these patches reflect agglomerates of altered olivine crystals (pseudomorphs), but this could not be confirmed based on thin section examinations. Alternatively, these zones could reflect higher concentrations of altered interstitial material. Another striking feature is that this subunit is associated with dark, clay-mineral filled veins or vein networks. It remains unclear whether fluid migration extending from these veins caused the overall higher degree of alteration of this subunit or whether the high alteration state of the rock resulted in higher porosity and lower density and has therefore provided preferential pathways for fracturing and fluid migration.

The uppermost appearance of Igneous Subunit 10c is in Section 392-U1580A-64R-1, 8 cm, and this subunit recurs five times in Igneous Unit 10. This subunit can be easily identified by its macroscopically patchy appearance, which corresponds with the presence of large (>10 mm) subophitic clinopyroxenes visible in thin section (Figure **F16**). Such speckled texture is also called ophimottled. Olivine also appears to show subophitic texture in thin section, although it is smaller and less abundant than the clinopyroxenes, and appears to be completely replaced with alteration minerals including chlorite. The remainder of the groundmass is composed of plagioclase, oxides, and altered interstitial material. Igneous Subunit 10c is usually spatially associated with Igneous Subunit 10b (see Table **T4** for stratigraphic location of divisions within Igneous Unit 10).

Drilling in Hole U1580A terminated during penetration of an interval of Igneous Subunit 10a (bottom of lowermost piece in Section 68R-4, 31 cm). At that point, the total penetrated thickness of Igneous Unit 10 reached 38.04 m, of which 37.13 m rock material was recovered (98%). The overall grain size of the Igneous Unit 10 rocks becomes coarse grained (~2 mm groundmass crystals) in Sections 66R-1 through 67R-8. In addition, the texture in this interval becomes largely equigranular (and by definition, aphyric) (Figure **F15D**). Because of the larger grain size and more equigranular texture, we classified the rock as dolerite between Sections 66R-1, 130 cm, and 68R-1, 3 cm. Igneous Unit 10 continues to the bottom of Hole U1580A, and therefore a lower contact was not recovered. The groundmass grain size in the lowermost basalts of Igneous Unit 10, however, decreased to medium grained, and the rock shows moderately phyric (Igneous Subunit 10a) or subophitic (Igneous Subunit 10c) textures in Section 68R-1 and below. This transition could indicate that drilling was approaching the lower margin of this unit.

4.2. Interpretation of the igneous units

The intercalation of igneous bodies and sediment packages in Hole U1580A implies that these units either represent lateral intrusions (sills) or that they were emplaced as lava flows on which sediments were deposited after each eruption. Based on several lines of evidence, we tentatively interpret this igneous succession as sills.

As stated in the discussion of the Site U1579 coring results (see **Igneous petrology** in the Site U1579 chapter [Bohaty et al., 2023]), the distinction of lava flows and intrusive sheets can be difficult with drill core samples (Koppers et al., 2010). Lava flows generally possess highly fractured and brecciated flow tops. Chilled margins are usually thin or absent. If erupted into water, however, glassy margins are common. Submarine lava flows advancing over soft (unconsolidated) seafloor sediment often form peperite facies (Skilling et al., 2002), resulting from various lava-sediment interactions and intermingling creating fragmented and deformed margins. In contrast, sill intrusions often show broad chilled margins but distinct, sharp contact surfaces and slow gradational changes in crystallinity (grain size) toward coarsely crystalline interiors. In this respect, the recovered igneous units resemble sills rather than lava flows. For instance, we recognize distinct chilled margins for most units at both the top and bottom of the units (even if the igneous contacts themselves are seldom preserved and recovered with RCB coring): at the top of Igneous Units 3, 7, 8, and 10 and at the bottom of Igneous Units 1, 2, 3, 5, 7, and 8 (Igneous Units 6 and 9 comprise only unoriented igneous rubble pieces). Submarine lava flows commonly exhibit thick glassy rinds (resulting from a more efficient quenching process in an aqueous environment). However, no glassy material or its alteration product, palagonite, was found at these margins (even where the direct contact was recovered). The ophitic or subophitic textures (bladed plagioclase surrounded by subhedral pyroxene) observed in the rocks of Igneous Units 3, 7, and 8 and Subunits 10b and especially 10c is also consistent with these bodies representing sills. This texture is

typical for dolerites (also called diabase or microgabbro), which is considered a subvolcanic equivalent of basalt and usually found in relatively shallow intrusions such as dikes and sills (e.g., Klein et al., 1993). Igneous Unit 10 bears perhaps the most compelling evidence for being a sill, considering its thickness and strongly increasing grain size toward the center of the unit. The top of Igneous Unit 10 is similar to the other units, with an uppermost chilled margin that is aphanitic but that reaches medium grain size about 2 m below this margin. The unit continues to coarsen downward until it reaches doleritic texture with groundmass plagioclase averaging 2.5 mm, clinopyroxene and olivine averaging 2 mm, and oxides averaging 1.5 mm. This much coarser grain size requires that the unit cooled slowly and was insulated from the thermally conductive seawater. Figure **F17** summarizes all mentioned characteristics of a typical igneous unit at Site U1580.

A distinct sign of sill intrusions into sedimentary successions is also a thermal overprint or baking (contact metamorphism) of the adjacent sedimentary lithology. Observed effects include bleaching or recrystallization (e.g., limestone transforms into marble) (e.g., Park, 1990). Similar reactions may also appear beneath thick lava flows but cannot be expected above such a flow (because any sediments deposited on an already existing lava body should be of younger age). The observed contact aureoles above Igneous Unit 2 (interval 392-U1580A-46R-1, 78–102 cm), Igneous Unit 3 (interval 48R-4, 66–68 cm), and the piece of marble between Igneous Units 4 and 5 (interval 48R-6, 126–130 cm) therefore provide compelling evidence for sill intrusions. Additional evidence for excess heating comes from other laboratory groups observations and data. For example, the organic-rich layer in interval 57R-1, 18–19 cm (between Igneous Units 7 and 8), shows thermogenic kerogen alteration and includes baked microfossils far beyond the grades expected at this relatively shallow depositional depth (466.18 m CSF-A; 467.815 m CCSF) (see **Geochemistry** and **Micropaleontology**).

In conclusion, we interpret the penetrated succession of igneous units and intercalated sediments at Site U1580 as a massive sill complex associated with the formation of the Agulhas Plateau. It was, however, totally unexpected to encounter such an extensive sill complex (possibly related to the two igneous bodies also tentatively interpreted as sills that were encountered 98 km away at the base of the previous Hole U1579D) near the center of the Agulhas Plateau and at such high stratigraphic position (with respect to the bulk of the seismically defined plateau basement). According to the biostratigraphically constrained ages, the sediments intercalating with the basalts in Hole U1580A are of early Turonian to late Cenomanian age (~94 Ma) (see **Micropaleontology**), meaning that if the igneous bodies are sills, they must be younger. The sediments encountered above and below the igneous units are often of a different type (e.g., cherts versus calcareous siltstones). This supports the often observed finding, made on better exposed terrestrial outcrops such as in the Karoo province, that sill intrusions commonly follow lithologic boundaries (e.g., Neumann et al., 2011).

Considering that most geodynamic models suggest a formation age of about 100 ± 5 Ma for the bulk of Agulhas Plateau volcanism, the igneous complex (regardless of whether it is deposited on

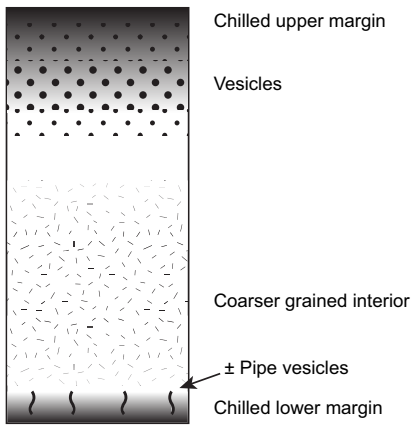

Figure F17. Idealized profile (not to scale) of a typical igneous unit in Hole U1580A. Specific features discussed in the text are indicated.

or intruded in slightly younger sediments) should represent a late-stage (or rejuvenated) event. Such rejuvenated magmatism of oceanic plateaus is often characterized by alkaline composition (e.g., Homrighausen et al., 2018; Hoernle et al., 2010). Preliminary shipboard pXRF spectrometry and inductively coupled plasma–atomic emission spectroscopy (ICP-AES) results, however, indicate a universal tholeiitic composition for these rocks (see **Geochemistry**).

Utilization of the Site U1580 basalts for detailed geochemical and petrological investigations is hampered by the considerable alteration of certain mineral phases (e.g., the complete replacement of olivine) and the interstitial groundmass. In contrast to submarine lava flows (which usually show the strongest alteration near the rock/seawater interface at their upper margins), complex, multilayered sill emplacements presumably create a longer lasting and extensive hydrothermal circulation cell not only affecting the intercalated sediments (see above) but also the igneous rocks themselves. As outlined above, the entire recovered igneous succession (independent of stratigraphic depth) shows moderate to severe alteration consistent with hydrothermal fluid-rock interaction. On the other hand, exceptional thick igneous intrusions like the >38 m Igneous Unit 10 almost act like a small magma chamber. Processes may include crystal-mesh interaction, segregation driven by the density contrast of magma and released volatiles or differentiation by gravitative crystallization, or magma replenishment and mixing. The three different subunits defined in Igneous Unit 10 likely reflect such processes and thus provide ample opportunities for further (more detailed) postcruise studies.

5. Micropaleontology

The 528.58 m thick succession cored at Site U1580 contains calcareous nannofossils, foraminifera, siliceous microfossils, and palynomorphs in varying abundance. In Hole U1580A, the sediment succession above ~407 m CSF-A consists of a thin layer (0–3.42 m CSF-A) of Pleistocene nannofossil-rich foraminiferal ooze (Lithostratigraphic Unit I; see **Lithostratigraphy**) overlying the lowermost Eocene–Coniacian strata (Lithostratigraphic Units II–III). Interbedded basalt and sediment was encountered between 407.46 and 490.54 m CSF-A (Lithostratigraphic Units VI–XIII); sediment in Lithostratigraphic Unit XIII was biostratigraphically dated to the late Cenomanian. The succession from 490.54 m CSF-A to the base of the cored succession at 528.58 m CSF-A consists of basalt (Lithostratigraphic Unit XIV).

Figure **F18** provides a comprehensive overview of the occurrence and preservation of microfossil groups documented in the Site U1580 sediments. Calcareous nannofossils are abundant and moderately to well preserved in the Paleogene and Pleistocene sediments (~0–200 m CSF-A). Abundance and preservation of calcareous nannofossils are more variable in the Cretaceous section, with some samples barren of nannofossils and preservation generally poor to moderate. Despite variable preservation and abundance, nannofossils are present throughout the recovered sediment and provide excellent biostratigraphic control for the Paleogene and reasonably good control for the Cretaceous (Figure **F19**; Table **T5**). Foraminifera are abundant and generally well preserved in the upper part of Site U1580. Below ~115 m CSF-A, foraminiferal abundance decreases and preservation deteriorates, although in some intervals of poor preservation delicate morphological features such as pore structures are preserved. Radiolarian fragments as well as pyritized diatoms and radiolarians were encountered in only a few samples from Site U1580. Trace numbers of palynofacies consisting of black phytoclasts are present in the Paleocene to lower Eocene sediments, whereas dinoflagellate cysts (dinocysts), miospores, and black phytoclasts are rare to abundant in the Cretaceous sediments above the basalt, and some samples show thermal alteration in the color of the palynomorphs.

5.1. Calcareous nannofossils

We examined all RCB core catcher samples from Holes U1580A and U1580B, as well as additional samples from split core sections for selected intervals, to establish a calcareous nannofossil biostratigraphy for Site U1580 (Figure **F19**; Table **T5**). Additional samples from split-core sections were used to refine ages for intervals of interest including the Paleocene/Eocene boundary and K/Pg boundary and when core catcher samples were barren or only contained sparse nannofossil

assemblages. Calcareous nannofossil assemblage distribution data are based on shipboard observations, which focused on identification and tabulation of species that are age diagnostic; therefore, the recorded assemblage may not be fully representative of the entire nannofossil assemblage (Table **T6**). Photomicrographs of selected nannofossils are shown in Figure **F20**.

The uppermost 3.42 m of Hole U1580A (Lithostratigraphic Unit I) consists of middle–upper Pleistocene foraminiferal ooze with nannofossils overlying nannofossil ooze with foraminifera dated to the earliest Eocene (Tables **T5**, **T6**). Calcareous nannofossils are generally abundant and moderately well preserved in the Eocene–Paleocene interval (Lithostratigraphic Subunits IIa and IIb; 3.42–207.11 m CSF-A). Nannofossils are present in most Cretaceous samples examined but are rare to common in abundance and poorly to moderately preserved (Lithostratigraphic Subunit IIc and Lithostratigraphic Units III, XI, and XIII). The oldest sediment recovered from Hole U1580A is dated to the latest Cenomanian in Sample 392-U1580A-60R-CC, 0–5 cm (481.54 m CSF-A). Hole U1580B recovered a second copy of the uppermost Paleocene to lower Eocene interval, including the Paleocene/Eocene boundary (Table **T6**).

5.1.1. Pleistocene

Hole U1580A recovered 3.42 m of Pleistocene foraminiferal ooze with nannofossils (Lithostratigraphic Unit I). Samples 392-U1580A-1R-1, 2 cm (0.02 m CSF-A), and 1R-3, 75 cm (3.05 m CSF-A), contain a late Pleistocene assemblage with abundant *Emiliania huxleyi*; common *Gephyrocapsa* spp. (including *Gephyrocapsa oceanica*), *Coccolithus pelagicus*, and *Umbilicosphaera sibogae*; and frequent *Helicosphaera carteri* (Table **T6**). Other taxa, including *Coccolithus braarudii*, *Pontosphaera japonica*, *Pontosphaera multipora*, *Rhabdosphaera* spp., and *Syracosphaera* spp., are present in rare to few numbers in these samples. The presence of *E. huxleyi* (biohorizon base = 290 ka) in both samples indicates that the sediment is younger than 290 ka and within Zone NN21 (Martini, 1971). Numerous reworked Paleogene nannofossil taxa are recorded mostly in Sample 1R-1, 2 cm (0.02 m CSF-A), and less commonly in Sample 1R-3, 75 cm (3.05 m CSF-A).

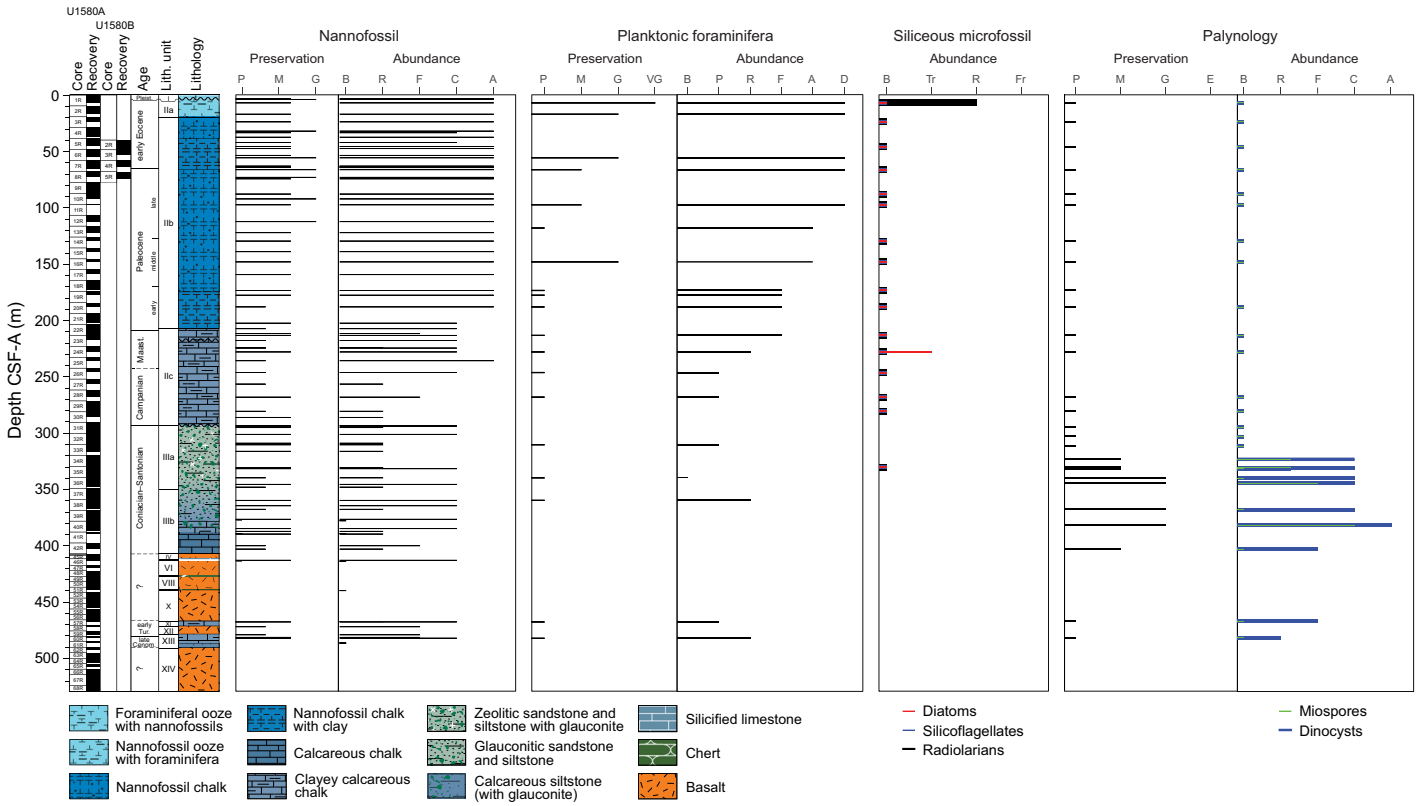

Figure F18. Overview of the preservation and abundance of nannofossils, planktonic foraminifera, siliceous microfossils and palynomorphs studied at Site U1580. Abundance: B = barren, P = present, Tr = trace, R = rare, F = few, Fr = frequent, C = common, A = abundant, D = dominant. Preservation: P = poor, M = moderate, G = good, VG = very good, E = excellent.

5.1.2. Eocene

Site U1580 recovered an expanded lowermost Eocene and Paleocene/Eocene boundary interval with very high sedimentation rates (see **Chronostratigraphy**). Calcareous nannofossils are abundant throughout the lowermost Eocene of Hole U1580A, and preservation is moderate to good. Biohorizon base *Tribrachiatus orthostylus* (54.30 Ma; n1 in Figure **F31** and Table **T5**), which falls within Zone NP10 and marks the base of Zone CNE3 (Agnini et al., 2014), is found in Sample 1R-CC, 15–20 cm (6.77 cm CSF-A). Pervasive but minor reworking of Cretaceous and Paleocene species precluded identification of biohorizon top *Fasciculithus* spp. (55.60 Ma), which marks the top of Zone CNE1. However, two bioevents that fall within Zone CNE2 were identified: (1) biohorizon base *Tribrachiatus contortus* (54.7 Ma; n2, same figure) is recorded in Sample 4R-3, 151 cm (33.25 m CSF-A), and (2) biohorizon base *Discoaster diastypus* (54.89 Ma; n3, same figure) is identified in Sample 5R-2, 151 cm (41.82 m CSF-A). The interval of increased clay content associated with the PETM was identified both visually as a distinct change in color (see **Lithostratigraphy**) and through physical properties data (see **Physical properties**). Calcareous nannofossil biostratigraphy confirmed that the sediment above the color change contains one of the markers for the PETM, the biohorizon base *Rhomboaster* spp. (56.00 Ma; n4, same figure) in Sample 7R-4, 60 cm (63.32 m CSF-A) (e.g., Bybell and Self-Trail, 1994; Kahn and Aubry, 2004; Self-Trail et al., 2012). This event was also identified in Hole U1580B in the core catcher sample above the color change inferred to be the PETM (Sample 392-U1580B-3R-CC, 21–22 cm; 53.51 m CSF-A).

5.1.3. Paleocene

The middle and upper Paleocene sediment at Site U1580 is characterized by diverse and moderately preserved calcareous nannofossil assemblages with common to abundant *Toweius pertusus*,

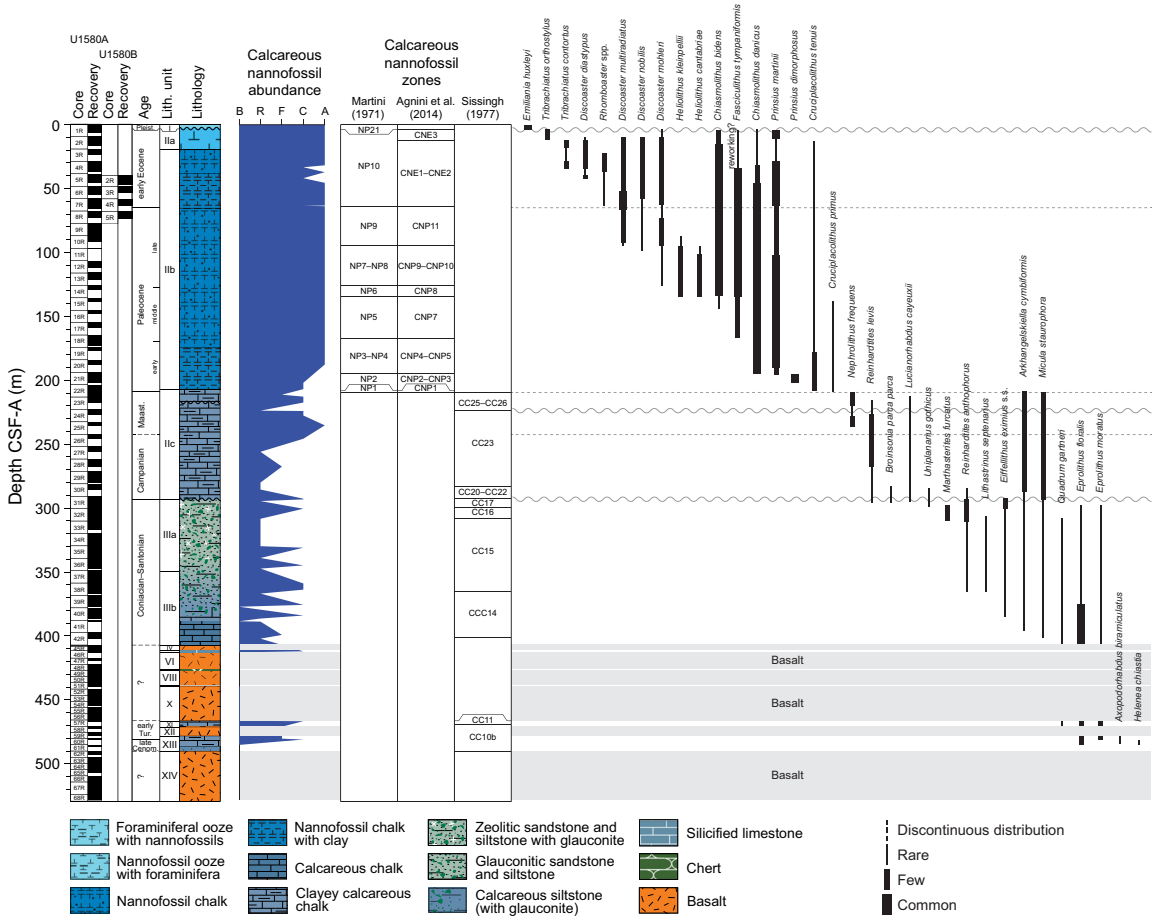

Figure F19. Calcareous nannofossil abundance, zones, and distribution of biostratigraphically important taxa, Site U1580. Dashed lines show epoch boundaries. Undulating lines represent inferred unconformities. Abundance: B = barren, R = rare, F = few, C = common, A = abundant.

Toweius callosus, *Toweius eminens*, *C. pelagicus*, *Chiasmolithus bidens*, *Chiasmolithus danicus*, and *Fasciculithus tympaniformis* (Table **T6**). Other species including early members of the *Discoaster* lineage (e.g., *Discoaster mohleri*, *Discoaster nobilis*, and *Discoaster multiradiatus*), *C. pelagicus*, and *Heliolithus kleinpellii* are also present. Although nannofossils are common to abundant in the lower Paleocene section, diversity is low. The assemblage is dominated by *Prinsius martinii* and *Prinsius bisulcus* with common *T. pertusus* in the upper part of the lower Paleocene. In the lowermost Paleocene, only a few species are present, including *Cruciplacolithus primus*, *Cruciplacolithus tenuis*, and *C. pelagicus*, together with some K/Pg survivor taxa (*Markalius inversus* and *Zeugrhabdotus sigmoides*). The Paleocene stratigraphy at Site U1580 is defined using eight nannofossil datums.

Biohorizon base *D. multiradiatus* (57.32 Ma; n5 in Figure **F31** and Table **T5**) is recognized in Sample 392-U1580A-10R-CC, 10–15 cm (91.96 m CSF-A), marking the base of Zones NP9 and CNP11. Biohorizon base *D. nobilis* (57.49 Ma; n6, same figure) is identified in Sample 11R-CC, 18–23 cm (97.18 m CSF-A), and falls within Zones NP8 and CNP10. Biohorizon base *D. mohleri* (58.97 Ma; n7, same figure), representing the evolution of this genus and marking the base of Zones NP7 and CNP9, is recognized in Sample 13R-5, 103 cm (121.90 m CSF-A). Biohorizon base *H. kleinpellii* (59.36 Ma; n8, same figure), identified in Sample 14R-CC, 5–10 cm (129.27 m CSF-A), marks the base of Zone NP6 and falls within Zone CNP8.

Biohorizon base *F. tympaniformis* (61.27 Ma; n9 in Figure **F31**), which marks the base of Zone NP5 and is located within the lower part of Zone CNP7, is documented in Sample 392-U1580A-

Table T5. Biostratigraphic datums, Site U1580. Datum numbers correspond to those shown in Figure F31. T = top, B = bottom. **Download table in CSV format.**

Datum number	Datum	Age (Ma)	Core, section, interval (cm)	Depth CSF-A (m)	Next sample above (below) for T (B) Core, section, interval (cm)	Depth CSF-A (m)	Midpoint depth CSF-A (m)
			392-U1580A-		392-U1580A-		
f1	T *Chiloguembelina wilcoxensis*	53.6	1R-CC, 15–20	6.77	1R-1, 0 (mudline)	0.00	3.39
n1	B *Tribrachiatus orthostylus*	54.30	1R-CC, 15–20	6.77	2R-CC, 19–24	16.73	11.75
n2	B *Tribrachiatus contortus*	54.70	4R-3, 151	33.25	4R-CC, 14–19	37.16	35.21
n3	B *Discoaster diastypus*	54.89	5R-2, 151	41.82	5R-CC, 17–22	45.49	43.66
f2	T *Acarinina subsphaerica*	54.905	11R-CC, 15–20	97.18	7R-CC, 6–11	66.04	81.61
n4	B *Rhomboaster* spp.	56.00	7R-4, 60	63.32	7R-4, 71	63.43	63.38
f3	T *Igorina tadjikistanensis*	56.0	7R-CC, 6–11	66.04	6R-CC, 12–17	55.48	60.76
n5	B *Discoaster multiradiatus*	57.32	10R-CC, 10–15	91.96	11R-CC, 18–23	97.18	94.57
n6	B *Discoaster nobilis*	57.49	11R-CC, 18–23	97.18	12R-CC, 15–20	112.10	104.64
n7	B *Discoaster mohleri*	58.97	13R-5, 103	121.90	14R-CC, 5–10	129.27	125.59
n8	B *Heliolithus kleinpellii*	59.36	14R-CC, 5–10	129.27	15R-CC, 13–18	138.76	134.02
n9	B *Fasciculithus tympaniformis*	61.27	17R-CC, 3–8	159.09	18R-CC, 21–26	173.14	166.12
n10	B *Neochiastozygus perfectus*	61.82	18R-CC, 21–26	173.14	19R-CC, 8–13	177.28	175.21
n11	B *Chiasmolithus danicus*	64.53	20R-CC, 21–26	187.76	21R-CC, 8–13	202.12	194.94
n12	B *Cruciplacolithus tenuis*	65.70	22R-3, 55	207.07	—	—	207.07
n13	T Cretaceous nannoflora	66.04	22R-4, 135	209.25	—	—	209.25
f4	T *Planohedbergella aspera*	68.24	22R-CC, 15–20	212.99	20R-CC, 21–26	187.76	200.38
f5	T *Planoheterohelix planata*	68.24	22R-CC, 15–20	212.99	20R-CC, 21–26	187.76	200.38
n14	T *Reinhardtites levis*	70.14	24R-1, 80	223.90	23R-CC, 6–11	217.55	220.73
f6	T *Archaeoglobigerina cretacea*	72.36	32R-CC, 29–34	310.07	28R-CC, 18–23	267.74	288.91
n15	T *Reinhardtites anthophorus*	74.47	30R-CC, 0–5	285.74	29R-CC, 0–5	280.29	283.02
n16	T *Eiffellithus eximius* s.s.	75.85	31R-2, 42	292.91	30R-CC, 0–5	285.74	289.33
n17	T *Eprolithus floralis*	84.0	31R-CC, 15–20	300.78	31R-2, 95	293.44	297.11
dc1	T *Heterosphaeridium difficile*	83.9	35R-CC, 25–30	339.38	35R-1, 128–130	331.08	335.23
dc2	T *Balteocysta perforata*	85.2	36R-4, 19–20	344.10	35R-CC, 25–30	339.38	341.74
n18	T *Lithastrinus septenarius*	85.30	32R-6, 65	308.61	31R-CC, 15–20	300.78	304.70
dc3	B *Impagidinium cristatum*	85.9	40R-3, 21–24	381.33	42R-CC, 22–27	402.54	391.94
n19	B *Micula staurophora*	87.18	42R-2, 43	399.63	42R-CC, 22–27	402.54	401.09
dc4	presence *Circulodinium distinctum* ("younger than" age)	87.9	42R-CC, 22–27	402.54	—	—	402.54
n20	B *Eprolithus moratus*	93.73	59R-CC, 8–10	478.61	60R-1, 24	480.84	479.73
n21	B *Quadrum gartneri*	93.75	57R-CC, 13–16	467.21	58R-1, 58	471.48	469.35
n22	T *Helenea chiastia*	93.90	60R-CC, 0–5	481.54	60R-1, 24	480.84	481.19
n23	T *Axopodorhabdus biramiculatus*	93.98	60R-1, 24	480.84	59R-CC, 8–10	478.61	479.73

Table T6. Distribution of calcareous nannofossils, Site U1580. **Download table in CSV format.**

17R-CC, 3–8 cm (159.09 m CSF-A). Biohorizon base *Neochiastozygus perfectus* (61.82 Ma; n10, same figure), identified in Sample 18R-CC, 21–26 cm (173.14 m CSF-A), is located within Zones NP4 and CNP5. Biohorizon base *C. danicus* (64.53 Ma; n11, same figure), documented in Sample 20R-CC, 21–26 cm (187.76 m CSF-A), marks the base of Zone NP3; the event also falls within Zone CNP3. Biohorizon base *C. tenuis* (65.70 Ma; n12, same figure), documented in Sample 22R-3, 55 cm (207.07 m CSF-A), is located within the lower Zones NP2 and CNP2.

5.1.4. Cretaceous/Paleogene boundary

The K/Pg boundary was recovered in Core 392-U1580A-22R; however, its exact placement is not clear (see **Lithostratigraphy**). Calcareous nannofossil biostratigraphy confirms that it falls below Sample 392-U1580A-22R-3, 55 cm (207.07 m CSF-A), which contains an early Paleocene assemblage that includes *C. primus*, *C. tenuis* (biohorizon base = 65.70 Ma; n12 in Figure **F31** and Table **T5**), micron-sized calcite particles (micarb), and a few survivor taxa, including *M. inversus* and *Z. sigmoides*. Sample 22R-4A, 135 cm (209.25 m CSF-A), contains rare specimens of the Cretaceous taxon *Micula* (biohorizon top = 66.04 Ma; n13, same figure) and no Paleocene species, and Sample

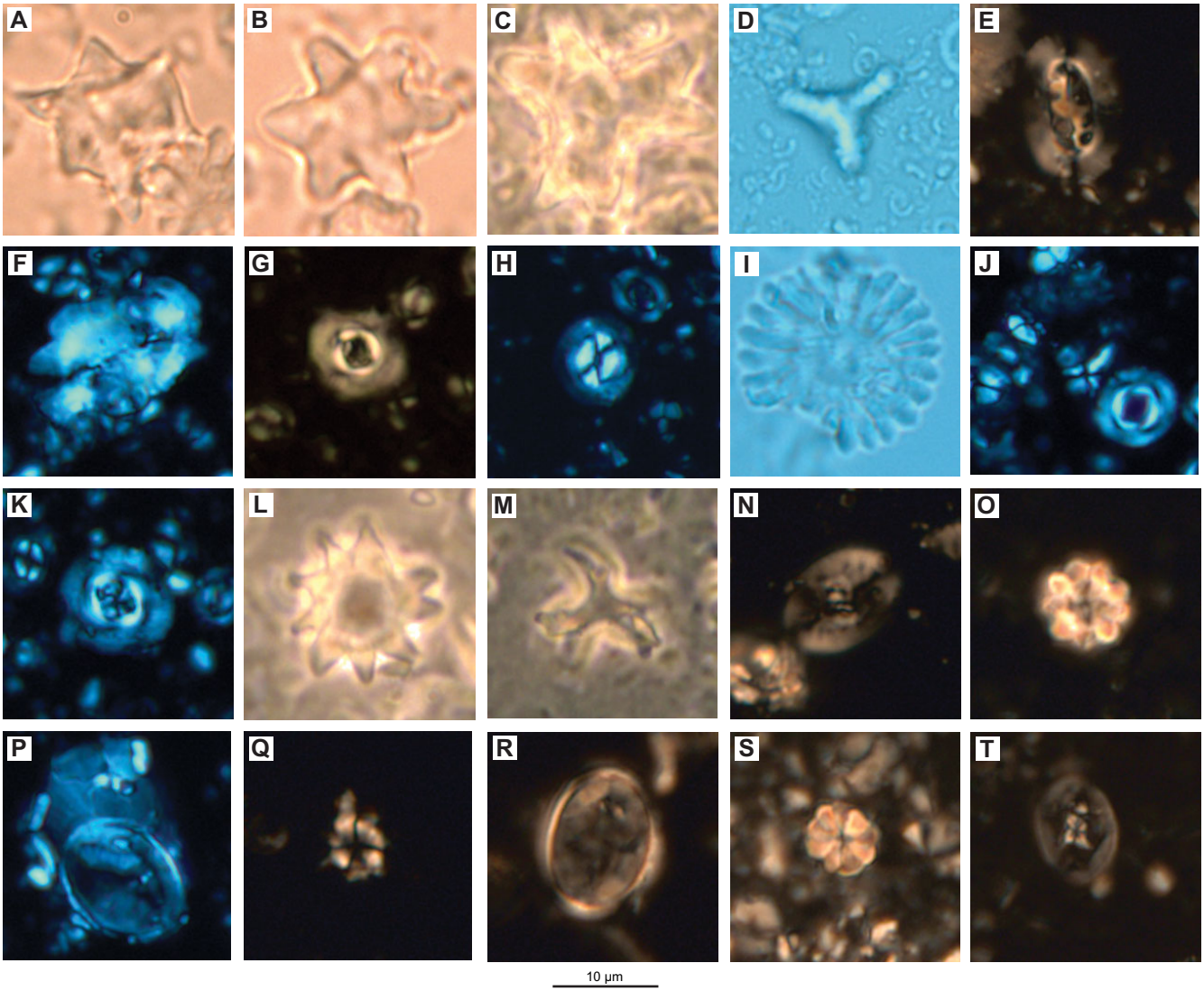

Figure F20. Selected Paleogene and Cretaceous calcareous nannofossils, Hole U1580A. Scale bars = 10 µm. A. *Rhomboaster cuspis* (7R-4, 5 cm). B. *Rhomboaster bramlettei* (3R-CC). C. *Tribrachiatus contortus* (4R-3, 151 cm). D. *Tribrachiatus orthostylus* (1R-3, 134 cm). E. *Ellipsolithus bollii* (7R-CC). F. *Ellipsolithus macellus* (1R-3, 134 cm). G. *Toweius callosus* (1R-3, 134 cm). H. *Coccolithus pelagicus* (1R-3, 134 cm). I. *Discoaster salisburgensis* (7R-4, 5 cm). J. *Sphenolithus editus* (1R-3, 134 cm). K. *Toweius gammation* (1R-3, 134 cm). L. *Discoaster araneus* (4R-CC). M. *Marthasterites furcatus* (32R-6, 65 cm). N. *Reinhardtites levis* (25R-CC). O. *Eprolithus floralis* (32R-6, 65 cm). P. *Kamptnerius magnificus* (23R-CC). Q. *Lithastrinus septenarius* (31R-2, 95 cm). R. *Gartnerago segmentatum* (46R-1, 66 cm). S. *Quadrum eneabrachium* (31R-2, 95 cm). T. *Axopodorhabdus biramiculatus* (=*Axopodorhabdus albianus*; 60R-CC).

22R-6, 60 cm (211.44 m CSF-A) contains a moderately preserved late Maastrichtian assemblage that includes common *Micula* spp. and few *Kamptnerius magnificus*, *Cribrosphaerella daniae*, *Nephrolithus frequens*, *Arkhangelskiella cymbiformis*, *Prediscosphaera cretacea*, and *Watznaueria barnesiae* (Table **T6**). We tentatively place the K/Pg boundary above Sample 22R-4A, 135 cm (209.25 m CSF-A), based on the presence of Cretaceous taxa and absence of Paleocene species.

5.1.5. Maastrichtian to Campanian

In general, the calcareous nannofossil assemblages in the Upper Cretaceous sediments of Site U1580 are relatively diverse with common numbers of specimens and are moderately to poorly preserved. Only a few samples are barren of calcareous nannofossils in the lowermost sediments of Site U1580.

Samples 392-U1580A-22R-6, 60 cm, to 31R-2, 42 cm (211.44–292.91 m CSF-A), are dated to the Campanian–Maastrichtian. Maastrichtian calcareous nannofossil assemblages vary from sparse to abundant and are moderately to poorly preserved. Common species include *N. frequens*, *K. magnificus*, *Micula murus*, and *A. cymbiformis*, whereas *Micula staurophora*, *Biscutum magnum*, *Reinhardtites levis*, *Eiffellithus gorkae*, *C. daniae*, *Cribrosphaerella ehrenbergii*, and *W. barnesiae* are present in rare to few numbers (Table **T6**). Biohorizon top *R. levis* (70.14 Ma; n14 in Figure **F31** and Table **T5**), identified in Sample 24R-1, 80 cm (223.90 m CSF-A), marks the base of Zone CC25 (Sissingh, 1977; Perch-Nielsen, 1985) and indicates that the interval above comprises Zones CC25–CC26. This event falls just below an unconformity inferred from abrupt changes in paleomagnetic inclination (see **Paleomagnetism**) and therefore may not represent its true last appearance datum. Other marker taxa for the early Maastrichtian are absent, very sparse, or only present well below their dated extinction level in the Tethyan region (e.g., Gradstein et al., 2020) at Site U1580, including *Tranolithus orionatus*, *Uniplanarius trifidus*, *Monomarginatus quaternarius*, and *Broinsonia parca constricta* (Table **T6**), which are excluded from the age-depth model. Biohorizon tops *Uniplanarius gothicus* (72.48 Ma) and *Reinhardtites anthophorus* (74.47 Ma; n15, same figure) are identified in Sample 30R-CC, 0–5 cm (285.74 m CSF-A), and biohorizon top *Eiffellithus eximius* s.s. (75.85 Ma; n16, same figure) is recorded in Sample 31R-2, 42 cm (292.91 m CSF-A), indicating a mid-Campanian age older than 75.85 Ma and younger than 80.97 Ma based on the absence of *Marthasterites furcatus*.

5.1.6. Santonian to Coniacian

Core 392-U1580A-31R shows a downcore color change from brown to red to green, marking the Lithostratigraphic Unit II–III transition (see **Lithostratigraphy**). Samples from Section 31R-2 contain a mid-Campanian assemblage (see **Maastrichtian to Campanian**), whereas Sample 31R-CC, 15–20 cm (300.78 m CSF-A), contains a distinctly different assemblage with biohorizon tops *M. furcatus* (80.97 Ma) and *Eprolithus floralis* (84.0 Ma; n17 in Figure **F31** and Table **T5**). This succession of biohorizons indicates a hiatus spanning much of the early and middle Campanian between ~76 and at least 83.7 Ma at Site U1580.

Lithostratigraphic Unit III falls below this hiatus and consists of green zeolitic sand-, silt-, and claystone with glauconite and calcareous chalk. This unit includes numerous coarse-grained beds with sharp bases that fine upward, suggesting rapid deposition (see **Lithostratigraphy**). Calcareous nannofossils are present throughout this unit but in varying numbers and preservation state. Despite this, several datums can be identified. Near the top of the unit, Sample 392-U1580A-32R-6, 65 cm (308.61 m CSF-A), contains a concurrence of several bioevents, including biohorizon tops *Lithastrinus septenarius* (85.30 Ma; n18 in Figure **F31**) and *Quadrum gartneri* (85.09 Ma), together with biohorizon base *M. furcatus* (89.86 Ma), suggesting a late Santonian age for the top of Lithostratigraphic Unit III. Biohorizon base *R. anthophorus* (86.57 Ma) is identified in Sample 38R-5, 20 cm (364.14 m CSF-A), indicating the base of Zone CC15. Biohorizon base *M. staurophora* (87.18 Ma; n19, same figure), which marks the base of Zone CC14, is identified in Sample 42R-2, 43 cm (399.63 m CSF-A). This event is found ~8 m above the uppermost basalt recovered at Site U1580 (Lithostratigraphic Unit IV; 407.46–411.76 m CSF-A; 407.46–411.76 m CCSF; we include CCSF depths for Lithostratigraphic Units IV–XIV because there is significant overlap of some cores on the CSF-A depth scale due to >100% recovery). The assemblage throughout Litho-

stratigraphic Unit III is mainly characterized by common *W. barnesiae* and *T. orionatus* as well as typical high-latitude species such as *Seribiscutum primitivum* and *Repagulum parvidentatum*.

5.1.7. Turonian to Cenomanian

The lowermost succession at Site U1580, from Sample 392-U1580A-43R-CC, 6 cm, to the base of the hole (407.46–528.58 m CSF-A; 407.46–529.59 m CCSF), is dominated by basalt interlayered with thin intervals of sediment (Lithostratigraphic Units IV–XIV). Some of these interbedded sediments yielded relatively abundant and well preserved calcareous nannofossil assemblages. Lithostratigraphic Unit XI comprises calcareous chalk, silicified limestone, and nannofossil-rich claystone. Within this unit, Sample 57R-CC, 13–16 cm (467.21 m CSF-A; 468.84 m CCSF), contains biohorizon base *Q. gartneri* (93.75 Ma; n21 in Figure **F31** and Table **T5**), which marks the base of Zone CC11 and falls just above the Cenomanian/Turonian boundary. Below another basalt interval (Lithostratigraphic Unit XII; 471.60–478.53 m CSF-A; 471.60–478.53 m CCSF), Lithostratigraphic Unit XIII (478.53–490.54 m CSF-A; 478.53–490.54 m CCSF) also contains calcareous chalk, claystone, siltstone and rubbles of basalt, and biohorizon base *Eprolithus moratus* (93.73 Ma; n20, same figure) is found in Sample 59R-CC, 8–10 cm (478.61 m CSF-A; 478.61 m CCSF), at the top of this unit. Two biohorizons indicative of the latest Cenomanian are also found in this unit. In Sample 60R-1, 24 cm (480.84 m CSF-A; 480.84 m CCSF), biohorizon top *Axopodorhabdus biramiculatus* (=*Axopodorhabdus albianus*; 93.98 Ma; n23, same figure) is recorded. Biohorizon top *Helenea chiastia* (93.90 Ma; n22, same figure), which marks the base of Subzone CC10b, is found in Sample 60R-CC, 0–5 cm (481.54 CSF-A; 481.54 m CCSF). The latest Cenomanian calcareous nannofossil assemblages include common *W. barnesiae*, *T. orionatus*, *E. floralis*, and frequent numbers of *Rhagodiscus*, *Gartnerago*, and *Helicolithus trabeculatus* (Table **T6**) and suggest a stronger influence of mid- to low-latitude assemblages compared to the southern high-latitude assemblages of the Campanian and Maastrichtian at Site U1580.

5.2. Foraminifera

A total of 20 core catcher samples and 1 discrete sample from a split core section from Hole U1580A were examined for planktonic and benthic foraminifera from the >63 µm size fraction. Specimens from the >150 and 63–150 µm fractions were similar, and the 63–150 µm fractions were examined regularly to ensure smaller species were not missed. All shipboard results are reported in Tables **T7** and **T8**. In Lithostratigraphic Unit I and Lithostratigraphic Subunit IIa (0–16.73 m CSF-A), planktonic foraminifera are very abundant and preservation is very good (Sample 392-U1580A-1R-1, 0 cm; 0 m CSF-A). Foraminifera in samples from the top of the hole to ~97 m CSF-A (Sample 11R-CC, 18–23 cm) were easily disaggregated from the sediments and show little evidence of recrystallization or dissolution. Preservation in the upper part of Lithostratigraphic Subunit IIb (19.40–100 m CSF-A) ranges from good (Sample 6R-CC, 12–17 cm; 55.48 m CSF-A) to moderate (Sample 11R-CC, 18–23 cm; 97.18 m CSF-A) as fragmentation becomes more prevalent. Sediment samples in the lower part of Lithostratigraphic Subunit IIb between Samples 13R-2, 6–8 cm (117.73 m CSF-A), and 24R-CC, 19–24 cm (227.70 m CSF-A), required disaggregation by soaking and stirring in water. Between Samples 28R-CC, 18–23 cm, and 60R-CC, 0–5 cm (267.74–481.54 m CSF-A), samples required soaking in >5% H_2O_2 to extract foraminifera. Preservation is poor from Sample 13R-2, 6–8 cm (117.73 m CSF-A), to the bottom of the hole. Sample 32R-CC, 29–34 cm (310.07 m CSF-A), shows excellent preservation of delicate morphological structures (such as pores) (Figure **F21G4, F21G5**). Although not abundant, foraminifera are present as deep as Sample 60R-CC, 0–5 cm (481.54 m CSF-A; 481.54 m CCSF).

The foraminiferal assemblage in Sample 392-U1580A-1R-CC, 15–20 cm (6.77 m CSF-A), differs greatly from that in the mudline (Sample 1R-1, 0 cm). The biohorizon tops of *Globorotalia australiformis* (Zone E9; 43.4 Ma), *Subbotina patagonica* (Zone E8; 43.85–45.72 Ma), and *Chiloguembelina wilcoxensis* (Zone E4; 53.6 Ma; f1 in Figure **F31** and Table **T5**) are found in Sample 1R-CC,

Table T7. Distribution of planktonic foraminifera, Site U1580. **Download table in CSV format.**

Table T8. Distribution of benthic foraminifera, Site U1580. **Download table in CSV format.**

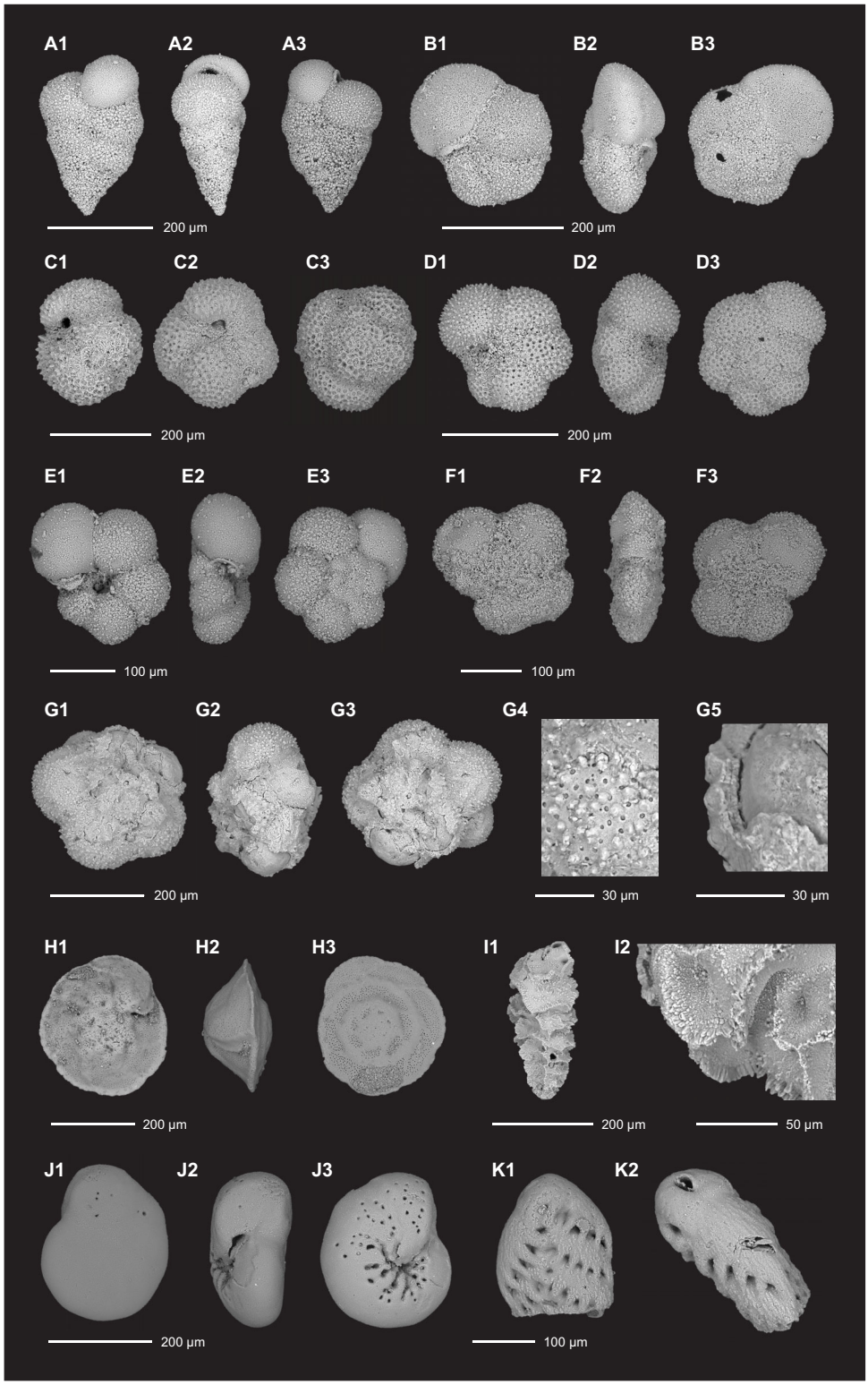

Figure F21. Selected Paleogene and Cretaceous planktonic and benthic foraminifera, Hole U1580A. A (1–3). *Chiloguembelina wilcoxensis* (scanning electron microscopy [SEM] P1: 392-U1580A-1R-CC). B (1–3). *Globanomalina australiformis* (SEM P4: 392-U1580A-1R-CC). C (1–3). *Acarinina subsphaerica*. (SEM P24: 392-U1580A-6R-CC). D (1–3). *Acarinina pentacamerata* (SEM P29: 392-U1580A-7R-CC). E (1–3). *Muricohedbergella sliteri* (SEM N5: 392-U1580A-22R-CC). F (1–3). *Planohedbergella subcarinatus* (SEM N12: 392-U1580A-22R-CC). G (1–5). *Archaeoglobigerina cretacea* (SEM N17: 392-U1580A-32R-CC); (4, 5) show the unique preservation of specimens. H (1–3). *Nuttallides truempyi* (SEM O25: 392-U1580A-6R-CC). I (1, 2). *Tappanina* sp. (SEM M2: 392-U1580A-6R-CC). J (1–3). *Gavelinella* sp. (SEM M7: 392-U1580A-7R-CC). K (1, 2). *Bolivinoides* sp. (SEM).

15–20 cm (6.77 m CSF-A), suggesting an age between 43.4 and 53.6 Ma. The top of the *Acarinina subsphaerica* Zone (Zone E3; 54.61–55.20 Ma; f2, same figure) is identified based on the presence of the nominative species in Sample 11R-CC, 15–20 cm (97.18 m CSF-A). The Paleocene/Eocene boundary interval is identified in Sample 7R-CC, 6–11 cm (66.04 m CSF-A), based on the presence of *Igorina tadjikistanensis* (Zone P5; 56.0 Ma; f3, same figure). This is consistent with observations from calcareous nannofossil biostratigraphy, a change in color in the sediment (see **Lithostratigraphy**), and changes in physical properties data (see **Physical properties**) that indicate that the PETM is present in Section 7R-4. There is also a transition in the benthic foraminiferal assemblage across the Paleocene/Eocene boundary interval at Site U1580. The epifaunal to shallow infaunal genus *Cibicidoides* is present in Samples 1R-CC, 15–20 cm, to 6R-CC, 12–17 cm (6.77–55.48 m CSF-A), whereas *Gavelinella* seems to occupy this epifaunal to shallow infaunal microhabitat in Samples 7R-CC, 6–11 cm, to 37R-CC, 28–33 cm (66.04–359.32 m CSF-A). *Nuttallides* also shows a change across the Paleocene/Eocene boundary from *Nuttallides florealis* in the Paleocene to *Nuttallides truempyi* in the Eocene. These transitions in benthic assemblages may be reflective of the PETM, when benthic foraminifera experienced a major extinction event (e.g., Thomas, 2007).

Maastrichtian planktonic foraminifera including *Planohedbergella aspera* (*Abathomphalus mayaroensis* Zone; 67.30–69.18 Ma; f4 in Figure **F31**) and *Planoheterohelix planata* (*A. mayaroensis* Zone; 67.30–69.18 Ma; f5, same figure) are present in Sample 392-U1580A-22R-CC, 15–20 cm (212.99 m CSF-A). Sample 32R-CC, 29–34 cm (310.07 m CSF-A), which is characterized by excellent morphologic preservation, also contains *Archaeoglobigerina cretacea* (*Gansserina gansseri* Zone; 71.75–72.97 Ma; f6, same figure) (Figure **F21G**). Other biogenic materials observed include ostracods, fish teeth, and radiolarians (Table **T7**).

In the >150 μm size fractions of Samples 392-U1580A-32R-CC, 29–34 cm (310.07 m CSF-A), and 37R-CC, 28–33 cm (359.32 m CSF-A), calcite spar, which requires open pore space to form, is present. Further analyses of preservation and diagenesis on these sections will be conducted onshore.

5.3. Siliceous microfossils

A total of 17 core catcher samples were analyzed for siliceous microfossils. Radiolarian fragments are present in the lower Eocene–Paleocene interval of Site U1580 in Samples 392-U1580A-1R-CC, 15–20 cm (6.77 m CSF-A); 18R-CC, 21–26 cm (173.14 m CSF-A); and 20R-CC, 21–26 cm (187.76 m CSF-A). Siliceous microfossils are barren in all remaining studied samples (Table **T9**). Pyritized radiolarian fragments were observed in Sample 3R-CC, 12–17 cm (23.60 m CSF-A; lower Eocene), and a pyritized diatom fragment was observed in Sample 24R-CC, 19–24 cm (227.70 m CSF-A; Maastrichtian).

5.4. Palynology

From the sedimentary part of the recovered succession at Site U1580, 27 samples (19 core catcher samples and 8 discrete split-core samples) were studied for palynology (Table **T10**). For the discrete samples, fine-grained, laminated, darker intervals were selected to maximize the chance of organic matter preservation. The productive samples for palynology therefore do not necessarily imply preservation of palynomorphs throughout the succession. Samples from Cores 392-U1580A-1R through 33R (6.77–311.24 m CSF-A) contain trace amounts of palynofacies (consisting of black phytoclasts) but are barren of dinocysts and miospores. Preservation of dinocysts and miospores is moderate to good in Cores 34R–42R (322.74–402.59 m CSF-A). Palynofacies in this interval contain rare to abundant black phytoclasts and dinocysts (Figure **F22**) with rare to common miospores. In particular, the dinocysts show varying degrees of thermal maturity in their color, from translucent to dark brown (Figure **F23**). Samples 57R-1, 18–19 cm (466.185 m CSF-A), and 60R-1, 51–53 cm (481.11 m CSF-A), contain abundant black phytoclasts and dark brown/black, evidently thermally matured, fragmented dinocysts.

5.4.1. Dinocysts

Dinocyst assemblages are diverse in Lithostratigraphic Unit III (293.51–407.46 m CSF-A) and contain typical early Santonian–late Turonian species: *Balteocysta perforata*, *Circulodinium distinctum*, *Conosphaeridium striatoconus*, *Coronifera oceanica*, *Cribroperidinium cooksoniae*, *Heterosphaeridium spinaconjunctum*, *Kallosphaeridium ringnesiorum*, and *Pervosphaeridium pseudohystrichodinium* (Table **T10**). We note the biohorizon top of *Heterosphaeridium difficile* (83.9 Ma; dc1 in Figure **F31** and Table **T5**) in Sample 392-U1580A-35R-CC, 25–30 cm (339.38 m CSF-A) and the biohorizon top of *B. perforata* (85.2 Ma; dc2, same figure) in Sample 36R-4, 19–20 cm (344.10 m CSF-A). The biohorizon base of *Impagidinium cristatum* (85.9 Ma; dc3, same figure) is in Sample 40R-3, 21–24 cm (381.33 m CSF-A). The lowermost sample that contains an interpretable dinocyst assemblage is Sample 42R-CC, 22–27 cm (402.54 m CSF-A). This sample is ~5 m above the uppermost basalt (Lithostratigraphic Unit IV; 407.46–411.76 m CSF-A) and shows signs of maturity in the color of the macerals. It also contains abundant *C. distinctum*, which makes it younger than 87.9 Ma (dc4, same figure). Reworking of Cenomanian–early Turonian dinocysts (e.g., *Hapsocysta dictyota*, *Fromea amphora*, *Cometodinium obscurum*, *Codoniella campanulata*) is common in the dinocyst-bearing interval. It could also be that these species had a longer stratigraphic range in the Southwest Indian Ocean than in the region where they were calibrated to the geologic timescale (Gradstein et al., 2020), which is mostly in the North Atlantic Ocean (Pearce, 2000).

There is distinct variability in color in the dinocyst assemblages from translucent to dark brown-black. Most samples have a translucent dinocyst assemblage, but in some samples (e.g., 392-U1580A-35R-CC, 25–30 cm; 339.38 m CSF-A), all dinocysts, including those species that are translucent in other samples, are medium brown (Figure **F23**). Samples 57R-1, 19 cm (466.185 m CSF-A; 467.815 m CCSF; within Lithostratigraphic Unit XI), and 60R-1, 51–53 cm (481.11 m CSF-A; 481.11 m CCSF; within Lithostratigraphic Unit XIII), were taken from the sediments intercalated between basalt units and contain dinocysts that are dark brown to black and are fragmented to an extent that species identification was difficult. For almost all samples, the coloration of the dinocysts is consistent within a sample, except for Sample 40R-3, 21–24 cm (381.33 m CSF-A), which contains a mix of translucent and medium brown dinocysts.

5.4.2. Miospores

Miospores are low in abundance and diversity but do contain rare angiosperm pollen in addition to pteridophytes and bisaccate pollen. This could hint toward the nearby presence of a hinterland with slightly more developed soils compared to what was inferred from the pteridophyte-

Table T9. Distribution of siliceous microfossils, Site U1580. B = barren, Tr = trace, R = rare. **Download table in CSV format.**

Sample ID	Top depth CSF-A (m)	Bottom depth CSF-A (m)	Diatom group abundance	Silicoflagellates group abundance	Radiolarians group abundance	Comment
392-U1580A-1R-CC-PAL(15-20)-DIAT	6.77	6.82	B	B	R	Trace radiolarian fragments with poor preservation
392-U1580A-3R-CC-PAL(12-17)-DIAT	23.60	23.65	B	B	B	Trace pyritized radiolarian fragments
392-U1580A-5R-CC-PAL(17-22)-DIAT	45.49	45.54	B	B	B	Mineral grains and clays
392-U1580A-7R-CC-PAL(6-11)-DIAT	66.04	66.09	B	B	B	Trace radiolarian fragments with some organic matter and minerals/clays
392-U1580A-9R-CC-PAL(20-25)-DIAT	87.57	87.62	B	B	B	
392-U1580A-11R-CC-PAL(18-23)-DIAT	97.18	97.23	B	B	B	
392-U1580A-14R-CC-PAL(5-10)-DIAT	129.27	129.32	B	B	B	
392-U1580A-16R-CC-PAL(16-21)-DIAT	147.82	147.87	B	B	B	
392-U1580A-18R-CC-PAL(21-26)-DIAT	173.14	173.19	B	B	B	Trace radiolarian fragments
392-U1580A-20R-CC-PAL(21-26)-DIAT	187.76	187.81	B	B	B	Trace radiolarian fragments
392-U1580A-22R-CC-PAL(15-20)-DIAT	212.99	213.04	B	B	B	
392-U1580A-24R-CC-PAL(19-24)-DIAT	227.70	227.75	Tr	B	B	Pyritized diatom fragments trace
392-U1580A-26R-CC-PAL(15-20)-DIAT	245.96	246.01	B	B	B	
392-U1580A-28R-CC-PAL(18-23)-DIAT	267.74	267.79	B	B	B	
392-U1580A-29R-CC-PAL(0-5)-DIAT	280.29	280.34	B	B	B	
392-U1580A-34R-CC-PAL(23-28)-DIAT	330.12	330.17	B	B	B	

Table T10. Distribution of palynofacies and palynomorphs, Site U1580. **Download table in CSV format.**

dominated miospore assemblages at Site U1579 (see **Micropaleontology** in the Site U1579 chapter [Bohaty et al., 2023]). However, because miospores are sparse at Site U1580, this is a speculative interpretation.

5.4.3. Paleoenvironments

The near-absence of macerals in the samples from Cores 392-U1580A-1R through 33R (6.77–311.24 m CSF-A) hints at well-ventilated bottom waters, allowing for thorough oxidation of organic matter. In turn, the presence of palynofacies in the samples from Cores 34R–42R (322.74–402.59 m CSF-A) suggests that exposure of sediments to oxygen was insufficient to remineralize all organic matter, at least in specific intervals of the sedimentary record. Dinocyst assemblages are typical of mid–continental shelf environments, although this might reflect the paleoenvironmental signal further upslope rather than the local environment, if the sediments were transported. The color variation of the dinocysts is reflective of the degree of maturation of the organic matter—the darker the macerals, the higher the maturity. In this case, we interpret the maturity to have originated from the intrusion of basaltic sills (see **Igneous petrology**), which provided heat

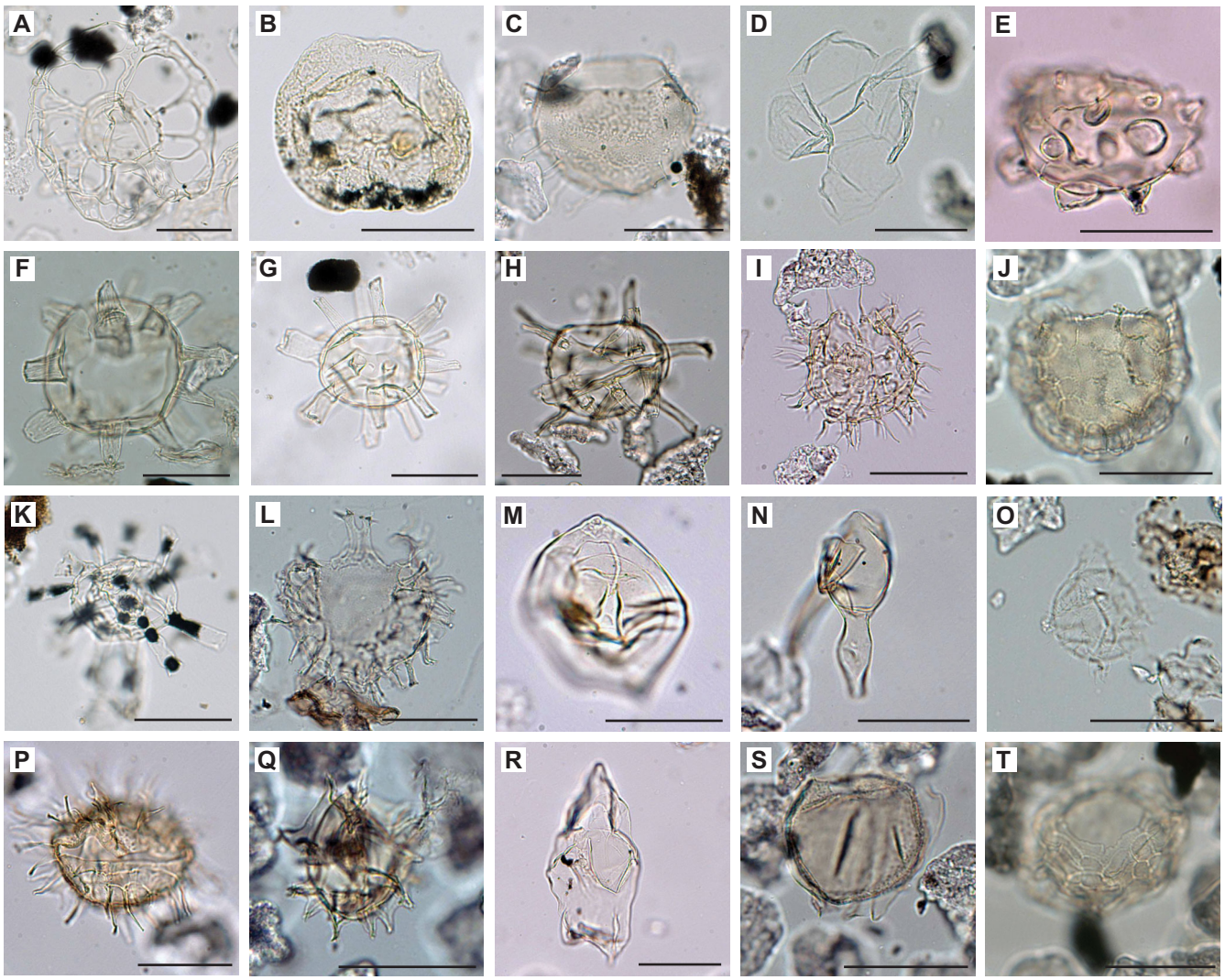

Figure F22. Selected dinocyst species from Hole U1580A. Scale bar = 50 µm. A. *Balteocysta perforata* (38R-6, 66–67 cm). B. *Canningia reticulata* (40R-3, 21–24 cm). C. *Circulodinium distinctum* (38R-CC). D. *Codoniella campanulata* (34R-2, 133–134 cm). E–H. Continuum between *Conosphaeridium abbreviatum* and *Conosphaeridium striatoconus*; (E) 40R-3, 21–24 cm; (F, H) 34R-2, 133–134 cm; (G) 38R-6, 66–67 cm. I. *Coronifera oceanica* (34R-2, 133–134 cm). J. *Cyclonephelium filoreticulatum* (36R-4, 19–20 cm). K. *Florentinia deanei* (40R-3, 21–24 cm). L. *Heterosphaeridium spinaconjunctum* (34R-2, 133–134 cm). M. *Isabelidinium glabrum* (38R-6, 66–67 cm). N. *Odontochitina costata* (38R-CC). O. *Palaeohystrichophora infusorioides* (34R-2, 133–134 cm). P. *Pervosphaeridium truncatum* (40R-3, 21–24 cm). Q. *Pterodinium cingulatum* (34R-2, 133–134 cm). R. *Satyrodinium haumuriense* (34R-2, 133–134 cm). S. *Senoniasphaera rotundata* (34R-2, 133–134 cm). T. *Valensiella reticulata* (36R-4, 19–20 cm).

to the surrounding sediments. Postcruise comparison of age constraints from the sills and sediments will allow testing of this hypothesis. The only sample that shows strong maturity of the macerals that is located well above the basaltic units is Sample 35R-CC, 25–30 cm (339.38 m CSF-A). Indeed, underlying and overlying samples (36R-4, 19–20 cm [344.10 m CSF-A], and 35R-1, 128–130 cm [331.08 m CSF-A], respectively) have translucent dinocysts with no signs of maturity.

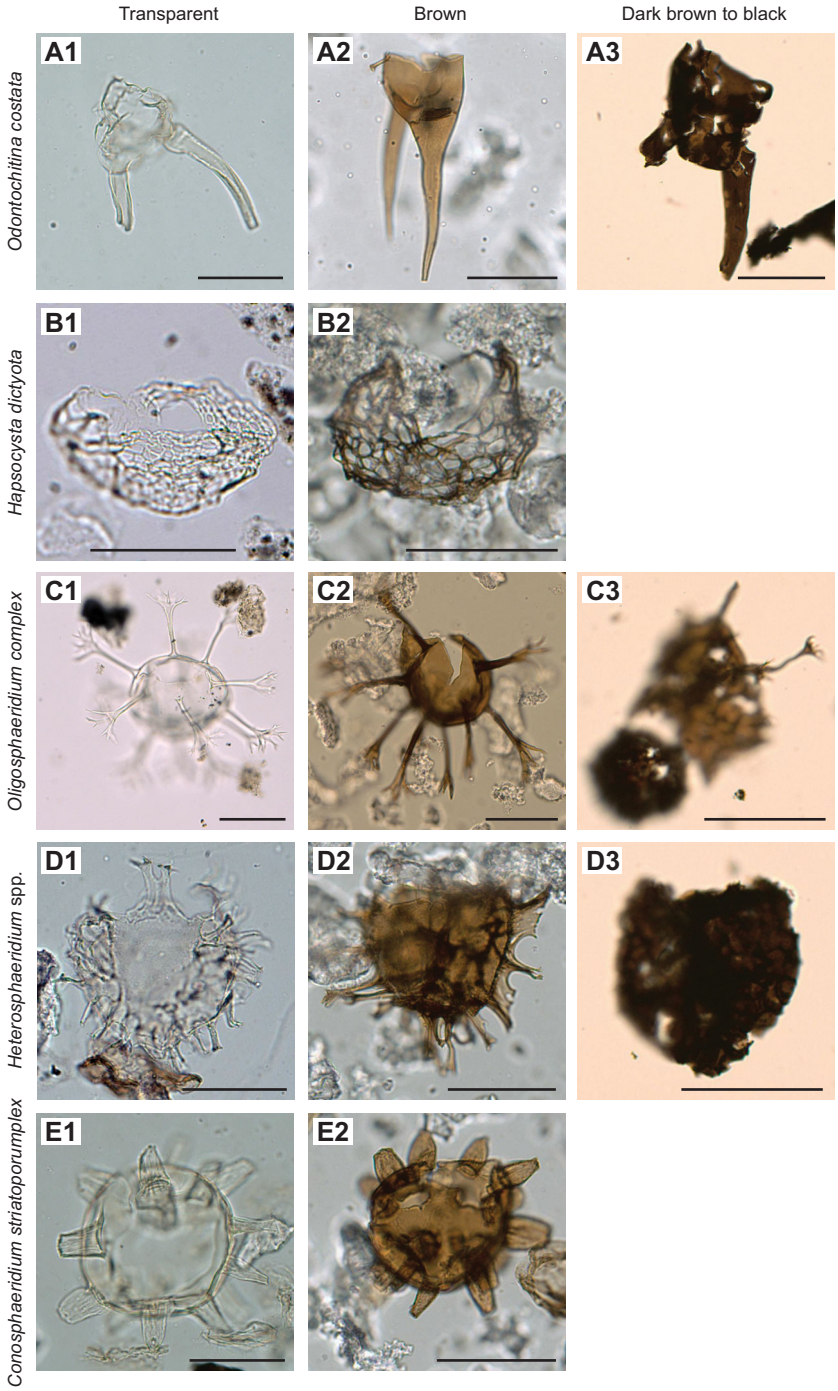

Figure F23. Color variation of specimens of *Odontochitina costata*, *Hapsocysta dictyota*, *Oligosphaeridium complex*, *Heterosphaeridium* spp., and *Conosphaeridium striatoconus* from Hole U1580A. Scale bar = 50 µm. Transparent (A1–E1), brown with rust colorations (A2–E2), and dark brown to black (A3, C3, D3). A (1) 34R-2, 133–134 cm (322.74 m CSF-A); (2) 35R-CC (339.38 m CSF-A); (3) 60R-1, 51–53 cm (481.11 m CSF-A). B (1) 38R-6, 66–67 cm (365.7 m CSF-A); (2) 40R-3, 21–24 cm (381.33 m CSF-A). C (1) 40R-3, 21–24 cm; (2) 35R-CC (339.38 m CSF-A); (3) 60R-1, 51–53 cm (481.11 m CSF-A). D (1) 4R-2, 133–134 cm (322.74 m CSF-A); (2) 35R-CC (339.38 m CSF-A); (3) 60R-1, 51–53 cm (481.11 m CSF-A). E (1) 34R-2, 133–134 cm (322.74 m CSF-A); (2) 35R-CC, 25–30 cm (339.38 m CSF-A).

This precludes the underlying sill as a cause for the maturation of the organic matter in this sample. Therefore, we interpret this as a signal that the dinocysts in this sample may have been transported from an upslope setting adjacent to a sill. It is interesting to note though that the dinocyst assemblage in this sample is of a contemporaneous stratigraphic age to the overlying and underlying sediment and therefore is not out of context within the in situ stratigraphy.

6. Paleomagnetism

Paleomagnetic measurements were performed on all archive-half sections from Holes U1580A and U1580B (Cores 392-U1580A-1R through 68R [0.0–528.58 m CSF-A] and 392-U1580B-2R through 5R [40.0–74.14 m CSF-A]) and on 68 discrete samples from Cores 392-U1580A-3R through 68R (21.7–525.14 m CSF-A) (Figures **F24**, **F25**). No discrete samples were collected for Hole U1580B because it recovered an interval already sampled in Hole U1580A. The primary purpose of paleomagnetic measurements was to determine magnetic polarity stratigraphy. Additional rock magnetic experiments were performed to further inform on the reliability of magnetic signals, magnetic fabric, and environmental and postdepositional processes, including anisotropy of magnetic susceptibility (AMS) and isothermal remanent magnetization (IRM) acquisition experiments.

Demagnetization experiments and rock magnetic analyses were performed to constrain magnetic polarity and the magnetic mineralogy of the sedimentary and igneous units recovered at Site U1580. Paleomagnetic results indicate that the units sampled at Site U1580 are reliable recorders of magnetic field direction. Magnetic polarity was determined from 61 of the 68 cores measured

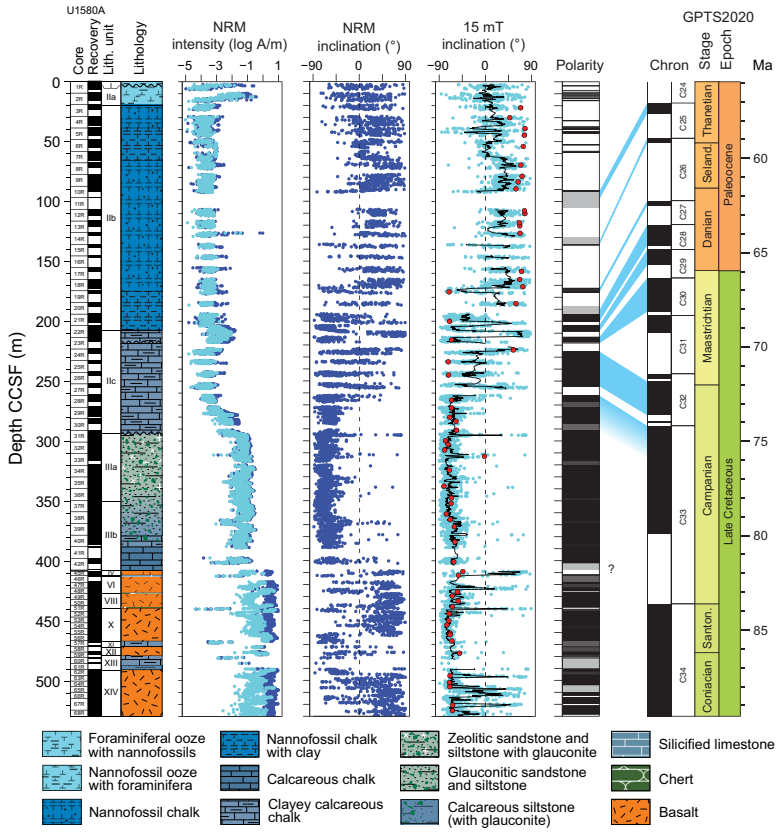

Figure F24. Magnetostratigraphic results, Hole U1580A. Dark blue dots = NRM intensity and inclination before AF demagnetization. Cyan dots = NRM intensity and inclination after 15 mT AF cleaning of archive halves. Black line in inclination column = 15 point moving average, red dots = discrete samples. The magnetic polarity plot is generated from the moving average: negative (up-pointing) inclination indicates deposition during a normal geomagnetic polarity field (black bands). Gray bands = intervals without paleomagnetic measurement (e.g., core gaps) or intervals where polarity could not be confidently constrained. Preliminary correlation with the GPTS of Ogg (2020) (GPTS2020) is shown (blue bands).

from Hole U1580A and all 4 cores measured from Hole U1580B. A total of 15 magnetic reversals (m1–m15) were identified, and normal and reversed polarity intervals were correlated to chrons in the geomagnetic polarity timescale (GPTS) from Geologic Time Scale 2020 (GTS2020; Ogg, 2020; Gradstein et al., 2020) (Figure **F31**; Table **T11**). These include Chrons C25n through C33n and Chron C34n. Rock magnetic results indicate that the dominant magnetic mineralogy is a combination of both ferrimagnetic and antiferromagnetic minerals, likely magnetite and hematite. Both ferrimagnetic and antiferromagnetic minerals occur in sedimentary Lithostratigraphic Unit I through Lithostratigraphic Subunit IIc (~0–300 m CSF-A) before transitioning to dominantly ferrimagnetic minerals in Lithostratigraphic Units III–XIV (~300–530 m CSF-A). AMS measurements indicate that sedimentary Lithostratigraphic Units I–III possess a typical oblate sedimentary fabric and that the basalts lack strong magnetic fabrics.

6.1. Discrete samples

Discrete sediment and igneous rock samples were analyzed from Cores 392-U1580A-3R through 68R (~19.4–528.58 m CSF-A). Two cores that span the Paleocene/Eocene (Core 7R) and K/Pg boundaries (Core 22R) were not sampled for discrete measurements. Additionally, cores with lim-

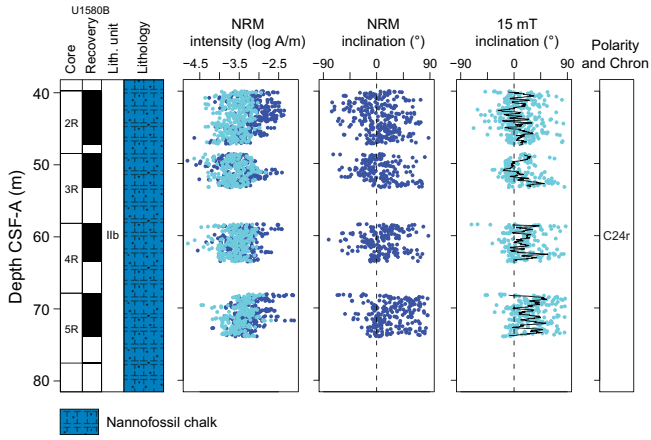

Figure F25. Magnetostratigraphic results, Hole U1580B. Dark blue dots = NRM intensity before AF demagnetization. Cyan dots = NRM intensity and inclination after 15 mT AF cleaning of the archive halves. Black line in inclination column = 10 point moving average. Cores 2R–5R deliberately targeted the Paleocene/Eocene boundary, which lies in the ~3 My long Chron C24r, and we therefore observe no magnetic reversals.

Table T11. Geomagnetic polarity tie points, Site U1580. Datum numbers correspond to those shown in Figure F31. **Download table in CSV format.**

Datum number	Top core, section, interval (cm)	Top depth CSF-A (m)	Bottom core, section, interval (cm)	Bottom depth CSF-A (m)	Midpoint depth CSF-A (m)	Chron boundary	Age (Ma)
	392-U1580A-		392-U1580A-				
m1	10R-3, 50	90.47	10R-3, 60	90.57	90.52	C24r/C25n	57.101
m2	10R-4, 55	91.82	12R-1, 0	106.70	99.26	C25n/C25r	57.656
m3	14R-3, 80	129.13	15R-1, 5	135.85	132.49	C25r/C26n	58.959
m4	15R-1, 65	136.45	15R-1, 80	136.60	136.53	C26n/C26r	59.237
m5	18R-6, 45	172.02	18R-6, 85	172.42	172.22	C26r/C27n	62.278
m6	19R-2, 15	175.98	19R-2, 20	176.03	176.01	C27n/C27r	62.53
m7	20R-2, 135	186.80	21R-1, 0	194.00	190.40	C27r/C28n	63.537
m8	21R-4, 150	199.87	21R-5, 55	200.43	200.15	C28n/C28r	64.645
m9	21R-6, 70	202.03	22R-1, 0	203.70	202.87	C28r/C29n	64.862
m10	22R-4, 45	208.35	22R-4, 48	208.38	208.36	C29n/C29r	65.7
m11	22R-7, 83	212.84	23R-1, 0	213.40	213.12	C29r/C30n	66.38
m12	23R-3, 120	217.28	23R-3, 133	217.41	217.34	C30n/C30r	68.178
m13	24R-2, 93	225.07	24R-3, 5	225.49	225.28	C32n.1r/C32n.2n	71.851
m14	27R-2, 60	254.29	27R-2, 133	255.02	254.65	C32n.2n/C32r.1r	73.651
m15	27R-3, 78	255.95	28R-1, 18	262.08	259.01	C32r.2r/C33n	74.201

ited recovery (Cores 11R, 41R, 43R–44R, 47R, 58R, and 60R–62R) were not sampled. Alternating field (AF) demagnetization experiments were performed on all discrete samples. AF steps were applied starting at 5 mT. Steps were progressively increased until either the samples lost 90% of their natural remanent magnetization (NRM) or to a maximum applied field of 120 mT. This procedure was sufficient to reveal characteristic remanent magnetization (ChRM) components for 60 of the 68 discrete samples. We note, however, that many of the sediment samples did not reach complete demagnetization using this procedure. In addition to demagnetization experiments, samples from sedimentary Lithostratigraphic Units I–III were also analyzed for AMS and IRM acquisition. Igneous samples were analyzed for AMS but were not subjected to IRM acquisition experiments to preserve their natural magnetization for postcruise analyses, which will enhance the understanding of their magnetic recording properties.

MS measurements (Figure **F26D**), normalized to volume, are consistent with measurements of whole cores. AMS experiments show that samples from sedimentary Lithostratigraphic Units I–III possess a typical oblate sedimentary fabric (k1 ≈ k2 > k3, where k_i are the axes of the AMS tensor), and the minor AMS axes (k3) are oriented parallel to the (*z*-)axis of the cores (Figure **F27A**). These results are confirmed by bootstrap analysis, which yields statistically overlapping k1 and k2 eigenvalues of the AMS tensor and a distinct minor eigenvalue (Figure **F27B, F27C**) (Constable and Tauxe, 1990). The anisotropy degree (P') and shape parameter (T) defined by Jelinek (1981) (see **Paleomagnetism** in the Expedition 392 methods chapter [Uenzelmann-Neben et al., 2023a]) were measured, and sedimentary samples generally have low P' (<1.3) and predominant oblate shapes (Figure **F27D**). P' does not show a particular trend downcore, but T assumes constant oblate values from ~250 to ~400 m CSF-A, which is likely the consequence of some degree of compaction. AMS data from the 18 discrete igneous samples show very low anisotropy degree values (average = 1.03), indicating the absence of significant fabrics (Figure **F27D**).

From IRM acquisition experiments, we calculated hard IRM (HIRM), saturation IRM (SIRM), and *S*-ratios (see **Paleomagnetism** in the Expedition 392 methods chapter [Uenzelmann-Neben et al., 2023a]) versus depth below seafloor (Figure **F26**). The HIRM is a measure of the contribution of high-coercivity minerals (e.g., hematite) to the total SIRM. The *S*-ratio is a measure of the relative amounts of low-coercivity (soft) versus high-coercivity (hard) magnetic minerals and provides an estimate of the relative contribution of ferrimagnets (e.g., magnetite) versus antiferromagnets

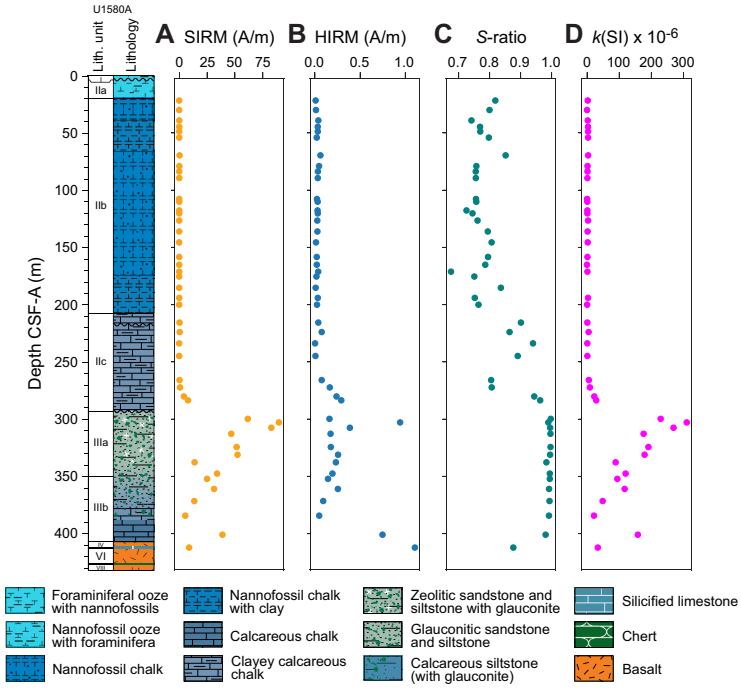

Figure F26. (A) SIRM, (B) HIRM, (C) *S*-ratio, and (D) MS (*k*), Hole U1580A.

(e.g., hematite) to the overall magnetic signal. Values of ~1 correspond to a dominance of ferrimagnetic minerals, and values <1 correspond to a dominance of antiferromagnetic minerals. In Hole U1580A, *S*-ratios indicate the presence of high-coercivity magnetic minerals (likely hematite) in most of the sedimentary units analyzed (Lithostratigraphic Units I–III, V, and XI) with a gradual increase downcore to Lithostratigraphic Subunit IIIa (~300 m CSF-A), where low-coercivity (ferrimagnetic) minerals become dominant. Below ~300 m CSF-A from Lithostratigraphic Subunit IIIa to Lithostratigraphic Unit V, the transition to ferrimagnetic dominance is accompanied by an increase in SIRM, HIRM, and bulk susceptibility values. This transition indicates a fundamental difference in magnetic mineralogy in these units compared to the sedimentary units above (Lithostratigraphic Unit I through Lithostratigraphic Subunit IIIa above 300 m CSF-A). NRM demagnetization results suggest that (titano)magnetite is one of the dominant low-coercivity minerals in these units and the primary carrier of magnetic remanence.

Demagnetization experiments on discrete samples yielded 60 ChRM directions from the 68 samples analyzed. The quality of the demagnetization data increases downcore, where the 14 ChRM directions between Cores 392-U1580A-2R and 13R were estimated using Fisher statistics (Fisher, 1953) and all others below Core 13R were determined using principal component analysis (PCA) (Kirschvink, 1980) using PuffinPlot software (Lurcock and Wilson, 2012) (Figure **F28A–F28D**). The majority of the sedimentary samples in Lithostratigraphic Subunits IIa–IIc were not completely demagnetized by peak AF fields of 120 mT, which is indicative of the presence of both low-coercivity minerals (which were demagnetized) and high-coercivity minerals (which were not demagnetized). These results are consistent with measured *S*-ratios for these samples. The igneous units (Lithostratigraphic Units IV, VI, VIII, X, XII, and XIV), on the other hand, were demag-

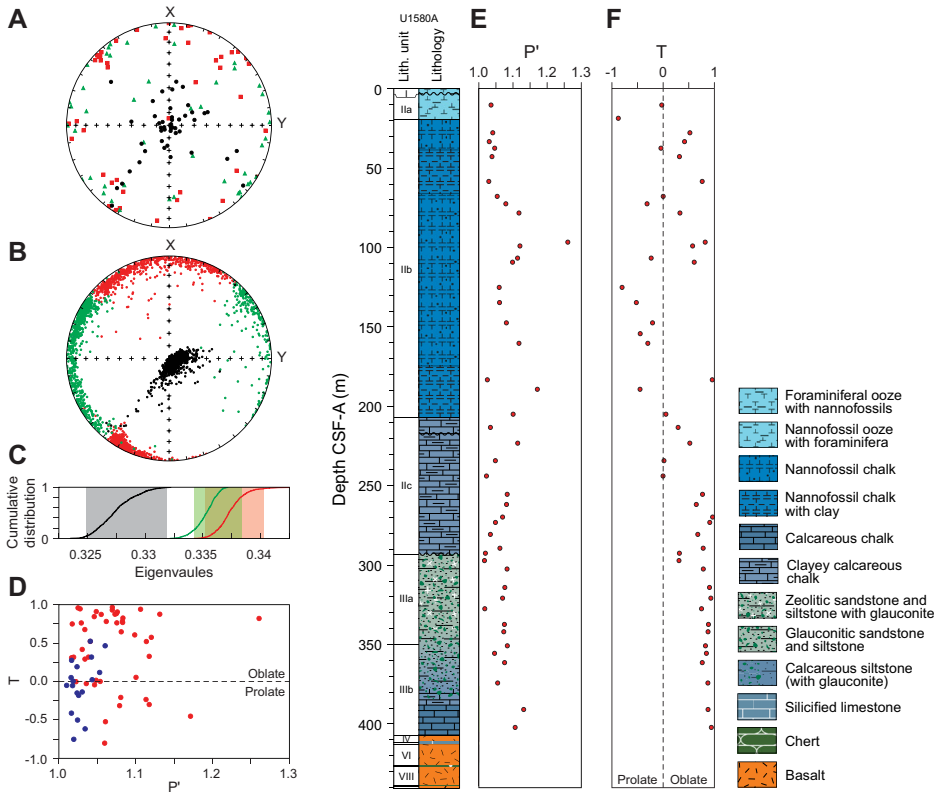

Figure F27. AMS analysis of discrete samples from Lithostratigraphic Units II and III, Hole U1580A. A. Equal-area projection from all samples. B. Average AMS tensors calculated from 1000 bootstrapped data sets. C. Cumulative distribution of the eigenvalues V_1, V_2, and V_3 associated to the 3 eigenvectors of the AMS tensor, calculated from the bootstrapped data set; V_3 is statistically distinct from overlapping V_1 and V_2, as expected in compacted (and undeformed) sediments. D. Diagram of P' and T; red dots = sediments, blue dots = igneous rocks. E, F. Stratigraphic variations of P' and T in the sedimentary units. All panels: the k1 ≥ k2 ≥ k3 axes or eigenvalues V_1, V_2, and V_3 of the AMS tensor are represented by red, green, and black symbols, respectively.

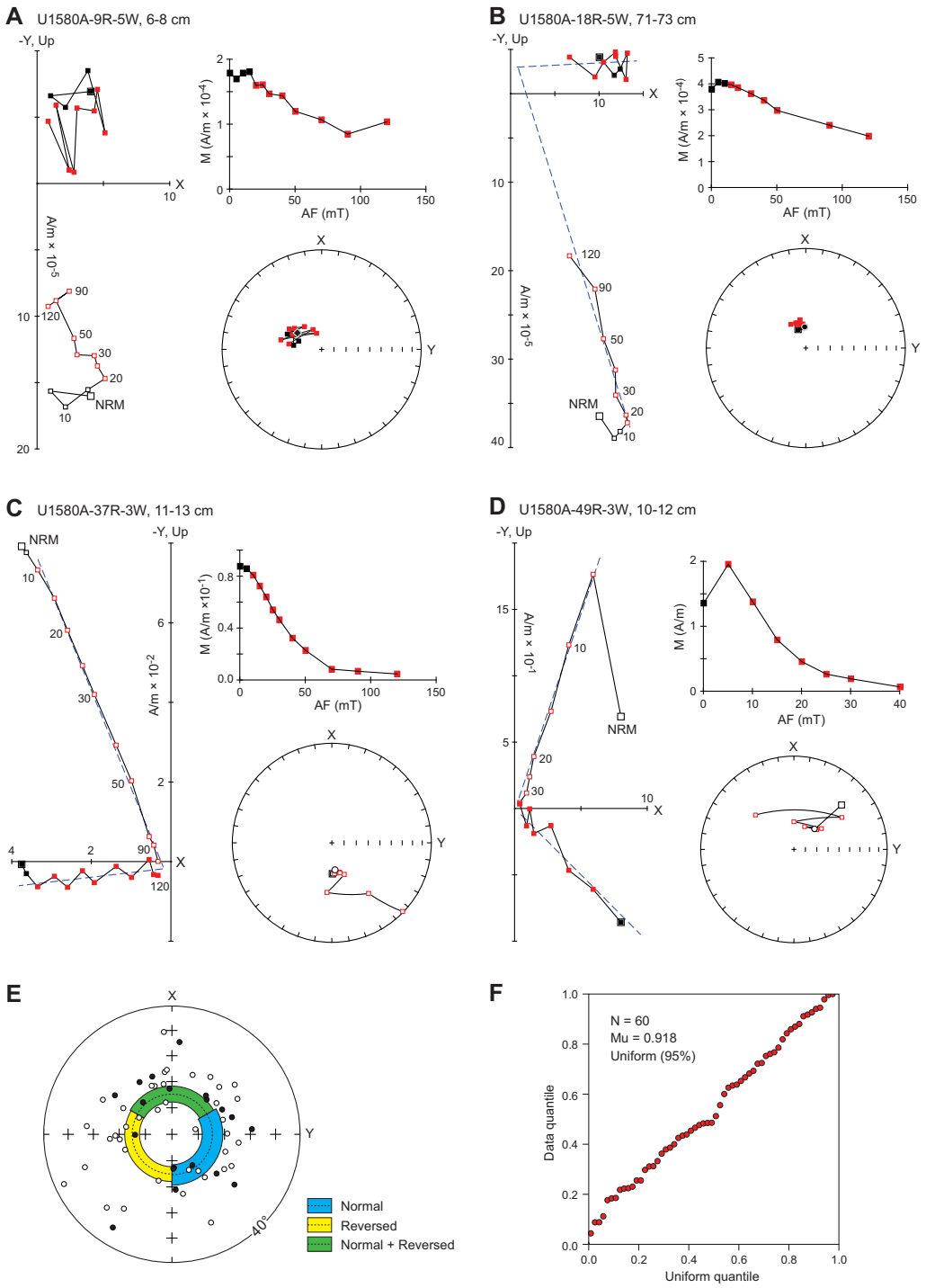

Figure F28. Discrete sample demagnetization analysis, Hole U1580A. A–C. Representative vector endpoint diagrams (left panels), equal area projections (round panels), and a graph showing natural magnetization (M) decay during demagnetization from Lithostratigraphic Units II–III (top right panels). D. Representative vector endpoint diagram (left panel), equal area projection (round panel), and a graph showing natural magnetization (M) decay during demagnetization from igneous rocks (Lithostratigraphic Unit VIII) (top right panel). Vector endpoint diagrams: white symbols = projections onto the vertical plane, black symbols = projections onto the horizontal plane, X and Y = axes of the working halves, and Up = vertical up-pointing (–Z-)axis of the core. Equal-area projections: open symbols = negative (up-pointing) directions, black symbols = positive (down-pointing) directions. All plots: red symbols = steps used to determine the characteristic remanent directions. E. Equal-area projection with all down-pointing (reversed; solid symbols) and up-pointing (normal; open symbols) paleomagnetic directions. Average inclination and 95% confidence boundaries are indicated in the inset (N + R = combined normal and reversed directions). F. Results from quantile-quantile analysis used to attest the uniformity of measured declinations; if $\mu > 1.207$, the null hypothesis of a uniform distribution of declination can be excluded at a 95% certainty (Fisher et al., 1987; Tauxe, 2010); the uniformly distributed declination values support the lack of pervasive drilling-induced magnetic overprints.

netized completely after a maximum applied AF step of ~40 mT, which suggests that the remanence is carried by Ti-rich magnetite or large pseudosingle domain-like to multidomain size particles (Dunlop and Özdemir, 1997). Directions are organized in two modes, either up-pointing (i.e., negative inclination), which indicates deposition during a normal geomagnetic field, or down-pointing (i.e., positive inclination), which indicates deposition during a reversed geomagnetic field. The inclination of the two modes is statistically antipodal (Figure **F28E**), indicating that the determined ChRM directions are unaffected by secondary magnetic overprints and that they are primary (Table **T12**). Average ChRM inclination measurements for discrete samples, calculated using the inclination-only protocol of McFadden and Reid (1982), are reported in Table **T12**. Furthermore, the declination of all directions is uniformly distributed around the vertical axis of the core (Figure **F28F**), which indicates the absence of pervasive overprinting induced by the drilling system.

6.2. Archive-half measurements

Downhole paleomagnetic measurements of NRM in Hole U1580A show a gentle increase in magnetization intensity in Cores 392-U1580A-1R through 28R (0.0–267.79 m CSF-A). This trend is briefly interrupted by a short magnetization increase across Cores 21R–23R, which brackets the K/Pg boundary, found in Core 22R (203.7–213.04 m CSF-A). The NRM intensity shows a marked two orders of magnitude increase in Cores 29R–31R (271.6–300.83 m CSF-A), near the transition between Lithostratigraphic Subunits IIc and IIIa. These higher NRM intensity values are sustained through Lithostratigraphic Subunits IIIa and IIIb (to 407.46 m CSF-A) to the transition to igneous Lithostratigraphic Unit IV, where the magnetization once again increases by two orders of magnitude (~408.6 m CSF-A). In Lithostratigraphic Units IV–XIV (~408.6–528.58 m CSF-A), magnetization intensity predominantly remains at these higher values except in intercalated sedimentary units (Lithostratigraphic Units V, VII, IX, XI, and XIII), where magnetization drops back to lower values.

All archive halves were subjected to low-field AF demagnetization up to maximum applied AF steps of either 15 or 20 mT. Demagnetization to these fields in the discrete samples was generally sufficient to remove secondary overprints and provides a good approximation for ChRM directions. Holes U1580A and U1580B were cored using the RCB system and were not oriented. Therefore, only inclination values after low-field demagnetization were used to determine polarity. To average out noise and aid polarity determination, a 15 point moving average was calculated from measured inclination data. In Hole U1580A, the paleomagnetic signal for Cores 1R–8R is noisy and difficult to interpret. From Core 9R (77.6 m CSF-A) downcore, consistent and reliable intervals of stable inclination values allow determination of polarity. In these intervals, both positive and negative inclination values are observed, indicating the presence of both normal and reversed polarity states. In Cores 28R–68R (261.9–528.58 m CSF-A), the inclination is predominantly negative, indicating that magnetization was acquired in these units during periods of normal magnetic polarity. This extended interval of normal polarity can be observed in Figure **F29**, which shows a clear peak in inclination at approximately −65°. All cores from the basalt units (Lithostratigraphic Units IV, VI, VIII, X, XII, and XIV) have large secondary steep and downward-pointing overprints, which is consistent with a drilling overprint. These secondary components were for the most part removed by 20 mT. Hole U1580B was drilled to recover a short sedimentary record across the Paleocene/Eocene boundary, which falls in the middle of a ~3 My reversed chron (C24r). Paleomagnetic results from Hole U1580B show that NRM intensity values are low (~1 × 10^{-4}) (Figure **F25**), but inclination values after AF demagnetization to 15 mT are predominantly positive, suggesting, as expected, that deposition occurred during a reversed chron.

6.2.1. Magnetostratigraphy

Throughout Hole U1580A, there is excellent agreement in inclination values between archive-half and discrete sample measurements. In Cores 9R through 28R (77.6–267.79 m CSF-A), 15 magnetostratigraphic reversals were identified (m1–m15; Figure **F31**; Table **T11**). In combination with biostratigraphic results, these reversals were successfully correlated to the GPTS (Ogg, 2020) and span from the top of Chron C25n to the top of Chron C33n (~57–74 Ma; Thanetian–Campanian) (Figure **F24**; Table **T11**). In Section 24R-1 (~223.55 m CSF-A), an observed distinct downcore

Table T12. Average paleomagnetic directions from discrete sample analysis, Site U1580. R+N = reversed and normal directions combined, *N* = number of averaged directions, Inc. = inclination, *k* = precision parameter of Fisher (1953), a95 = 95% confidence angle of Fisher (1953). Average angle and confidence parameters were estimated using the inclination-only approach of McFadden and Reid (1982). **Download table in CSV format.**

Mode	*N*	Inc. (°)	*k*	a95 (°)
Reversed	19	69	50	3.8
Normal	41	−68.6	19.5	5.3
R+N	60	68.8	24.4	4.1

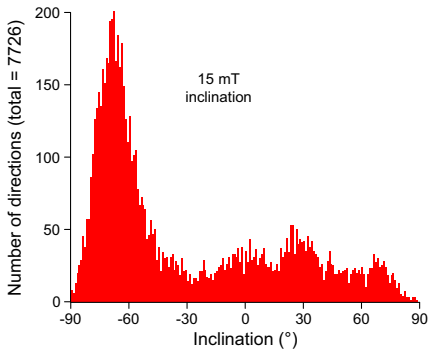

Figure F29. Histogram of all magnetic inclination data after 15 mT AF demagnetization, Hole U1580A.

shift in inclination from ~80° to ~70° is interpreted to indicate the presence of an unconformity, which is corroborated by biostratigraphic data from the same section (see **Micropaleontology**). In Cores 28R–68R (261.9–528.58 m CSF-A), paleomagnetic inclination values are negative, indicating acquisition during a normal geomagnetic polarity field. We interpret that this series of sediments and igneous rocks formed in the time encompassed by Chrons C33n and C34n. An unconformity at Core 31R (~291 m CSF-A), constrained by biostratigraphic data, straddles the ~75–85 Ma interval that encompasses Chron C33r and explains why it was not recorded (see **Chronostratigraphy**).

7. Stratigraphic correlation

At Site U1580, two holes were cored using the RCB system. Hole U1580A was drilled to 533.9 m drilling depth below seafloor (DSF) (bottom recovered depth = 528.58 m CSF-A), and Hole U1580B was drilled from 40.0 to 77.8 m DSF (bottom recovered depth = 74.14 m CSF-A). In the interval where the stratigraphy of the holes overlapped (Cores 392-U1580A-5R through 8R [38.80–72.82 m CSF-A] and 392-U1580B-2R through 5R [40.00–74.14 m CSF-A]), recovery was 68% in Hole U1580A and 63% in Hole U1580B.

7.1. Guidance for coring

A 40.0 m CSF-A starting depth for coring in Hole U1580B was recommended to recover the stratigraphic interval spanning the Paleocene/Eocene boundary encountered in Section 392-U1580A-7R-4, 61.5 cm (63.34 m CSF-A). Aligned core breaks between Holes U1580A and U1580B and Cores 392-U1580A-5R through 8R and 392-U1580B-2R through 5R, along with drilling disturbance, hampered the construction of a splice over the full interval cored in Hole U1580B, but features in individual cores may be correlated across holes.

7.2. Core composite depth below seafloor depth scale

In Hole U1580A, four sediment cores had more than 100% reported recovery, likely because of core expansion. Eight basalt cores had more than 100% recovery, as much as 139% for Core 392-U1580A-48R, causing apparent overlap on the CSF-A depth scale. Basalt cores may have incorpo-

rated drilled material that was not dislodged from the substrate during recovery of the previous core (i.e., the previously cut core was not broken off at the base of the drilled interval). To avoid the apparent overlaps, a CCSF depth scale was developed for Hole U1580A (Table **T13**), providing offsets for individual cores.

7.3. Correlation of core to wireline

Recognition of matching patterns in NGR records from cores and total spectral gamma ray (HSGR) data from wireline logging with the HNGS in Hole U1580A permitted translation of core depth scales from the CCSF (or CSF-A) scale to the wireline log matched depth below seafloor (WMSF) scale (Figure **F30**). This correlation places basalt cores with more than 100% recovery in a higher position than that recorded on the CSF-A scale, which is in line with the construction of the CCSF scale. For example, the top of Core 392-U1580A-48R at 422.37 m CSF-A is offset to 419.90 m CCSF (−2.47 m) for the construction of the CCSF scale and correlates to 419.68 m WMSF in the logging data.

Table T13. Affine table, Hole U1580A. **Download table in CSV format.**

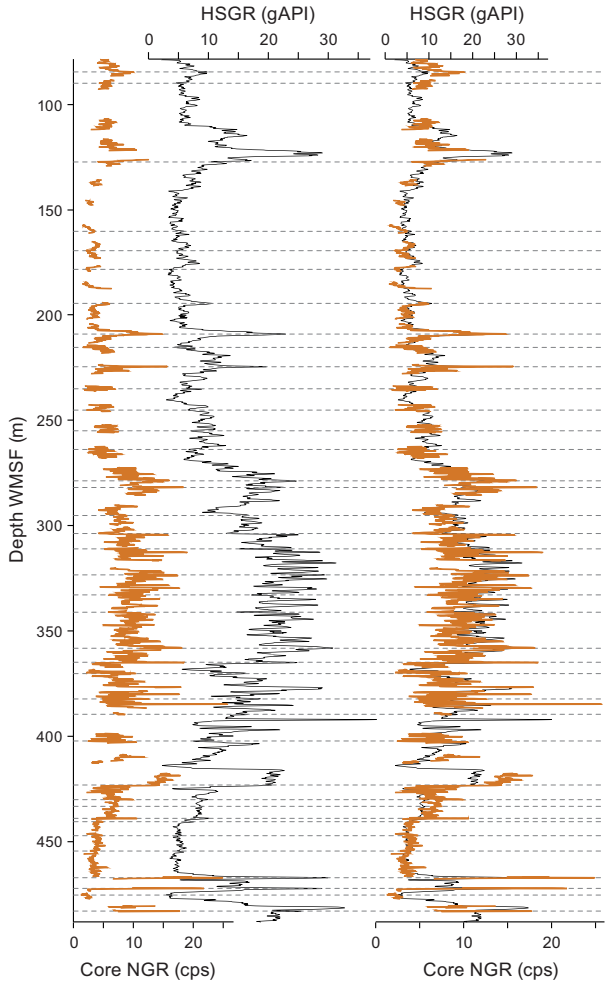

Figure F30. Correlation of NGR data measured on cores (orange) to HSGR data from downhole logging with the HNGS (black) on separate, equally scaled horizontal axes (left) and overlapping, differently scaled horizontal axes (right), Site U1580. Dashed gray lines = tie points to individual cores. cps = counts per second.

7.4. Summary

Compiled records of the cored intervals at Site U1580 demonstrate 66% recovery for the drilled interval spanning sediments of late Cenomanian to early Eocene age, as well as igneous rocks. A CCSF depth scale is constructed for Hole U1580A to enable visualization of results without overlap of recovered intervals between cores.

8. Chronostratigraphy

Calcareous nannofossils, planktonic and benthic foraminifera, dinocysts, and magnetostratigraphy provide age control for the uppermost Cenomanian–lower Eocene sedimentary sequence recovered at Site U1580 (see **Micropaleontology** and **Paleomagnetism**). Nannofossils provide biostratigraphic age constraints (Table **T5**) for the uppermost Cenomanian–lowermost Turonian sedimentary intervals (Lithostratigraphic Units XI and XIII; see **Lithostratigraphy**) found between basalt units. Dinocysts and nannofossils provide age constraints across the Coniacian–Santonian interval where paleomagnetic results (Table **T11**) show continuous normal polarity due to deposition during Superchron C34n. For the Campanian–lower Eocene sedimentary sequence, biostratigraphic datums guided the interpretation of magnetic polarity reversals, which are correlated to the GPTS (Ogg, 2020) (Table **T11**). Magnetic reversals are less well constrained with biostratigraphy in the Campanian–lower Maastrichtian interval and require a higher resolution study postcruise. Below, we describe ages and sedimentation rates of the sedimentary succession in stratigraphic order from oldest to youngest (Figure **F31**).

8.1. Cenomanian–Turonian (~94 Ma; 490.54–467.21 m CSF-A)

Sediments (Lithostratigraphic Units XI and XIII) intercalated between basalts in Cores 392-U1580A-62R and 56R are latest Cenomanian–earliest Turonian in age. The biohorizon tops of *H. chiastia* (n22 in Figure **F31** and Table **T5**) and *A. biramiculatus* (=*A. albianus*; n23, same figure) in samples from Core 60R (481.54–480.84 m CSF-A; 481.54–480.84 m CCSF) are of latest Cenomanian age (93.90 and 93.98 Ma, respectively), and the biohorizon base of *Q. gartneri* in Sample 57R-CC, 13–16 cm (467.21 m CSF-A; 468.84 m CCSF), is early Turonian in age (93.75 Ma; n21, same figure). Because these biohorizons are found in thin sedimentary successions between igneous units, we cannot infer sedimentation rates.

8.2. Coniacian–Santonian (86.1–85.2 Ma; 402.54–300.78 m CSF-A)

The presence of dinocyst *C. distinctum* (dc4 in Figure **F31** and Table **T5**) at the base of Lithostratigraphic Subunit IIIb (Sample 392-U1580A-42R-CC, 22–27 cm; 402.54 m CSF-A), indicates a maximum possible age of ~88 Ma for the lowermost sediments on top of the uppermost basalt unit (Lithostratigraphic Unit IV). The biohorizon bases of *M. staurophora* (n19, same figure) in Sample 42R-2A, 43 cm (399.63 m CSF-A), and *I. cristatum* (dc3, same figure) in Sample 40R-3, 21–24 cm (381.33 m CSF-A), may suggest low sedimentation rates in the lowermost part of Lithostratigraphic Subunit IIIb. However, these may not represent the true bases of these species because they directly overlie the basalt; therefore, we infer high, linear sedimentation rates of ~11 cm/ky for Lithostratigraphic Unit III.

Nannofossil and dinocyst datums indicate a late Coniacian–early Santonian age (86–85.2 Ma) for the top of Lithostratigraphic Subunit IIIa (349.98–293.51 m CSF-A), specifically from the biohorizon top of *B. perforata* (85 Ma; dc2 in Figure **F31**) in Sample 392-U1580A-36R-4, 19–20 cm (344.1 m CSF-A), as well as the biohorizon tops of *L. septenarius* (85.30 Ma; n18, same figure) in Sample 32R-6, 65 cm (308.61 m CSF-A), and *E. floralis* (84.00 Ma; n17, same figure) in Sample 31R-CC, 15–20 cm (300.78 m CSF-A). The top of Lithostratigraphic Unit III is bounded by an unconformity that is ~8 My in duration based on inferred linear sedimentation rates above in Lithostratigraphic Subunit IIc and below in Lithostratigraphic Unit III (Figure **F31**). Further high-resolution sampling for dinocysts and nannofossils will provide additional age control for this interval.

8.3. Campanian–Maastrichtian (77.9–66.04 Ma; 300.78 to ~209.1 m CSF-A)

Lithostratigraphic Subunit IIc is bounded by two hiatuses. The hiatus at the base of this subunit is identified between the top of Section 392-U1580A-31R-2 and the base of Section 31R-CC (292.49–300.83 m CSF-A). The base of this subunit must be older than the biohorizon top of *E. eximius* s.s. (75.85 Ma; n16 in Figure **F31** and Table **T5**), which is found in Sample 31R-2, 42 cm (292.91 m CSF-A). The absence of *M. furcatus* from this sample indicates that this subunit must be younger than 80.97 Ma. There are few biostratigraphic constraints in Lithostratigraphic Subunit IIc; however, the available biostratigraphic constraints at the top and base of the subunit allow assignment of three paleomagnetic reversals (m13, m14, and m15 in Figure **F31** and Table **T11**) to Chron C32, which provides good age control, and includes the Chron C33n/C32r.2r boundary between Cores 27R and 28R (~259 m CSF-A). Another hiatus is inferred near the top of Lithostratigraphic Subunit IIc based on an abrupt change in paleomagnetic inclination in Section 24R-1, 45 cm (223.55 m CSF-A) (see **Paleomagnetism**). In addition, the detection of the biohorizon top of *R. levis* (70.14 Ma; n14, same figure) immediately below the shift in inclination in Sample 24R-1, 80 cm (223.90 m CSF-A), would indicate a significant change in sedimentation rate compared to the overlying succession unless a hiatus is inferred. Between these hiatuses at ~223.55 and 292.49 m CSF-A, average sedimentation rates of 1.3 cm/ky are estimated for the late Campanian.

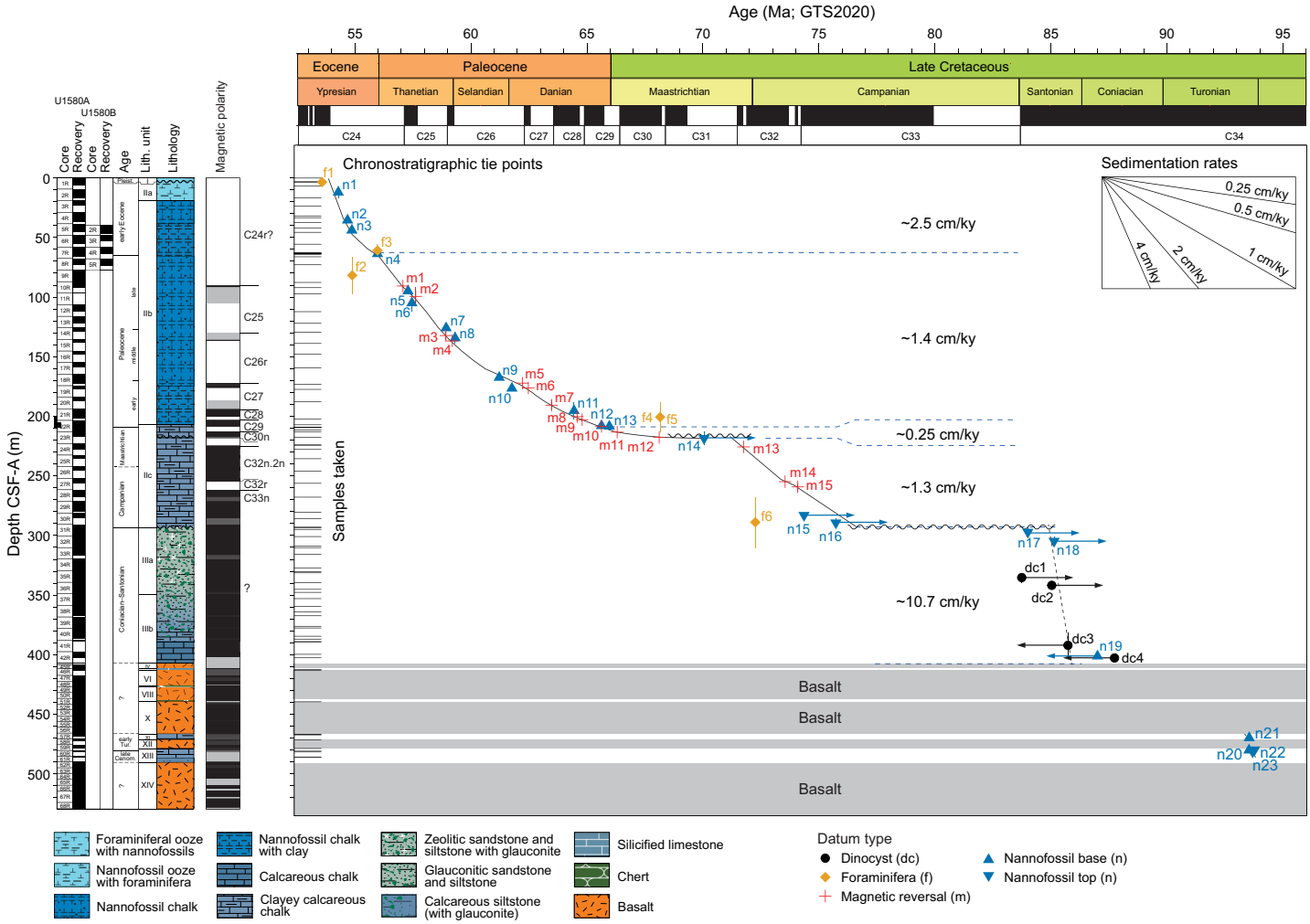

Figure F31. Age-depth model and average sedimentation rates, Site U1580. Numbers for bioevents correspond to those in Table T5. Numbers for magnetic reversals correspond to those in Table T11.

The inferred hiatus in Core 392-U1580A-24R (~224 m CSF-A) truncates the lower Maastrichtian succession. Its duration is at least 2 My based on the biohorizon top of *R. levis* (70.14 Ma; n14 in Figure **F31**) below the unconformity and the Chron C30r/C30n boundary (68.178 Ma; m12, same figure) above the unconformity in Core 23R. Nannofossil assemblages suggest that the K/Pg boundary is located between Samples 22R-4A, 135 cm (209.25 m CSF-A), and 22R-3A, 55 cm (207.07 m CSF-A) (see **Micropaleontology**). Correlation of sediment banding patterns of Core 22R with banding patterns over the K/Pg boundary interval in Core 392-U1579D-33R suggests that the K/Pg boundary may be marked by a color change (see **Lithostratigraphy**) in Section 392-U1580A-22R-4, ~120 cm (~209.1 m CSF-A); we therefore tentatively place the boundary at this position. This boundary defines the top of the Maastrichtian, and a low sedimentation rate (~0.25 cm/ky) is calculated for the Maastrichtian interval above the hiatus at ~224 m CSF-A.

8.4. Paleocene (66.04–56.0 Ma; ~209.1–63.32 m CSF-A)

The K/Pg boundary in Core 392-U1580A-22R (~209.1 m CSF-A) marks the base of the Paleocene succession. The Paleocene appears to be continuous at the resolution of 18 shipboard bio- and magnetostratigraphic (Chrons C29r through C24r) age tie points (Figure **F31**). The Paleocene/Eocene boundary is identified in interval 7R-4, 61.5 cm (63.34 m CSF-A), based on nannofossil biostratigraphy (see **Micropaleontology**), a distinct color change (see **Lithostratigraphy**), and the physical properties of the sediment (see **Physical properties**). Average sedimentation rates for this interval are 1.44 cm/ky and show a slight increasing trend upsection.

8.5. Early Eocene (56.0–53.6 Ma; 63.32–3.42 m CSF-A)

In Hole U1580A, the Paleocene/Eocene boundary is located in Section 392-U1580A-7R-4, 61.5 cm (63.335 m CSF-A). A second copy of this boundary was recovered in Core 392-U1580B-4R. The top of Hole U1580A is dated to the Pleistocene based on nannofossil biostratigraphy, and it overlies Eocene sediment dated to ~53.6–54 Ma based on foraminiferal and nannofossil biostratigraphy. In the lower Eocene succession, seven biostratigraphic datums provide chronostratigraphic age constraints. Because of low magnetization intensity, no magnetic reversals were identified in this interval. The biostratigraphic datums suggest an average sedimentation rate of 2.5 cm/ky for the lower Eocene, which is higher than that calculated for the Paleocene.

9. Geochemistry

The geochemistry program at Site U1580 was designed to characterize the composition of bulk sediment and interstitial water (IW) and report on the presence and abundance of volatile hydrocarbons (HC) for routine safety monitoring. In addition, major elements and certain trace element data were also determined on selected igneous rock samples. A sedimentary sequence spanning the Pleistocene to Upper Cretaceous was recovered at Site U1580 (see **Lithostratigraphy** and **Chronostratigraphy**). Sediments were analyzed for carbon and nitrogen concentration in Hole U1580A through Section 61R-1 (485.99 m CSF-A). IW samples were analyzed through Section 37R-5 (356.16 m CSF-A), below which pore water was not extractable.

9.1. Headspace hydrocarbon gases

In total, 51 headspace samples were taken and analyzed for routine safety monitoring (Table **T14**). The samples typically were taken from the top of the deepest section above the core catcher in each core with the exception of lithified cores, where sediment was taken from the section breaks of the core for convenience. Methane above the detection limit was not found in any samples. Propene (17.4 ppmv), iso-pentane (5.8 ppmv), and iso-hexane (3.9 ppmv) were detected in Sample 392-U1580A-9R-7, 0–5 cm (86.63 m CSF-A).

Table T14. Hydrocarbon gas concentrations, Site U1580. **Download table in CSV format.**

9.2. Interstitial water geochemistry

Samples for IW were collected downcore until minimal water was retrieved in a sample. No pore fluid samples were taken between 205.02 and 295.25 m CSF-A (Cores 392-U1580A-23R through 30R) because the porosity drops in this depth range, which did not allow for pore fluid extraction, and no pore fluid samples were collected below Core 37R (356.16 m CSF-A) because the sediment became too consolidated (see **Lithostratigraphy**).

Note that although Table **T15** presents both ICP-AES data and ion chromatography data for many of the major elements, we focus on the ion chromatography results for sulfate, chloride, and sodium and the ICP-AES data for the balance of the major cations because the ICP-AES data appeared to yield more consistent results for these major cations during this expedition. All data are however presented for completeness. When discussing specific depths of samples, this section is referencing the Top Depth CSF-A (m) value.

Alkalinity decreases from 3.0 mM in the shallowest sample (392-U1580A-1R-3, 145–150 cm; 3.75 m CSF-A) to 0.3 mM in Sample 33R-1, 87–97 cm (311.27 m CSF-A) (Figure **F32**; Table **T15**). Alkalinity is generally constant but distinctly low (0.3–0.5 mM) below ~295 m CSF-A. pH is relatively constant at 7.4 to <7.7 throughout the upper 185 m CSF-A and 7.7–8.3 below 295 m CSF-A (Figure **F32**; Table **T15**). Of the major anions, sulfate decreases at Site U1580 from 28.3 mM at 3.75 m CSF-A to 21.9 mM at ~356 m CSF-A (Figure **F33**). Chloride increases downhole from 573

Table T15. IW composition, Site U1580. **Download table in CSV format.**

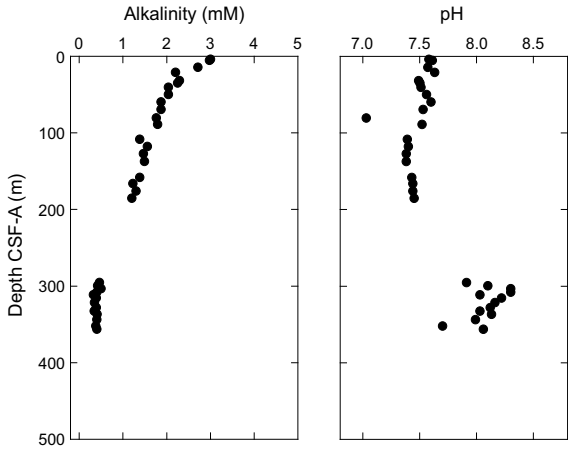

Figure F32. Alkalinity and pH, Site U1580.

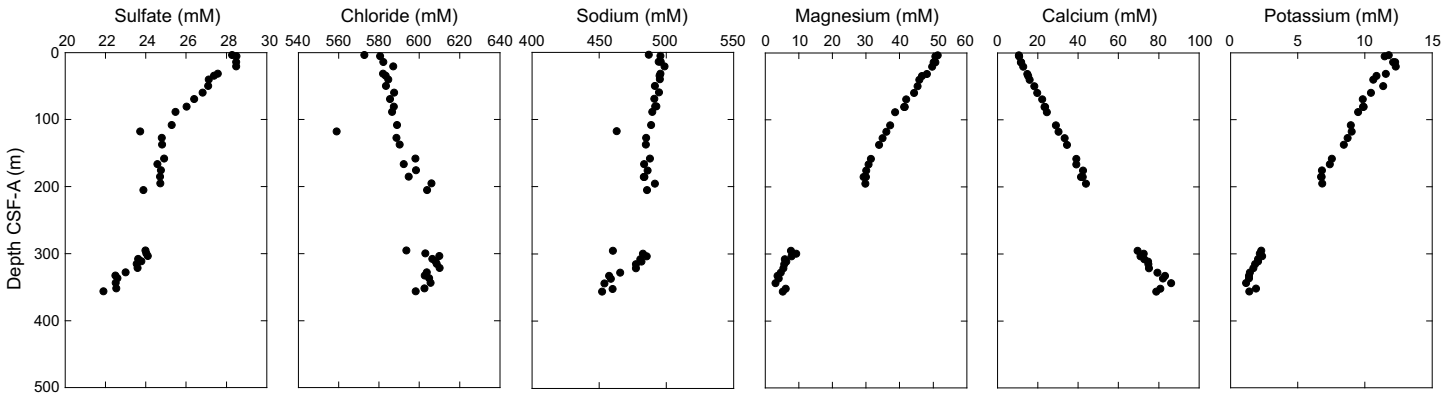

Figure F33. IW sulfate, chloride, sodium, magnesium, calcium, and potassium, Site U1580.

mM to >600 mM below ~300 m CSF-A (Figure **F33**). The major cation sodium shows a slight decline over its seawater value (481 mM) throughout the site to ~328 m CSF-A, below which values decline to 452 mM at 356.16 m CSF-A (Figure **F33**). Magnesium declines from 51.1 mM at 3.75 m CSF-A to 3.0 mM at 343.81 m CSF-A, followed by a slight increase in concentration in the bottom two samples (Figure **F33**). Calcium (ICP-AES) inversely mirrors Mg and increases from ~10.7 mM at 3.75 m CSF-A to 86.0 mM at ~343 m CSF-A, below which values decline slightly to 80.7 and 78.7 mM for the bottom two pore fluid samples. Potassium declines throughout the site from 11.7 mM at 3.75 m CSF-A to 1.2 mM at 343.81 m CSF-A, below which concentrations elevate slightly, consistent with the Mg increase and the Ca decrease in the deepest two samples (Figure **F33**). Compared with Site U1579, dissolved Li concentrations are remarkably constant over the upper 195 m of the sediment column, increasing slightly from 24.6 µM at 3.75 m CSF-A to 29.2 µM at 195.4 m CSF-A (Figure **F34**). This small positive gradient is followed by a systematic decline in concentrations for interval 295.25–356.16 m CSF-A. Sr gradually increases from 91.8 µM at 3.75 m CSF-A to 308.1 µM at 195.4 m CSF-A. Between 299.61 and 356.16 m CSF-A, Sr declines slightly from ~315 to 285 µM. Boron concentrations decline slightly from 448 µM at 3.75 m CSF-A to 402 µM at 195.4 m CSF-A. Boron values between 295.6 and 356.2 m CSF-A show a scattered distribution but decline from ~400 µM to 356 µM. Iron shows a gradual increase from below detection to ~20 µM at 69.3 m CSF-A, followed by a decline to values below detection at 195.4 m CSF-A (Figure **F34**).

9.3. Bulk sediment geochemistry

In total, 83 sediment samples were obtained for bulk carbon and nitrogen analyses at Site U1580. One or two samples were routinely taken from the working half sections and more frequently in some cores to capture specific intervals of lithologic variability. Total carbon and $CaCO_3$ range 0.0–14.5 and 0.0–97.2 wt% at Site U1580, respectively, which is consistent with the deposition of pelagic nannofossil oozes and chalks, zeolitic sand/siltstones, limestone, and claystone (see **Lithostratigraphy**) (Figure **F35**; Tables **T16**, **T17**). We observe more variability in $CaCO_3$ content between ~220 and 290 m CSF-A compared to the stable content above and generally lower but still variable concentrations in Lithostratigraphic Units III to XIII (excluding basalts) below ~290 m CSF-A. In this lower interval, inorganic carbon and carbonate decrease to averages of 1.5 and 12.8 wt%, respectively. As a note of caution for the interpretation of these inorganic carbon records, we emphasize that the main carbonate mineral phase is likely calcite for most parts of the nannofossil and foraminiferal ooze and chalk lithologies (Lithostratigraphic Units I and II; see **Lithostratigraphy** for smear slide data). However, in the green zeolitic siltstone-sandstone, limestone, and claystone below ~290 m CSF-A (Lithostratigraphic Units III, V, VII, XI, and XIII), the carbonate content may include other carbonate minerals, including siderite, dolomite, and possibly others (see **Lithostratigraphy**). Despite these uncertainties, it is worth noting that carbonate carbon persists to the bottom of the analyzed sedimentary section (~485 m CSF-A), with local increases to as

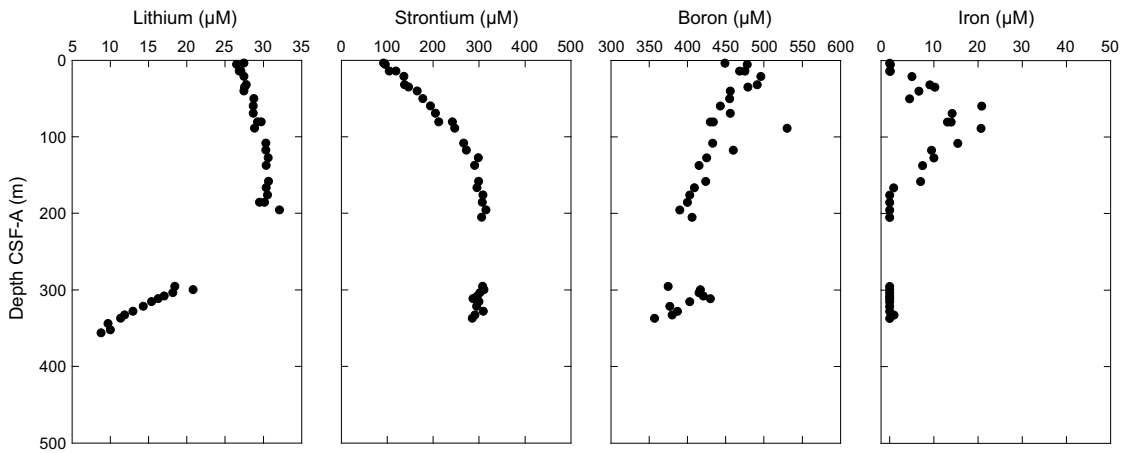

Figure F34. IW lithium, strontium, boron, and iron, Site U1580.

high as 62.5 wt%. We note six horizons between ~360 and ~465 m CSF-A (Cores 392-U1580A-38R through 57R) with intermediate to high carbonate content between ~40 and 60 wt%. Corresponding lithologies are diverse, covering siltstone, limestone, and dark, finely laminated claystone (see **Lithostratigraphy**).

Organic carbon contents are calculated as the difference between the total carbon (elemental analyzer measurement) and inorganic carbon (coulometer measurement) (Table **T17**). Values calculated below 0 were set to 0. The average total organic carbon (TOC) is 0.4 ± 1.2 wt% with minimum and maximum concentrations of 0 and 9.3 wt%, respectively. We note four samples with TOC content >1 wt% below ~315 m CSF-A, with two samples >5 wt% in the lowest part of the hole deeper than 410 m CSF-A. These samples are composed of calcareous siltstone (Sample 392-U1580A-46R-1, 39–40 cm; 412.19 m CSF-A) and black claystone (Sample 57R-1, 17.5–18.5 cm; 466.175 m CSF-A). The uncertainty in the organic carbon estimation (±0.27 wt%) is based on the average uncertainties in the carbonate carbon and total carbon measurements from repeat analysis of individual samples. Concentrations of organic carbon average ~0.4 wt% (we assume below detection limit concentrations = 0 for the purposes of this calculation) throughout the site, reflecting the prominent calcareous ooze, chalk, and limestone character of large parts of the sedimentary sequence that have low organic carbon abundances and supporting the overall very low methane concentrations. These results will be verified with shore-based analysis, using decalcified samples to determine organic carbon directly using an elemental analyzer.

Total nitrogen was measured but remains at or below the detection limit for most samples analyzed from Site U1580. Where quantified, concentrations remain below 0.1 wt%, except for Sample 392-U1580A-57R-1, 17.5–18.5 cm, at ~466 m CSF-A, where nitrogen increases to 0.3 wt%. The

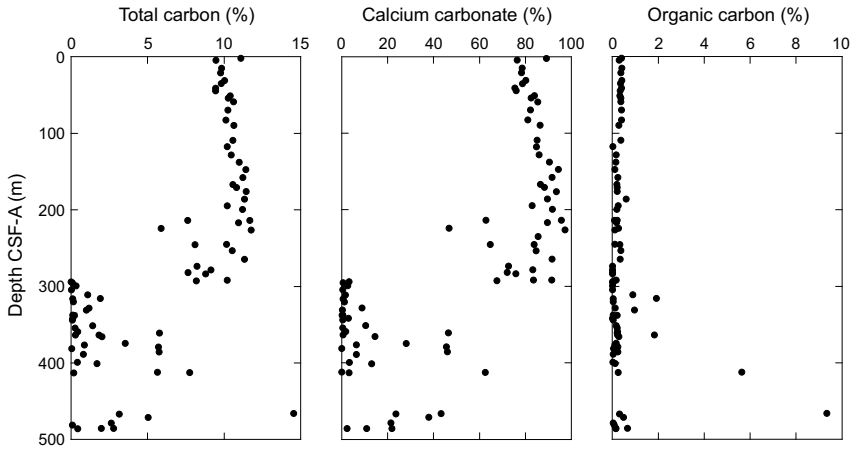

Figure F35. Total carbon, calcium carbonate, and organic carbon, Site U1580. Organic carbon is calculated as the difference between total and inorganic carbon.

Table T16. Bulk sediment geochemistry data statistics, Site U1580. STDV = standard deviation. **Download table in CSV format.**

Statistic measures	$CaCO_3$ (wt%)	Inorganic C (wt%)	Total C (wt%)	N (wt%)	Organic C (wt%)
Min:	0.03	0.00	0.00	0.00	0.00
Max:	97.17	11.66	14.53	0.26	9.34
Average:	49.09	5.89	6.08	0.01	0.44
STDV:	37.79	4.53	4.59	0.03	1.21

Table T17. Bulk sediment geochemistry data, Hole U1580A. **Download table in CSV format.**

low nitrogen values for the entire hole (except Sample 57R-1, 17.5–18.5 cm; 466.175 m CSF-A) suggest that inorganic nitrogen may be the primary component being analyzed. The data are presented in Table **T17** but are not discussed here further. The TOC/nitrogen (N) ratio of Sample 57R-1, 17.5–18.5 cm (466.175 m CSF-A), is 35.6, suggesting an admixture of terrestrial organic matter.

9.4. Organic matter source and thermal maturity analysis

Based on lithology and color (see **Lithostratigraphy**), initial assessment of palynology (see **Micropaleontology**), and calculated TOC content, we selected 10 samples from below ~290 m CSF-A (Cores 392-U1580A-31R through 61R) for source rock analyzer (SRA) measurement to identify their organic matter source (kerogen type) and level of thermal maturation.

Calculated TOC content based on S1, S2, and S4 yields vary between 0.3 and 8.5 wt% (Table **T18**). The data support the presence of residual carbon (captured as S4) in the kerogen fraction of the samples analyzed. HC yields (S1 and S2) are low, between 0.03 and 0.85 mg HC/g TOC for S1 and no detection (0) and 0.83 mg HC/g TOC for S2, except for Sample 392-U1580A-57R-1, 17.5–18.5 cm (~466 m CSF-A), which shows a much stronger HC response (1.1 and 7.9 mg HC/g TOC). CO_2 yields of S3 are low to moderate between 0.2 and 1.7 mg CO_2/g TOC for all samples. The overall low HC and CO_2 response during pyrolysis asks for caution when evaluating hydrogen index (HI), oxygen index (OI), and thermal maturity proxies (T_{max} and production index [PI]). The results from Sample 57R-1, 17.5–18.5 cm (466.175 CSF-A), stand out with a strong pyrolysis and oxidation signal that supports confident interpretation of both organic matter source and thermal maturity. The results from SRA analyses are illustrated in traditional HI – T_{max} and HI – OI diagrams (Figure **F36**). Low to very low HI (<100 mg HC/g TOC) and scattered OI with values as high as 300 mg CO_2/g TOC support the presence of nonreactive organic carbon of type IV kerogen in the lower part of Hole U1580A. The strong signal from Sample 57R-1, 17.5–18.5 cm (466.175 m CSF-A), hints toward a mixed type II/III kerogen source of marine and terrigenous origin. The elevated C/N ratio of 36.4 is consistent with this initial conclusion. A similar origin may apply to the other samples; however, their low HC response does not support further analyses. Thermal maturity is at peak to early post oil window maturity, confirmed at Sample 57R-1, 17.5–18.5 cm (466.175 m CSF-A), or higher (all other samples). T_{max} (454°–560°C) and PI indexes (0.12–1.0) are consistent. Overmature levels suggested for most samples must be taken with caution because of the low signal response.

Table T18. SRA data, Site U1580. **Download table in CSV format.**

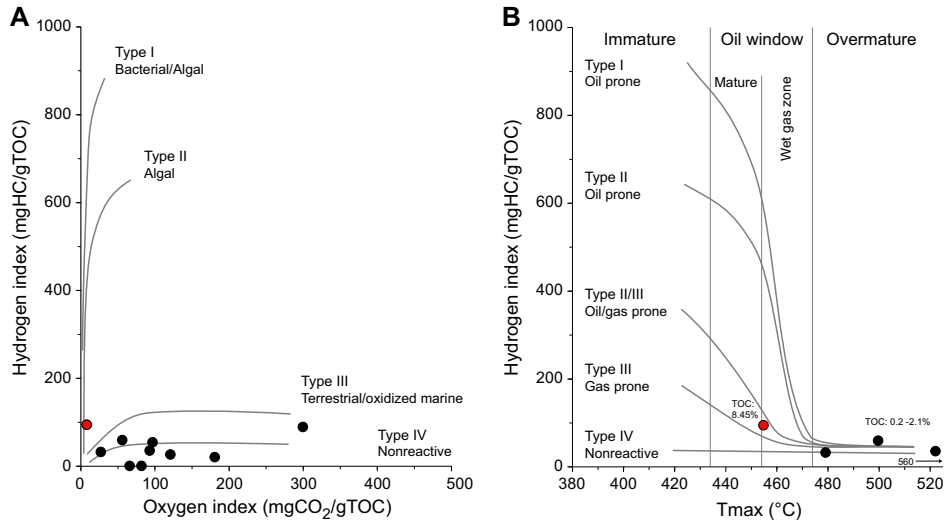

Figure F36. SRA results, Site U1580. (A) HI – OI and (B) HI – T_{max} plots. Red solid symbol = 392-U1580A-57R-1, 17.5–18.5 cm. SRA-derived TOC percentages are presented.

The SRA results support a mixed marine–terrestrial organic matter source and excess thermal maturation at much shallower depths than anticipated. This conclusion is supported by palynological observations of mixed terrestrial and marine palynomorphs and abundant dark colored palynomorphs of elevated thermal maturity in the lower part of the section (see **Micropaleontology**).

The combined geochemical and palynological observations in Hole U1580A provide strong evidence for localized thermal overprint most likely connected to the underlying and interbedded igneous units, tentatively interpreted as magmatic sill intrusions (See **Igneous petrology**).

9.5. Sediment and hard rock geochemistry

All sediment major element concentrations are calculated and discussed as element weight percentages, and all minor and trace elements are presented in parts per million (Figure **F37**; Table **T19**). Aluminum concentrations are less than 2 wt% from 5.25 to 205.02 m CSF-A. There is a single data point at 224.12 m CSF-A where the Al concentration increases to 3.8 wt% before returning to <2 wt% to 295.25 m CSF-A; below this depth, Al values increase and range 0.8–5.9 wt%, showing higher values between ~295 and 345 m CSF-A and lower values near the base of the sedimentary sequence. Silicon and iron distributions follow the vertical distribution of Al with Si averaging 24.7 wt% at 295.25–399.35 m CSF-A, whereas iron concentrations average 5.5 wt% in this same depth interval. Calcium concentrations likely reflect the dominant distribution of calcium carbonate because of the similarity between the Ca concentrations and $CaCO_3$ records. Unlike the other major elements, the Ca record is more elevated in the region shallower than 295.25 m CSF-A (~31 wt%) as compared to the deeper region (6.9 wt%). Potassium concentrations broadly follow Al and Si; however, the peak in K is centered at 343.81 m CSF-A (2.5 wt%). Sulfur concentrations are low (<0.6 wt%) throughout the site.

Ten igneous rock intervals (Lithostratigraphic Units IV–XIV, including Igneous Units 1–10) were designated in Hole U1580A. Most of the igneous units are separated by sedimentary intervals (see **Igneous petrology**). Eleven representative samples from these units were selected for ICP-AES analyses (Table **T20**). Based on classic discrimination diagrams for igneous rocks (Figure **F38**), all samples classify as tholeiitic basalts, plotting along with tholeiitic lavas dredged from the neighboring Mozambique Ridge. The observed variations in SiO_2 and Mg/Zr are caused by crystal fractionation. The rocks show a trend of increasing CaO/Al_2O_3 with decreasing MgO (not shown) indicating the predominant crystallization of olivine and plagioclase feldspar that is consistent with a relatively shallow (low pressure) fractionation trend typical for mid-ocean ridge or many oceanic plateau basalts. No significant downhole variations are observed in the igneous units at

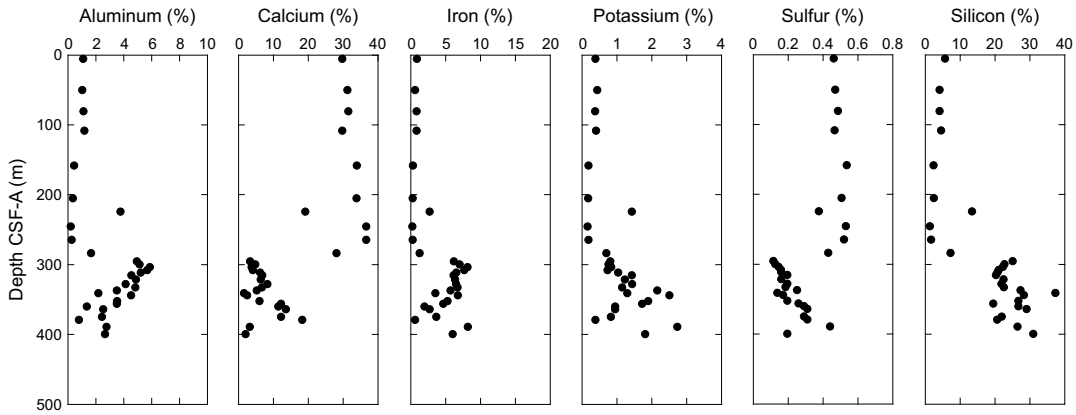

Figure F37. Sediment aluminum, calcium, iron, potassium, sulfur, and silicon, Site U1580.

Table T19. Major and minor element concentrations of sediments, Hole U1580A. **Download table in CSV format.**

Table T20. Major and trace element concentrations of igneous rocks, Site U1580. **Download table in CSV format.**

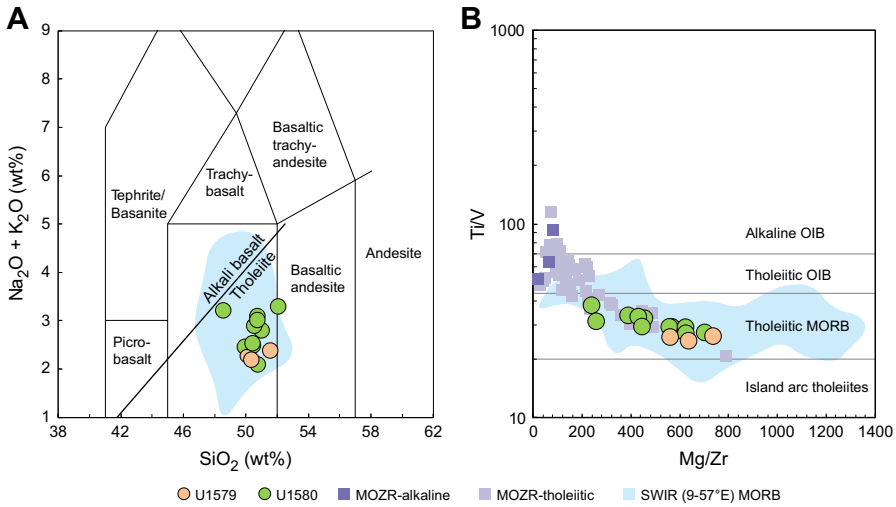

Figure F38. A. Total alkali vs. silica diagram (normalized to 100% on a volatile free basis) with alkaline/tholeiitic boundary after MacDonald and Katsura [1964] and B. Mg/Zr vs. Ti/V from shipboard ICP-AES analyses of igneous units (all data calibrated with liquid standards). Discrimination lines for rock types in (B) are taken from Shervais (2022). All samples plot as tholeiitic basalts. Reference data from dredged samples from neighboring Mozambique Ridge (MOZR) taken from Jacques et al. (2019). Data from the Southwest Indian Ridge (SWIR) from Le Voyer et al. (2019) and references therein. OIB = ocean-island basalt, MORB = mid-ocean-ridge basalt, SWIR = Southwest Indian Ridge.

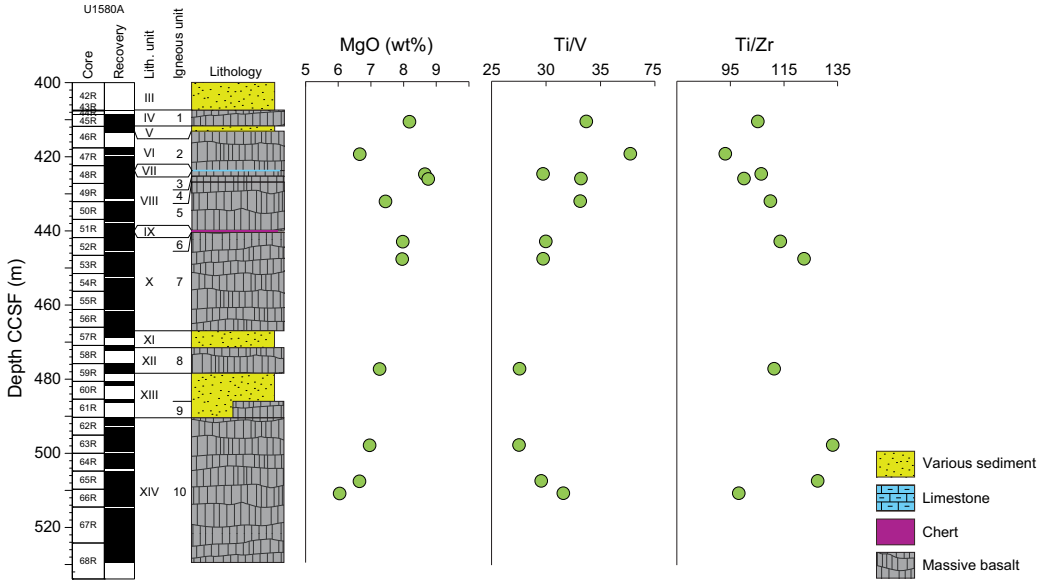

Figure F39. Downhole variations in basalts for MgO (normalized), Ti/V, and Ti/Zr (liquid standard calibration), Site U1580. No significant systematic variation with depth is observed.

Site U1580 (Figure F39). Excluding Sample 392-U1580A-47R-2, 54–57 cm (419.5 m CCSF), from Igneous Unit 2, there appears to be a slight trend toward decreasing MgO content downhole, possibly indicating stronger magma evolution (crystal fractionation). Ratios of immobile incompatible elements such as Ti/V or Ti/Zr show no systematic variations with depth and only limited variability, suggesting no significant changes in magma source composition.

10. Physical properties

Physical properties of sediments and igneous rocks recovered at Site U1580 were measured on whole-round core sections, split-half core sections, and discrete samples to a total depth of 528.58

m CSF-A in Hole U1580A. Complementary downhole logging data sets were also collected in Hole U1580A (see **Downhole measurements**). Between ~40 and 74 m CSF-A, cores from Holes U1580A and U1580B overlap stratigraphically. Measured variations in physical properties arise from lithification with increasing burial depth and from variations in lithologic composition. The upper part of the section shows small variations in MS, NGR, *P*-wave velocity, and density (Lithostratigraphic Unit I and Lithostratigraphic Subunits IIa and IIb; 0 to ~207 m CSF-A). The overall higher *P*-wave velocities, higher densities, and color change toward darker and more reddish layers in the lower part of Lithostratigraphic Subunit IIb (~19.4–207.11 m CSF-A) are attributed to diagenetic changes and to increasing clay content. Anomalous physical properties downcore were recorded for the potassium-enriched zeolitic sandstones to claystones interval of Lithostratigraphic Subunit IIIa. These green zeolitic sandstones to claystones are characterized by a decrease in bulk density, increase in porosity, low *P*-wave velocities (as low as ~2000 m/s), and a sharp drop in thermal conductivity compared to the strata above and below. High MS and NGR values lower in the section (Lithostratigraphic Unit III; ~293.51–407.46 m CSF-A) correspond to zeolitic sandstones and claystones. Exceptional peaks in NGR (related to high U content) were also observed in a few dark layers in Cenomanian–Turonian strata (Lithostratigraphic Unit XII; ~471.6–478.53 m CSF-A; 471.60–478.53 m CCSF) sandwiched between basalt layers (Lithostratigraphic Units XI and XIII).

10.1. Natural gamma radiation

The NGR values for Site U1580 cores range 1–26 counts/s among the various lithostratigraphic units (Figures **F40**, **F41**). NGR is low and does not exceed 12.5 counts/s for most of the shallowest ~207 m in Hole U1580A, including the foraminiferal ooze, nannofossil ooze, and nannofossil chalk of Lithostratigraphic Unit I (~0–3.4 m CSF-A) and Lithostratigraphic Subunits IIa and IIb (~3.4–207.1 m CSF-A) (Figure **F40**). Between 0 and 129.1 m CSF-A, NGR averages 6.5 counts/s, and then it decreases to an average of 3.3 counts/s between 135.9 and 207.1 m CSF-A. In the calcare-

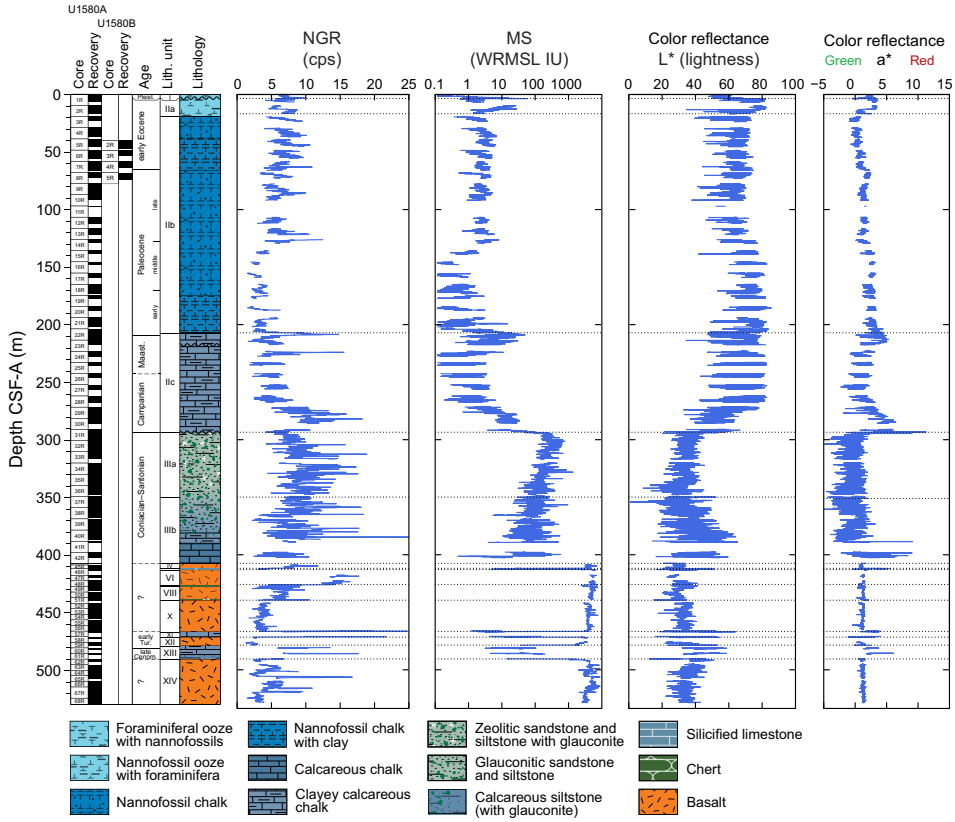

Figure F40. Physical properties, Hole U1580A. All plotted data sets omit data points of poor quality such as from section ends and cracks in the cores. Dotted lines = lithostratigraphic boundaries. cps = counts per second.

ous chalk of Lithostratigraphic Subunit IIc, NGR averages 7.0 counts/s from 207.1 to 293.5 m CSF-A, with the highest values coinciding with clay-rich intervals and reaching a peak of 18.2 counts/s at 281.9 m CSF-A. In the green sandstones, siltstones, claystones, and chalk of Lithostratigraphic Unit III at 293.5–407.5 m CSF-A, NGR averages 8.9 counts/s (Figure **F40**). In the underlying units of basalts and sediments from 407.5 m CSF-A (407.5 m CCSF) to the bottom of Hole U1580A (528.58 m CSF-A; 529.59 m CCSF), NGR is variable. In the basalt of Lithostratigraphic Unit IV (407.5–411.8 m CSF-A; 407.46–411.76 CCSF), NGR varies between 6.8 and 11.8 counts/s (Figure **F41**). In Lithostratigraphic Unit V, which consists of limestone, siltstone, and chert, NGR varies between 3.0 and 4.8 counts/s. The basalt of Lithostratigraphic Unit VI (412.82–426.25 m CSF-A; 413.16–423.78 m CCSF) averages 14.3 counts/s, whereas the basalts of Lithostratigraphic Units VIII (426.3–438.9 m CSF-A; 423.80–439.90 m CCSF) and X (439.5–466.6 m CSF-A; 440.43–468.46 m CCSF) have significantly lower NGR (average = 4.1 counts/s) (Figure **F41**). The sedimentary rocks of Lithostratigraphic Unit XI (466.63–471.6 m CSF-A; 467.09–471.6 m CCSF) have high NGR (as high as 24.8 counts/s), and the basalt of Lithostratigraphic Unit XII (471.6–478.5 m CSF-A; 471.6–478.5 m CCSF) has low NGR (1.3–3.0 counts/s). Recovered sediments from Lithostratigraphic Unit XIII (478.5–490.5 m CSF-A; 478.5–490.5 m CCSF) have higher NGR (as high as 17.6 counts/s). The lowermost basaltic Lithostratigraphic Unit XIV (490.5–528.58 m CSF-A; 490.5–529.28 m CCSF) generally has NGR values between 1.5 and 6.4 counts/s, but four spikes in NGR occur, of which the highest peak is 16.8 counts/s at 506.40 m CSF-A (505.74 m CCSF) (Figure **F41**).

Elemental abundance depth profiles of potassium (K), uranium (U), and thorium (Th) were deconvolved from the Natural Gamma Radiation Logger (NGRL) spectral data from Hole U1580A cores (see **Physical properties** in the Expedition 392 methods chapter [Uenzelmann-Neben et al., 2023a]) and provide additional insights into trends of the full NGR profile, along with geochemical information for the site (Figure **F42**). Deconvolved NGR data reveal an enrichment of U in the foraminiferal ooze of Lithostratigraphic Unit I in the uppermost 3.5 m of the site. Other intervals of elevated U occur in the calcareous siltstone of Lithostratigraphic Subunit IIIb (~370–390 m CSF-A) and in Cenomanian–Turonian Lithostratigraphic Units XI and XIII (~460–490 m CSF-A) (see **Lithostratigraphy**). These intervals of enriched U commonly correspond to darker sedimentary beds and may reflect paleoredox conditions that led to higher organic carbon content preservation and/or authigenic mineral enrichment. From ~294 to 380 m CSF-A, K is enriched to ~0.5–2.0 wt% in the zeolitic sandstones to claystones of Lithostratigraphic Subunit IIIa (Figure **F42**).

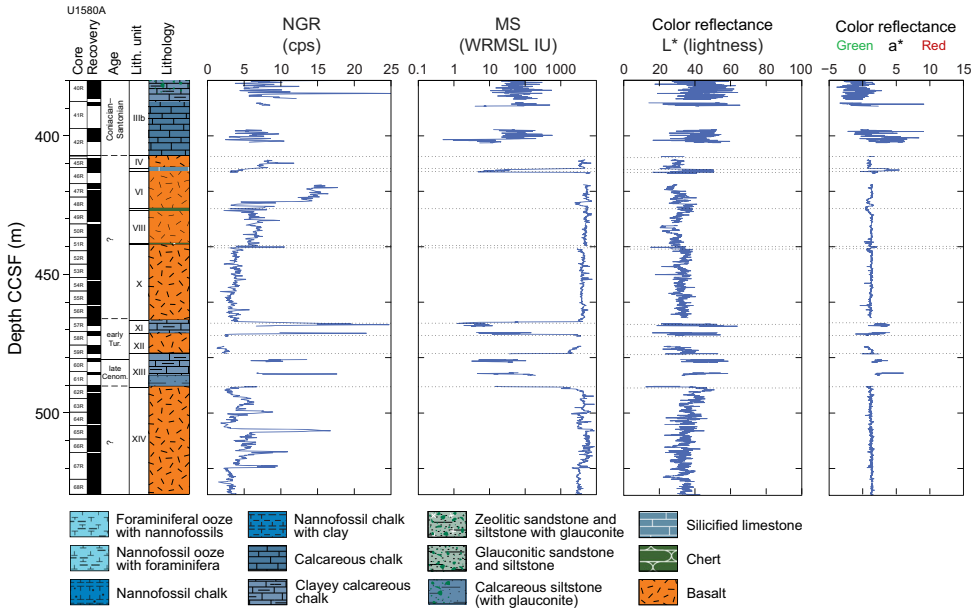

Figure F41. Physical properties data spanning the depth interval with basalt lithologies, Hole U1580A (~380–530 m CCSF). All plotted data sets omit data points of poor quality such as from section ends and cracks in the cores. Dotted lines = lithostratigraphic boundaries. cps = counts per second.

Because this interval of K enrichment does not contain a corresponding increase in U and Th, the increase in NGR in Lithostratigraphic Subunit IIIa cannot be solely explained by increases in the relative content of common clay minerals. Instead, the increase in K derived from spectral deconvolution of NGR likely reflects an increase in authigenic minerals rich in K such as glauconite and celadonite (see **Lithostratigraphy**).

10.2. X-ray images

X-ray imaging was performed on selected half cores from Hole U1580A to investigate the Paleocene/Eocene boundary (Sections 7R-3 and 7R-4) and the K/Pg boundary (Sections 22R-3 and 22R-4). Features related to bioturbation and drilling-induced fracturing were primarily observed.

10.3. Color reflectance

The carbonate-rich lithostratigraphic units at Site U1580 from the seafloor to 293.51 m CSF-A have high total reflectance (L*) ranging 40–84 (average = 67) throughout Lithostratigraphic Unit I (foraminiferal ooze), Lithostratigraphic Subunit IIa (nannofossil ooze), Lithostratigraphic Subunit IIb (nannofossil chalk), and Lithostratigraphic Subunit IIc (clayey calcareous chalk) (Figure **F40**). In a ~2 m thick clay-rich bed in Lithostratigraphic Subunit IIc (Core 392-U1580A-22R; ~207–209 m CSF-A), L* decreases by 20 units and a* (green [negative] versus red [positive] coloration) increases to 5.3. This change indicates a darker and more reddish hue compared to sediments immediately above the K/Pg boundary (see **Lithostratigraphy**). Downcore, in the lower interval of the clayey calcareous chalks of Lithostratigraphic Subunit IIc, L* decreases to ~50 and a* reaches a maximum of 11.2 at 293.29 m CSF-A, reflecting a decrease in carbonate content (Figure **F40**). In the green zeolitic sandstones to claystones of Lithostratigraphic Unit III (293.51–383.80 m CSF-A), L* mostly varies between 20 and 50, showing values as high as 45 near the base of Lithostratigraphic Unit III at 407.51 m CSF-A. The succession of basalts and thinner sedimentary units below 407.51 m CSF-A (Lithostratigraphic Units IV–XIV) has generally low L* of ~30, showing

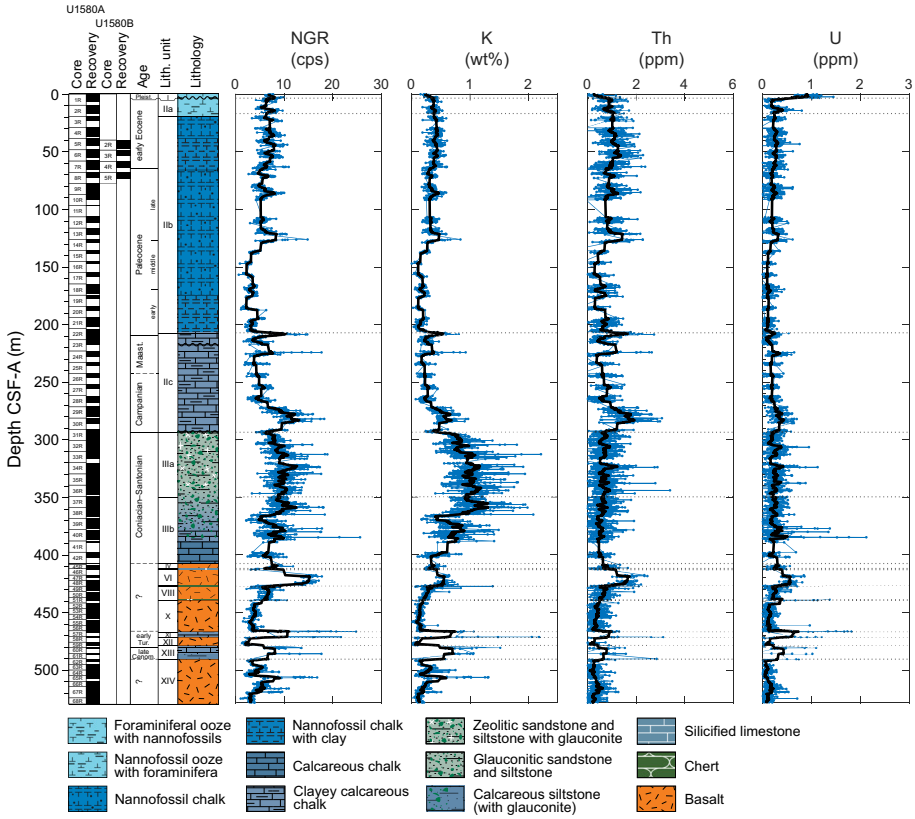

Figure F42. NGR and K, Th, and U abundances from deconvolution of the total NGR energy spectra, Holes U1580A and U1580B. Black lines = 25 point moving averages, dotted lines = lithostratigraphic boundaries.

values as high as 45 in sedimentary lithologies such as in Lithostratigraphic Unit XI between 466 and 471.62 m CSF-A (Cores 57R–58R; 467.63–471.62 m CCSF) (Figure **F41**).

10.4. Magnetic susceptibility

MS values measured on both the Whole-Round Multisensor Logger (WRMSL) and Section Half Multisensor Logger (SHMSL) range across several orders of magnitude among the different lithostratigraphic units at Site U1580 (Figure **F40**). The uppermost ~294 m of the site has the lowest MS (0–65 instrument units [IU]), with most values less than ~10 IU. This trend is consistent with the high carbonate content in the nannofossil-rich Lithostratigraphic Unit II (3.42–293.51 m CSF-A) and is occasionally punctuated by spikes in MS in clay-rich beds, as indicated by correlative NGR peaks (e.g., at ~207–210 m CSF-A). In general, MS correlates positively with NGR in the uppermost ~294 m of the sedimentary sequence at Site U1580 (Figure **F40**). MS increases sharply to ~200–1000 IU directly below the contact with the underlying zeolitic sandstone to claystones of Lithostratigraphic Subunit IIIa at ~294 m CSF-A and declines between ~300 and 400 m CSF-A to values that are mostly less than ~200 IU in the calcareous siltstones of Lithostratigraphic Subunit IIIb. In the underlying basalt units that comprise the main lithology between 407.5 and 528.6 m CSF-A (407.5–529.59 m CCSF), MS is elevated and on the order of ~1,000–10,000 IU (Figure **F41**). Minor sedimentary layers interbedded between basalt units have much lower MS values that are generally less than ~100 IU. MS exhibits an inverse relationship with NGR in the lowermost interval of Site U1580 below ~400 m CSF-A, where sediments are characterized by low MS and high NGR and basalts are mostly characterized by high MS and low NGR (Figure **F40**). However, the basalts at 418.96–425.59 m CSF-A (418.96–423.12 m CCSF) exhibit high NGR (>10 counts/s) and high MS (>1000 IU) (Figure **F41**). This may relate to original magmatic or postemplacement alteration processes in this unit (see **Igneous petrology**).

10.5. Bulk density, grain density, and porosity

Moisture and density (MAD) analyses were performed on 90 discrete samples from Hole U1580A (2 per full core; 1 per half core) (Figures **F43**, **F44**). The bulk density of sediments at Site U1580 increases downcore from ~1.8 g/cm^3 in the foraminiferal ooze of Lithostratigraphic Unit I (0–3.42 m CSF-A) immediately below the seafloor to ~2.3 g/cm^3 near the base of the clayey nannofossil chalk of Lithostratigraphic Subunit IIc (~294 m CSF-A) (Figure **F43**). Bulk density decreases sharply below the contact with the underlying green zeolitic sandstones to claystones of Litho-

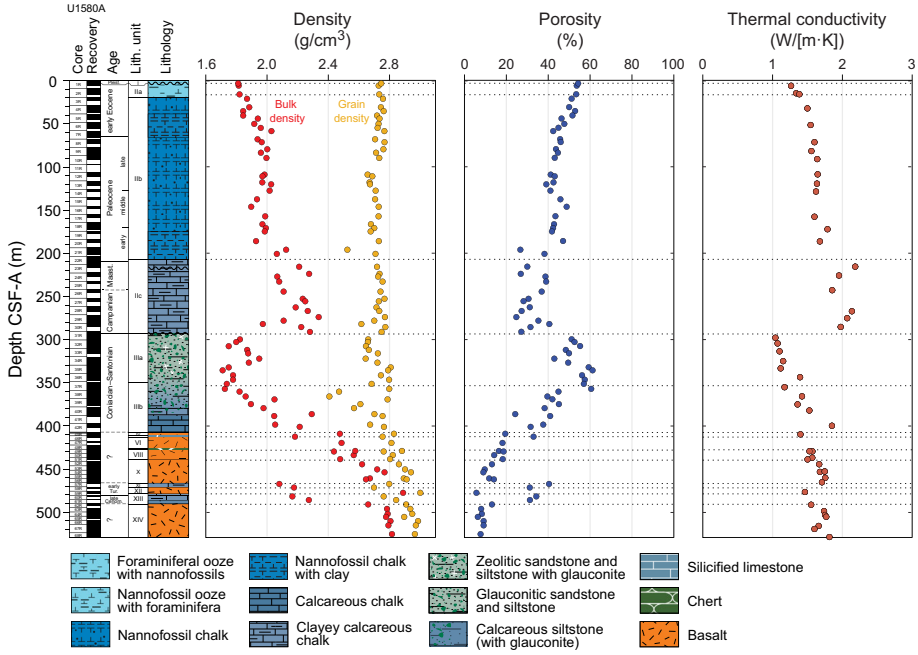

Figure F43. MAD and thermal conductivity results, Hole U1580A. Dotted lines = lithostratigraphic boundaries.

stratigraphic Subunit IIIa (~294–407.5 m CSF-A), reaching ~1.7 g/cm^3 at ~335 m CSF-A. Below this interval, density increases downcore to the highest values for the site (~2.8 g/cm^3) in the lowermost basalt layer. The bulk density values measured from MAD analyses are on average 0.1–0.2 g/cm^3 higher than the gamma ray attenuation (GRA) bulk density measured using the WRMSL (Figures **F45**, **F46**). However, both techniques resolve similar trends in bulk density with depth and can be compared with downhole density logs (see **Downhole measurements**).

Trends in MAD bulk density at Site U1580 correlate inversely with changes in porosity (Figures **F43**, **F44C**). Porosity mainly decreases downcore from ~55% in the foraminiferal ooze near the seafloor to less than 20% in the basalt lithologies at the base of the cored interval (deeper than 500 m CSF-A). One exception to this trend is that the porosity of the zeolitic sandstones to claystones of Lithostratigraphic Subunit IIIa (~294–350 m CSF-A) is sharply higher (~50%–60%) than in the overlying nannofossil chalks of Lithostratigraphic Subunit IIc (20%–40%) (Figure **F43**). Grain density is generally ~2.6–2.8 g/cm^3 in the sedimentary strata through the uppermost ~400 m of the site, consistent with high carbonate content in Lithostratigraphic Units I–III (see **Geochemistry**; Figure **F43**) and somewhat lower grain density values in the siliciclastic (<10 wt% $CaCO_3$) Lithostratigraphic Unit IIIa. Increases in bulk density for sedimentary lithologies at Site U1580 correlate with decreases in porosity from burial compaction and/or carbonate cementation of pore spaces, as opposed to changes in grain density (mineral content) (Figure **F44D**). Conversely for igneous lithologies, downcore increases in bulk density correlate with both a decrease in porosity and an increase in grain density (Figure **F44C**).

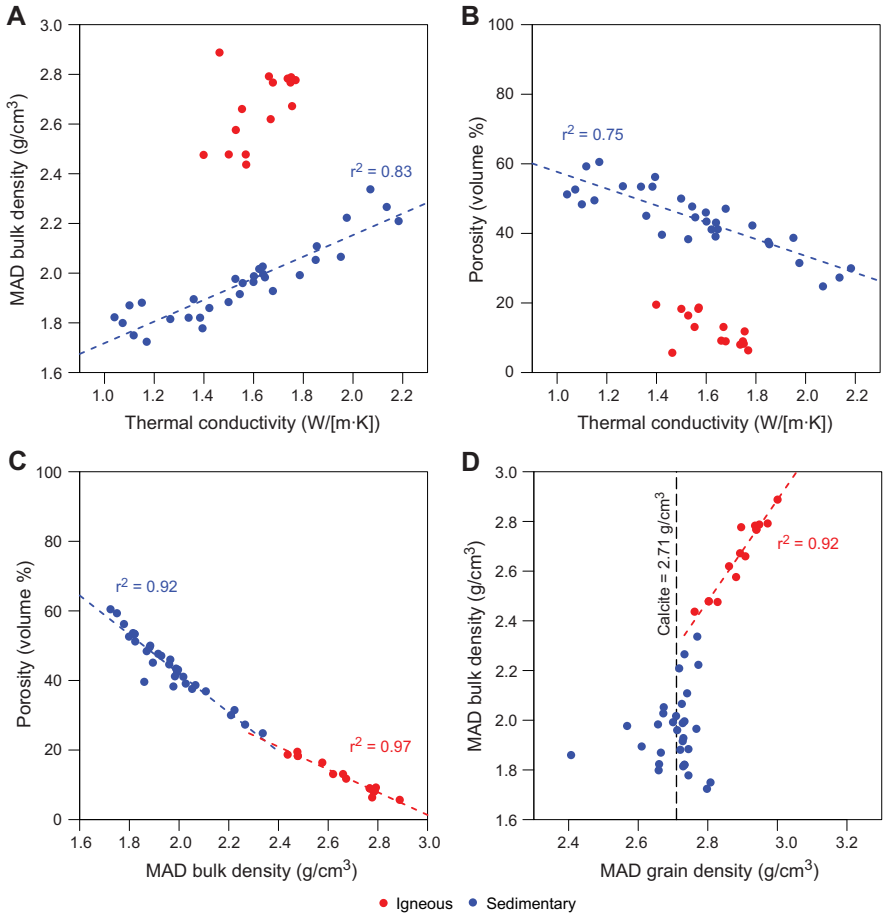

Figure F44. MAD results, Hole U1580A. A. MAD bulk density vs. thermal conductivity. B. Porosity vs. thermal conductivity. C. Porosity vs. MAD bulk density. D. MAD bulk density vs. MAD grain density (vertical dashed line = grain density of calcite). Thermal conductivity data were paired with the closest MAD measurement from a maximum depth offset of 3 m.

10.6. *P*-wave velocity

The *P*-wave velocities of Site U1580 cores were measured using the *P*-wave logger (PWL) on the WRMSL at a spatial resolution of 2.5 cm and using the *P*-wave caliper (PWC) system on one to two samples per core. In addition to standard track and caliper measurements, four discrete basalt samples were analyzed for *P*-wave directional information. *P*-wave velocity increases with depth from ~1600 m/s at the seafloor to ~2500 m/s at ~207 m CSF-A (Lithostratigraphic Unit I through

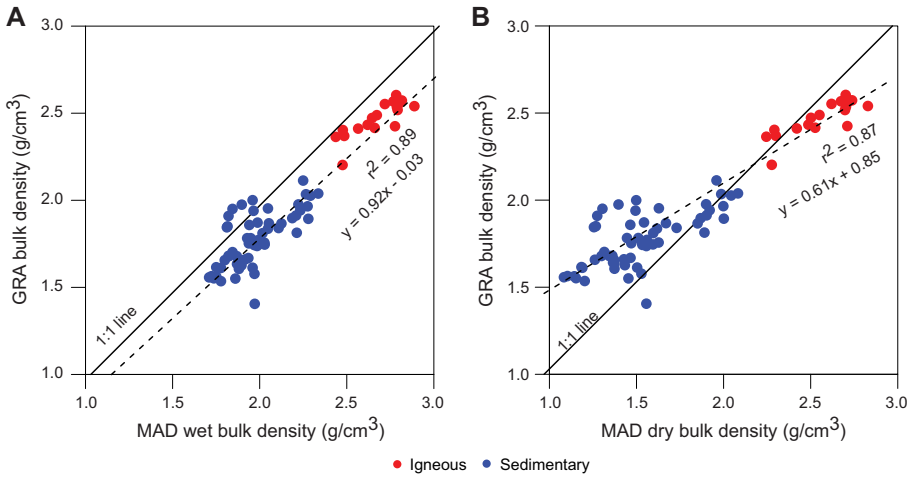

Figure F45. Bulk density, Site U1580. A. GRA bulk density vs. MAD wet bulk density. B. GRA bulk density vs. MAD dry bulk density. MAD data were paired with the closest GRA bulk density measurement from a maximum depth offset of 2 cm. The plotted GRA bulk density data omit data points of poor quality such as from section ends and cracks in the cores.

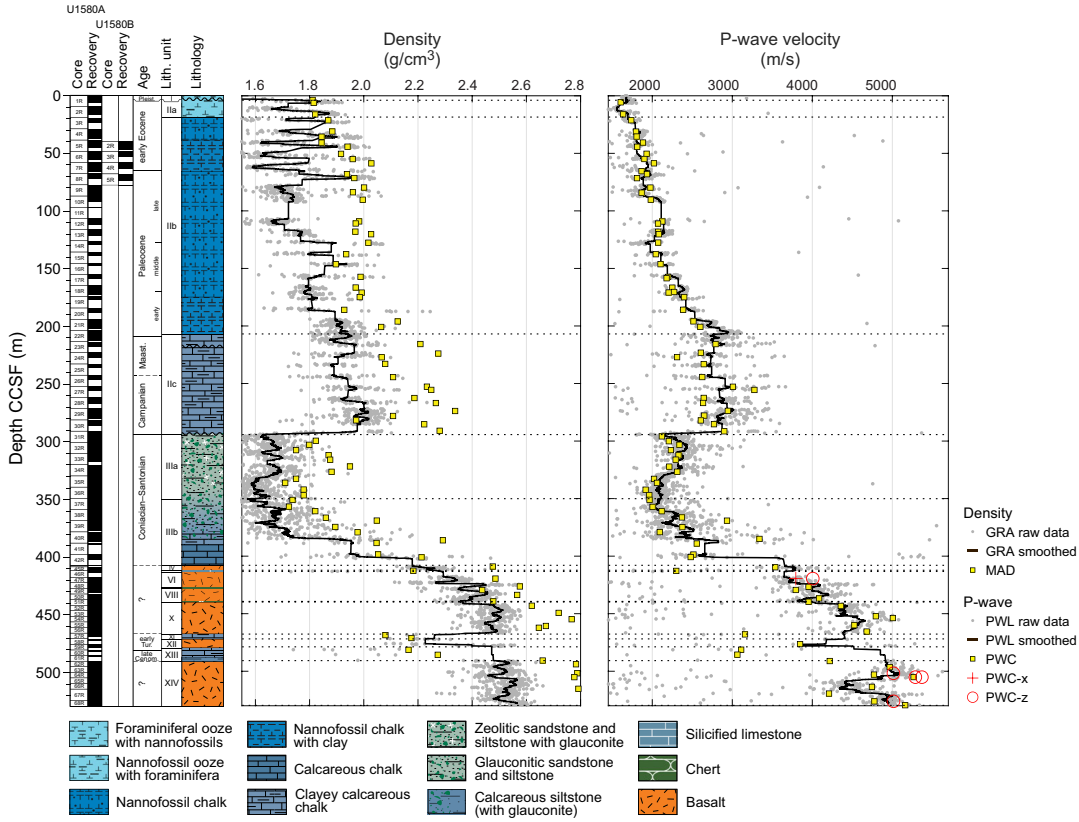

Figure F46. WRMSL density and *P*-wave velocity, Site U1580. All plotted data sets omit poor quality data points such as from section ends, cracks in the cores, or poor contact between the core and core liner.

Lithostratigraphic Subunit IIb) (Figure **F46**). PWC *P*-wave velocity data in the underlying Lithostratigraphic Subunit IIc (207–294 m CSF-A) are mostly between ~2600 and ~3000 m/s. The zeolitic sandstones to claystones of Lithostratigraphic Subunit IIIa (~294–350 m CSF-A) and calcareous siltstones of Lithostratigraphic Subunit IIIb (~350–407.5 m CSF-A) have relatively low *P*-wave velocities, as low as ~2000 m/s. The *P*-wave velocities measured in basalts below 407.5 m CSF-A range ~4000 to ~5000 m/s, with larger values characteristic for the deeper basalt layers (Figure **F46**). The measurements on discrete samples indicate 5%–10% larger vertical (*z*-) velocities compared to horizontal (*x*-) velocities in the lower basalt Lithostratigraphic Unit XIV (490.54–528.58 m CSF-A). The upper basalt units are more isotropic. The sedimentary rocks interbedded in the basalt sequence have *P*-wave velocities of 3000–3500 m/s. Comparisons of *P*-wave velocities from the PWC system and smoothed *P*-wave velocities from the WRMSL PWL show relatively good agreement in downcore trends between both data sets (Figure **F46**).

10.7. Thermal conductivity

Thermal conductivity was measured on section halves using a puck probe (Figure **F43**). Section halves of igneous rocks were immersed in seawater during measurement, following 6 h of soaking in a seawater bath under vacuum (see **Physical properties** in the Expedition 392 methods chapter [Uenzelmann-Neben et al., 2023a]). In both the igneous and sedimentary lithologies at Site U1580, thermal conductivity values correlate inversely with porosity and positively with MAD bulk density (Figure **F44A, F44B**). Thermal conductivity at Site U1580 increases downcore from ~1.2 W/(m·K) at the seafloor to ~2.0 W/(m·K) at 285.3 m CSF-A near the base of Lithostratigraphic Unit II (Figure **F43**). This downcore increase in thermal conductivity is associated with a decrease in porosity to ~30%. Thermal conductivity sharply drops below the contact with the more porous zeolitic sandstones to claystones of Lithostratigraphic Unit III (near ~300 m CSF-A) from ~2.0 to ~1.1 W/(m·K). These anomalously low values of thermal conductivity are probably controlled by both porosity and the zeolitic composition of Lithostratigraphic Unit III. Thermal conductivity in the interbedded sequence of basalts and chalk/claystone below ~407 m CSF-A is between 1.40 and 1.82 W/(m·K); higher values are typical for the less porous basalts, and lower values are typical for sediments (Figures **F43**, **F44**).

11. Downhole measurements

Downhole measurements at Site U1580 consisted of wireline logging of Hole U1580A on 5 and 6 March 2022. No downhole temperature data were measured at this site. In addition to standard sonic and MS data, high-resolution density, NGR, neutron porosity, and electrical resistivity logging, FMS and UBI imagery provided a continuous borehole record, documenting lithologies of unrecovered stratigraphic intervals where coring gaps occurred in Hole U1580A. Thorium/potassium ratios from downhole gamma ray spectroscopy data indicate that sediments of Lithostratigraphic Units II and III occupy two distinct compositional domains. The potassium-rich Lithostratigraphic Unit III is characterized by anomalously high porosity (>60%), which is confirmed by MAD analysis. The integrated interpretation of downhole data was instrumental in identifying the nature of contacts and true thicknesses of interbedded sediments and basalts below 407 m WMSF (see **Lithostratigraphy** and **Physical properties**). The UBI and FMS images display various degrees of alteration and fracturing in basalts and sharp transitions to the interbedded sediments. The sedimentary rocks interbedded within basalt units are characterized by elevated uranium abundance with peaks at about 2 ppm. The cross-dipole setup of acoustic logging enables a detailed core-to-seismic integration, including the analysis of elastic anisotropy.

11.1. Wireline downhole logging

Following the completion of RCB drilling at Hole U1580A, the bit was dropped and the BHA was retracted to 80.7 WMSF (see **Operations**). The borehole was displaced with seawater without adding barite muds to stabilize the borehole because the UBI acoustic imaging requires a transparent borehole fluid. The local tidal range was minimal (<0.5 m) during the logging session, and the sea state was calm to moderate with an average heave of 1–1.5 m and occasional larger swells. On each run, the wireline heave compensator (WHC) was engaged when the tool string was lowered

past the BHA to minimize distortion of logging records between the different logging passes. In chronological order of deployment, the wireline logging tool strings (see Figure **F22** in the Expedition 392 methods chapter [Uenzelmann-Neben et al., 2023a]) consisted of the following: (1) the triple combo, which included the MSS, the HNGS, the High-Resolution Laterolog Array (HRLA), the Accelerator Porosity Sonde (APS), and the HLDS; (2) the FMS and DSI, which also included the HNGS and the GPIT to orient 360° FMS resistivity images of the borehole wall; and (3) the UBI, GPIT, and HNGS.

On the initial downpass, the triple combo recorded a maximum borehole depth of ~533.9 m WMSF, which is ~10 m shallower than expected from coring. This may have resulted from fall-in of rubble left behind after coring the lowermost sediments and basalts in the hole. The first uplog measured between the total borehole depth of ~534 and 354 m WMSF and was considered the repeat pass. To prevent neutron activation of the formation, the APS was not engaged because it would have produced artificial gamma radiation in the borehole wall and biased HNGS data on the subsequent main pass. The main pass was the second and final uplog of the triple combo run. It was conducted at a reduced logging speed of 274.3 m/h (900 ft/h) to permit collection of logging data at a finer depth resolution from ~533 to ~80 m WMSF.

To improve the resolution of composite FMS resistivity images of the borehole wall, the FMS-sonic run consisted of two main passes at 457 m/h (1500 ft/h) over 127–503 m WMSF (first pass) and 90–508 m WMSF (second pass). The DSI was run in anisotropic mode to obtain slow and fast *S*-wave directions in the horizontal plane. A successful single pass of the UBI from 505 to 390 m WMSF spanned the depth interval of igneous lithologies observed in cores. At the start of a second pass, the transducer subassembly motor began stuttering and sticking, most likely from settled debris at the base of the hole; the second pass was therefore not completed, and the UBI was brought to the surface. The GPIT was run on both the FMS-sonic and UBI tool strings to spatially orient imaged features of the borehole wall.

After logging, the preprocessed logs were sent to the Lamont-Doherty Earth Observatory Borehole Research Group (LDEO-BRG), where the logs were processed and then sent back to the ship during the expedition. One aspect of this processing involved shifting the wireline logging data to a depth scale referenced to the seafloor, which was determined by steps in HSGR (standard total NGR) and resistivity observed on the downpass of the triple combo at 2572 m drilling depth below rig floor (DRF) in Hole U1580A. Additionally, logging data were corrected for variations in the borehole diameter in Hole U1580A, which were measured using a hydraulic caliper during the main passes of each tool string run. The quality of the borehole was good to excellent for downhole logging. Caliper measurements indicated a borehole diameter of less than 31.8 cm (12.5 inches) for the majority of the main pass of the triple combo, which is similar to the 25.1 cm (9.875 inches) diameter of the RCB drill bit (Figure **F47**). Caliper measurements exceeded 35.6 cm (14 inches) in diameter between ~290 and 330 m WMSF and between ~110 and 140 m WMSF, suggesting minor washout of the borehole walls in these two intervals. Measurements using logging tools that require contact with the borehole wall, such as the HLDS, HRLA, and FMS-sonic, can be affected by wide (30.5 cm; >12 inches) or irregular borehole size. As a result, logging data in these intervals from Hole U1580A should be interpreted with caution.

The processed downhole wireline logs are presented in Figure **F47**. The in situ data are generally in good agreement with physical properties measurements from whole-round, split-core, and discrete samples aboard ship (Figure **F48**). The differences between the WMSF and CSF-A depth scales are assumed to be <1 m, which is below the uncertainty of determination of the seafloor depth.

11.1.1. Natural gamma radiation

The HNGS measured the HSGR of the borehole wall in Hole U1580A (Figure **F47**). Prominent peaks and trends in the downhole HNGS data can be readily correlated to NGR data measured from the cores on the NGRL (see **Stratigraphic correlation**). In Hole U1580A, HSGR ranges 5–30 American Petroleum Institute gamma radiation units (gAPI) from 80 to ~490 m WMSF. The nannofossil oozes and chalks of Lithostratigraphic Unit II (to ~294 m CSF-A) are generally characterized by HSGR values below 10 gAPI (Figure **F47**), apart from several meter-thick peaks of about

20–25 gAPI at ~125 and ~210 m WMSF. HSGR increases below about 275 m WMSF, corresponding to the lower part of Lithostratigraphic Subunit IIc (207.11–293.51 m CSF-A), and reaches 25–30 gAPI in the zeolitic sandstones and siltstones of Lithostratigraphic Unit III (293.51–407.46 m CSF-A). In the lower part of the borehole (380–500 m WMSF), basalt lithologies are generally characterized by low HSGR (5–15 gAPI), whereas interbedded sedimentary lithologies are significantly more radioactive, exhibiting HSGR values of 20–30 gAPI (Figure **F49**).

The HNGS also logged elemental abundances of U, Th, and K based on downhole gamma ray spectroscopy data. Estimated abundances of K are equivalent between the HNGS measurements from downhole logging data and the NGR spectral deconvolution data of NGRL core data from Hole U1580A (R = 0.91) (Figure **F48**). U and Th abundances as measured using the different methods are less consistent (R = 0.42 and R = 0.63, respectively). This may be due to the relatively low U and Th abundances in Hole U1580A, which likely approach detection limits and have smaller amplitude spectral peaks for the gamma radiation associated with the daughter products of these elements.

Ratios of Th and K abundance can be used to evaluate clay mineralogy (Figure **F50**). The average Th/K ratio between 100 and ~293 m WMSF is ~4.5. These values are characteristic for illite and montmorillonite clays (Quirein et al., 1982), suggesting that these minerals are dominant in the clay fraction in Lithostratigraphic Units I and II. Th/K ratios between ~293 and 407 m WMSF are distinctly lower, clustering between 0.5 and 2 (mean K abundance = ~1 wt%). This indicates the presence of potassium-rich and thorium-poor clay minerals such as glauconite and/or micas (Quirein et al., 1982) in Lithostratigraphic Unit III (293.51–407.46 m CSF-A).

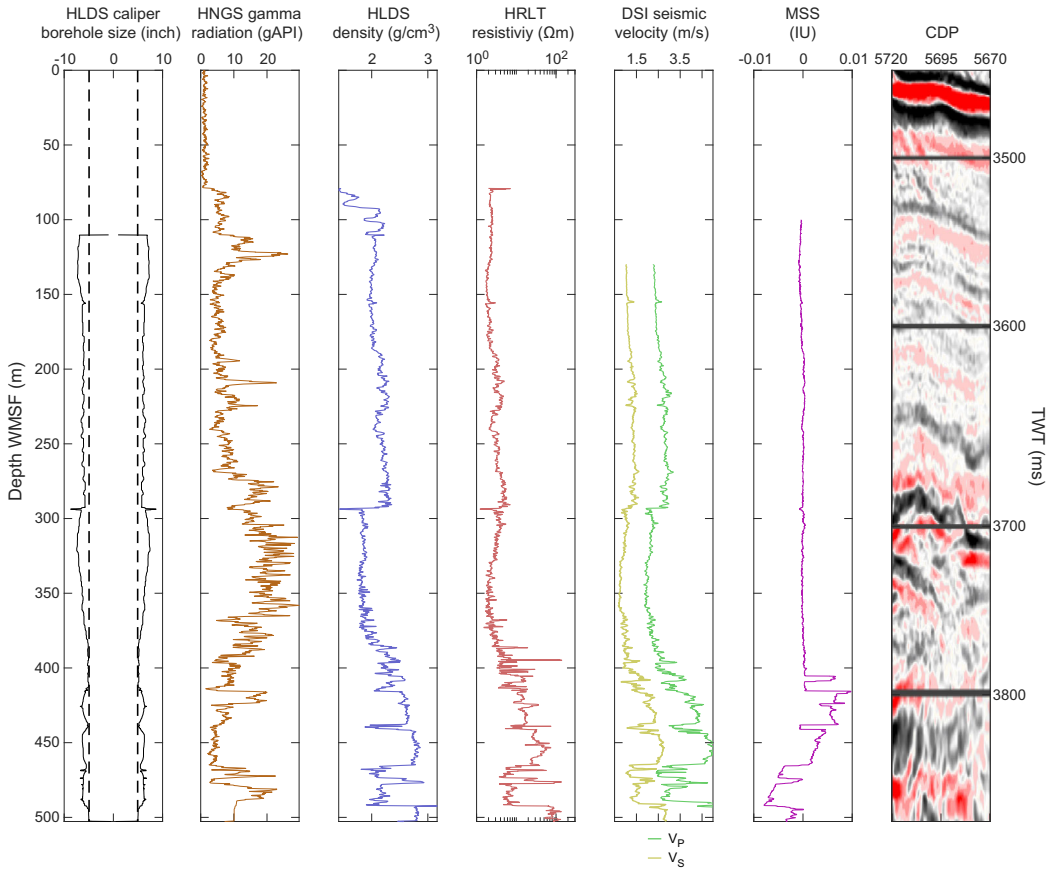

Figure F47. Downhole wireline logging results, Hole U1580A. Right column shows 50 traces of Seismic Line AWI-98015 in two-way traveltime (TWT) around Site U1580, located at common depth point (CDP) 5695. HLRT = High-Resolution Laterolog Array.

11.1.2. Downhole electrical resistivity and Formation MicroScanner

The HRLA measured a downhole resistivity profile for Hole U1580A, and high-resolution resistivity images of the borehole wall were obtained using the FMS (Figure **F49**). Electrical resistivity increases with depth from 2 to 5 Ωm in the sedimentary succession (Figure **F47**). Resistivity drops gradually to 1–2 Ωm in the borehole depth interval (~293–350 m WMSF) that consists of the zeolitic sandstones to siltstones of Lithostratigraphic Subunit IIIa (293.51–349.98 m CSF-A). This contrast of electrical properties is associated with the transition to more porous lithologies (see **Neutron porosity**). Borehole resistivity increases to 10–50 Ωm (locally to 100 Ωm) between 390 and 400 m WMSF in the lowermost depth interval of Lithostratigraphic Unit III. The upper basalt units have electrical resistivity of 20–30 Ωm, whereas the lower basalt unit (Lithostratigraphic Unit XIV; below ~490 m WMSF) has higher resistivity (~100 Ωm and up to ~250 Ωm locally), indicating less alteration (Figures **F47**, **F49**). Resistivity drops to 5–10 Ωm in the siltstones and claystones that are interbedded with basalts (e.g., 478–490 m WMSF).

The FMS logs provide in situ resistivity images of the borehole wall to resolve lithostratigraphic contacts along with finer scale bedding and structural features such as faults and fractures (Figures **F47**, **F49**). The oriented images cover about a 30° angle in each of four geographic directions, with 0° corresponding to the north. The FMS logs provide high-resolution information to characterize

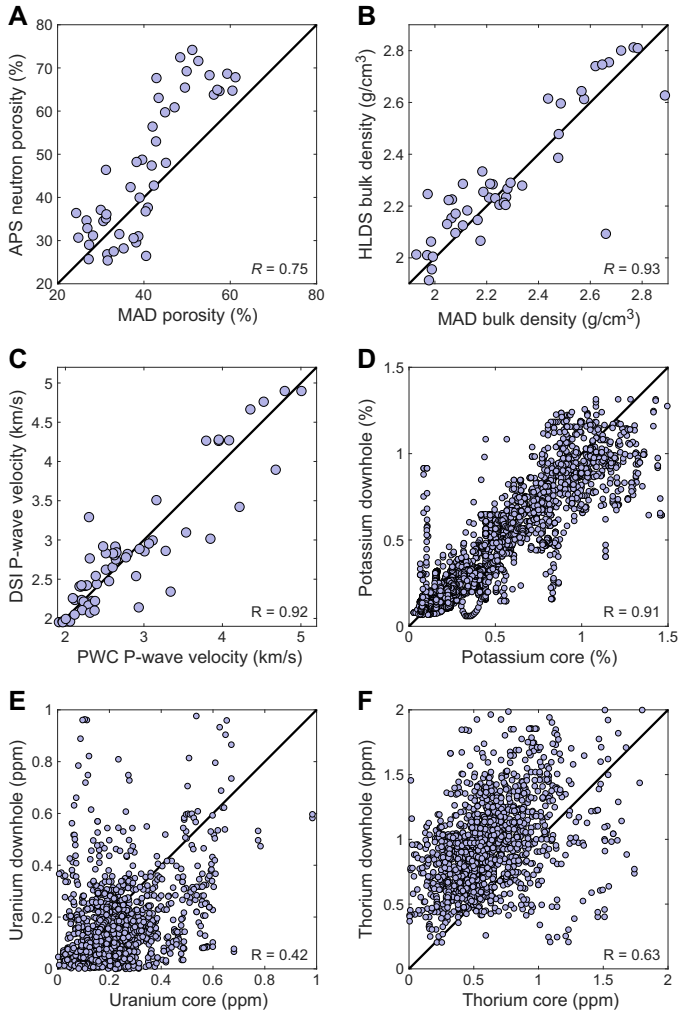

Figure F48. Data crossplots from core samples vs. downhole observations (150–500 m WMSF). A. Porosity. B. Bulk density. C. *P*-wave velocity. NGR spectroscopy results: D. Potassium. E. Uranium. F. Thorium. Downhole elemental abundance data are from the HNGS log of Hole U1580A through the sedimentary lithologies at depths shallower than 400 m WMSF. On the uranium and thorium content graphs, some points are negative. This is an artifact caused by noise in the data and low abundances.

intervals of poor core recovery such as 90–194, 216–272, 386–422, and 467–480 m CSF-A. For example, the true thicknesses of Lithostratigraphic Units V (411.76–412.82 m CSF-A; 411.76–413.16 m CCSF) and XI (466.63–471.60 m CSF-A; 467.0–471.60 m CCSF), based on interpretation of logging data, are about 6.0 and 7.8 m, respectively. That is significantly thicker than estimates from recovered core samples. The FMS images resolve a sharp contact between the lowermost basalt Lithostratigraphic Unit XIV (below 490.54 m CSF-A) and overlying sediments, suggesting that the rock fragmentation in cores across this boundary was caused by drilling (Figure **F49**).

11.1.3. Seismic velocity

The DSI *P*-wave velocities (V_P) and *S*-wave velocities (V_S) in Hole U1580A follow the same trends as those measured on cores using the PWC and WRMSL PWL (Figure **F48C**). The correlation coefficient (R) between the DSI V_P and PWC velocities is 0.92. The upper dipole shear data had the best coherency between the lower and the upper dipoles. Both the compressional and shear wave data recorded using the monopole source were also of excellent quality. However, PWC velocities measured on the cores of carbonate lithologies (Figure **F46**) are 100–300 m/s lower than V_P measured on the DSI (Figures **F47**, **F49**). Seismic velocities increase downhole from 2300 to ~2900 m/s for V_P and from 1010 to ~1470 m/s for V_S at the base of Lithostratigraphic Unit II (293.51 m CSF-A). The seismic velocities sharply drop to a V_P of ~2030 m/s and V_S of ~830 m/s across the contact with the underlying zeolitic sandstones to claystones of Lithostratigraphic Subunit IIIa (293.51–349.98 m CSF-A) and slightly increase toward the bottom of Lithostratigraphic Subunit

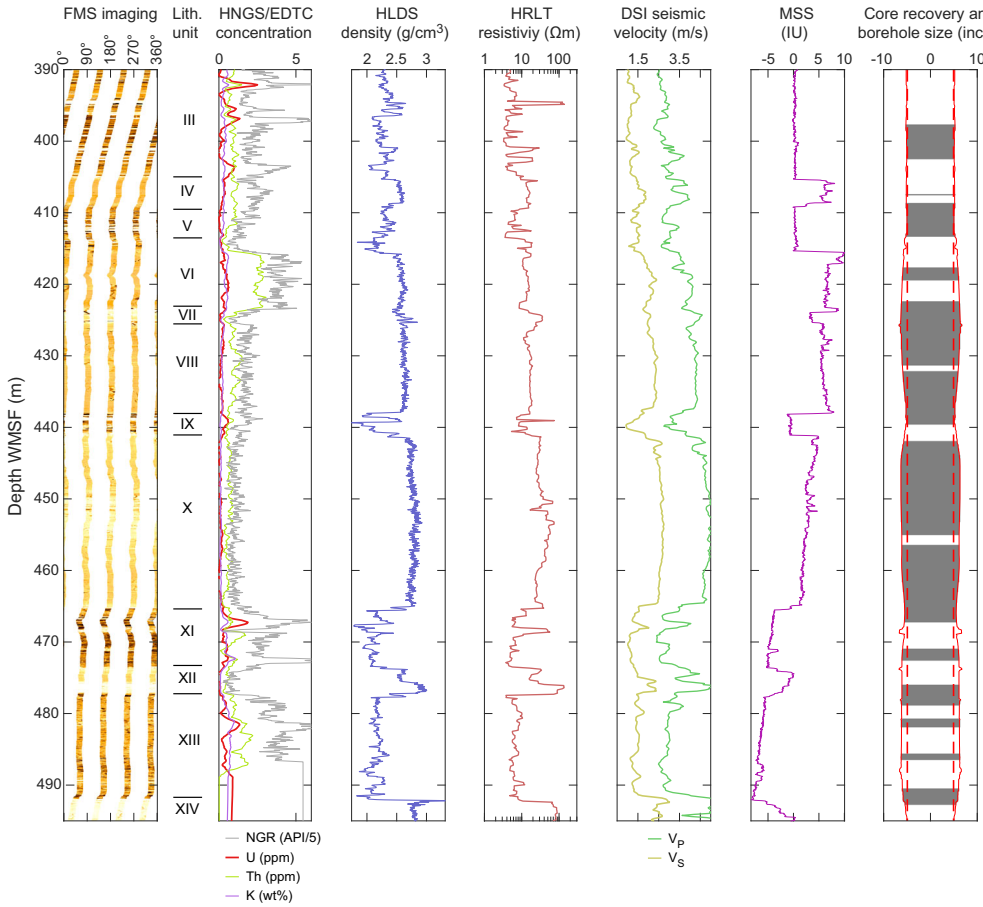

Figure F49. High-resolution downhole wireline logging results for the lower part of Hole U1580A. FMS images span about 30° in each direction, and the darker color corresponds to lower resistivity. EDTC = Enhanced Digital Telemetry Cartridge. API/5 = gAPI units divided by five plotted on the same axis as K, U, and Th abundances. HLRT = High-Resolution Laterolog Array. Dashed red line = size of the drill bit, solid red line = caliper borehole size, gray shaded regions = recovered core intervals.

IIIb (349.98–407.46 m CSF-A). The seismic velocities of the basalts increase with depth and show an average V_P of 4100 m/s for Lithostratigraphic Units IV–X, 4750 m/s for Lithostratigraphic Unit XII, and 5200 m/s for Lithostratigraphic Unit XIV. Sedimentary lithostratigraphic units interbedded with basalts have a significantly lower average V_P of ~2500 m/s. The multichannel seismic reflection data (AWI-98015) were depth converted using the borehole *P*-wave velocities. The prominent reflection at about 3700 ms (~300 m WMSF) with a negative impedance contrast corresponds to the transition from the nannofossil chalk of Lithostratigraphic Subunit IIc to the underlying zeolitic sandstone, siltstone, and claystone lithologies of Lithostratigraphic Unit III (Figure **F47**). Lithostratigraphic Unit II contains weak seismic reflection signatures.

11.1.4. Density

HLDS density of the borehole wall in Hole U1580A generally follows the *P*-wave velocity trend (Figure **F47**). A sharp drop in density below ~294 m WMSF marks the contact between the nannofossil chalk of Lithostratigraphic Subunit IIc (207.11–293.51 m CSF-A) and the underlying zeolitic sandstones to claystones of Lithostratigraphic Subunit IIIa (293.51–349.98 m CSF-A). Significant fluctuations in HLDS density of more than 0.5 g/cm^3 are observed at the contacts between igneous and interbedded sedimentary lithostratigraphic units below ~380 m WMSF (Figure **F49**). Bulk density values determined using MAD analyses of core samples are found to be in good agreement with HLDS density downhole logs (R = 0.93) (Figure **F48B**).

11.1.5. Neutron porosity

The high-resolution APS neutron logging tool was engaged to provide porosity from ~533 to 100 m WMSF. APS downhole logs follow similar trends with porosity determined by MAD analyses (Figure **F48A**). The average porosity ranged from about 10% in the basalt lithologies to 30%–40% in the sedimentary lithologies. The porosity has a step change to 60%–85% below ~294 m WMSF at the contact of the nannofossil chalk of Lithostratigraphic Subunit IIc (207.11–293.51 m CSF-A) with the underlying zeolitic sandstones and siltstones of Lithostratigraphic Subunit IIIa (293.51–407.46 m CSF-A). The comparison with MAD analysis indicates an anomalously high neutron porosity in Lithostratigraphic Subunit IIIa, which may relate to bounded water contained in clay minerals such as zeolites or to biases from washouts and a poor contact with the borehole wall.

11.1.6. Ultrasonic Borehole Imager

High-resolution UBI images were recorded in good detail with minimum influences of stick and slip from ship heave (Figure **F51**). The sampling rate of UBI images was 0.5 cm (0.2 inch). The

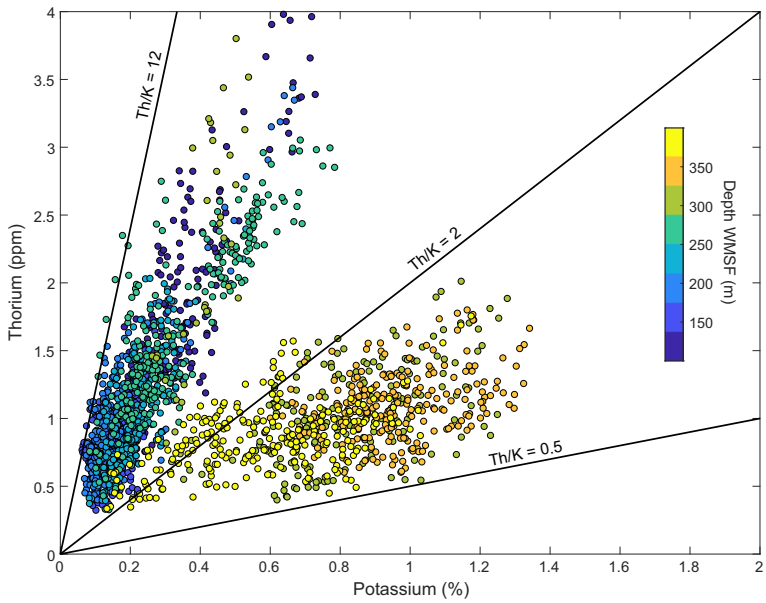

Figure F50. Crossplot of Th vs. K abundance data from the HNGS log, Hole U1580A. Sedimentary lithologies from depths shallower than 400 m WMSF are shown.

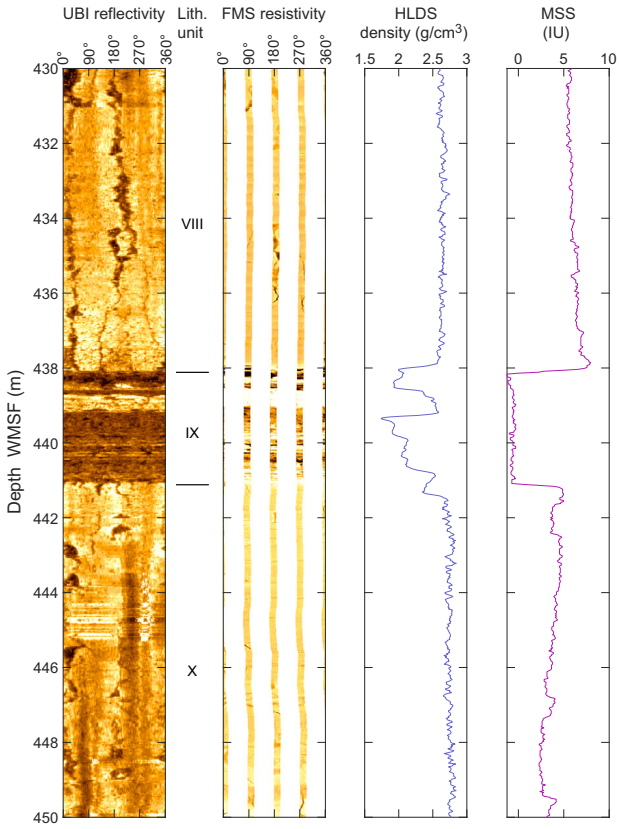

Figure F51. High-resolution UBI and resistivity along with density and MSS logs for igneous units, Hole U1580A.

angular resolution was 180 samples per revolution using a 500 kHz source frequency. The UBI imagery covered the basalt interval, including the uppermost contact with overlying sediments (386–501 m WMSF).

The ultrasonic imaging of the basalt interface with sedimentary Lithostratigraphic Unit IX illustrates details of the transition zone at about 440 m WMSF (Figure **F51**). The true thickness of Lithostratigraphic Unit IX (438.97–439.49 m CSF-A; 439.90–440.42 m CCSF) is about 2.5 m larger than the recovered core length. Ultrasonic imaging indicates that the unit contains a contrasting low-MS layer with low resistivity and high density. This can be interpreted as an altered basalt or a chert layer. The basalts contain subvertical fractures that can be roughly oriented in the north–south (0°–180°) direction. The presence of fractures can explain lower seismic velocities in the upper basalt unit compared to the deeper section. The vertical dark stripes in the lower part of the image are probably due to the tool being not precisely centered in the borehole and/or an elliptic borehole.

References

Agnini, C., Fornaciari, E., Raffi, I., Catanzariti, R., Pälike, H., Backman, J., and Rio, D., 2014. Biozonation and biochronology of Paleogene calcareous nannofossils from low and middle latitudes. Newsletters on Stratigraphy, 47(2):131–181. **https://doi.org/10.1127/0078-0421/2014/0042**

Bohaty, S.M., Uenzelmann-Neben, G., Childress, L.B., Archontikis, O.A., Batenburg, S.J., Bijl, P.K., Burkett, A.M., Cawthra, H.C., Chanda, P., Coenen, J.J., Dallanave, E., Davidson, P.C., Doiron, K.E., Geldmacher, J., Gürer, D., Haynes, S.J., Herrle, J.O., Ichiyama, Y., Jana, D., Jones, M.M., Kato, C., Kulhanek, D.K., Li, J., Liu, J., McManus, J., Minakov, A.N., Penman, D.E., Sprain, C.J., Tessin, A.C., Wagner, T., and Westerhold, T., 2023. Site U1579. In Uenzelmann-Neben, G., Bohaty, S.M., Childress, L.B., and the Expedition 392 Scientists, Agulhas Plateau Cretaceous Climate. Proceedings of the International Ocean Discovery Program, 392: College Station, TX (International Ocean Discovery Program). **https://doi.org/10.14379/iodp.proc.392.103.2023**

Bybell, L.M., and Self-Trail, J.M., 1994. Evolutionary, biostratigraphic, and taxonomic study of calcareous nannofossils from a continuous Paleocene-Eocene boundary section in New Jersey. U.S. Geological Survey Professional Paper, 1554. **http://pubs.er.usgs.gov/publication/pp1554**

Constable, C., and Tauxe, L., 1990. The bootstrap for magnetic susceptibility tensors. Journal of Geophysical Research: Solid Earth, 95(B6):8383–8395. **https://doi.org/10.1029/JB095iB06p08383**

Dunlop, D.J., and Özdemir, Ö., 1997. Rock Magnetism: Fundamentals and Frontiers: Cambridge, United Kingdom (Cambridge University Press). **https://doi.org/10.1017/CBO9780511612794**

Fisher, N.I., Lewis, T., and Embleton, B.J.J., 1987. Statistical Analysis of Spherical Data: Cambridge, United Kingdom (Cambridge University Press). **https://doi.org/10.1017/CBO9780511623059**

Fisher, R.A., 1953. Dispersion on a sphere. Proceedings of the Royal Society A: Mathematical, Physical and Engineering Sciences, 217(1130):295–305. **https://doi.org/10.1098/rspa.1953.0064**

Gradstein, F.M., Ogg, J.G., Schmitz, M.D., and Ogg, G.M. (Eds.), 2020. The Geologic Time Scale 2020: Amsterdam (Elsevier BV). **https://doi.org/10.1016/C2020-1-02369-3**

Hoernle, K., Hauff, F., van den Bogaard, P., Werner, R., Mortimer, N., Geldmacher, J., Garbe-Schönberg, D., and Davy, B., 2010. Age and geochemistry of volcanic rocks from the Hikurangi and Manihiki oceanic plateaus. Geochimica et Cosmochimica Acta, 74(24):7196–7219. **https://doi.org/10.1016/j.gca.2010.09.030**

Homrighausen, S., Hoernle, K., Hauff, F., Geldmacher, J., Wartho, J.-A., van den Bogaard, P., and Garbe-Schönberg, D., 2018. Global distribution of the HIMU end member: formation through Archean plume-lid tectonics. Earth-Science Reviews, 182:85–101. **https://doi.org/10.1016/j.earscirev.2018.04.009**

Jacques, G., Hauff, F., Hoernle, K., Werner, R., Uenzelmann-Neben, G., Garbe-Schönberg, D., and Fischer, M., 2019. Nature and origin of the Mozambique Ridge, SW Indian Ocean. Chemical Geology, 507:9–22. **https://doi.org/10.1016/j.chemgeo.2018.12.027**

Jelinek, V., 1981. Characterization of the magnetic fabric of rocks. Tectonophysics, 79(3–4):T63–T67. **https://doi.org/10.1016/0040-1951(81)90110-4**

Kahn, A., and Aubry, M.-P., 2004. Provincialism associated with the Paleocene/Eocene Thermal Maximum: temporal constraint. Marine Micropaleontology, 52(1–4):117–131. **https://doi.org/10.1016/j.marmicro.2004.04.003**

Kirschvink, J.L., 1980. The least-squares line and plane and the analysis of palaeomagnetic data. Geophysical Journal International, 62(3):699–718. **https://doi.org/10.1111/j.1365-246X.1980.tb02601.x**

Klein, C., Hurlbut, C.S., and Dana, J.D., 1993. Manual of Mineralogy, 21st edition: New York (Wiley).

Koppers, A.A.P., Sano, T., Natland, J.H., Widdowson, M., Almeev, R., Greene, A.R., Murphy, D.T., Delacour, A., Miyoshi, M., Shimizu, K., Li, S., Hirano, N., Geldmacher, J., and the Expedition 324 Scientists, 2010. Massive basalt flows on the southern flank of Tamu Massif, Shatsky Rise: a reappraisal of ODP Site 1213 basement units. In Sager, W.W., Sano, T., Geldmacher, J., and the Expedition 324 Scientists, Proceedings of the Integrated Ocean Drilling Program. 324: Tokyo (Integrated Ocean Drilling Program Management International, Inc.). **https://doi.org/10.2204/iodp.proc.324.109.2010**

Le Voyer, M., Hauri, E.H., Cottrell, E., Kelley, K.A., Salters, V.J.M., Langmuir, C.H., Hilton, D.R., Barry, P.H., and Füri, E., 2019. Carbon fluxes and primary magma CO_2 contents along the global mid-ocean ridge system. Geochemistry, Geophysics, Geosystems, 20(3):1387–1424. **https://doi.org/10.1029/2018GC007630**

Lurcock, P.C., and Wilson, G.S., 2012. PuffinPlot: a versatile, user-friendly program for paleomagnetic analysis. Geochemistry, Geophysics, Geosystems, 13(6):Q06Z45. **https://doi.org/10.1029/2012GC004098**

MacDonald, G.A., and Katsura, T., 1964. Chemical composition of Hawaiian lavas. Journal of Petrology, 5(1):82–133. **https://doi.org/10.1093/petrology/5.1.82**

Martini, E., 1971. Standard Tertiary and Quaternary calcareous nannoplankton zonation. Proceedings of the Second Planktonic Conference, Roma, 1970:739–785.

McFadden, P.L., and Reid, A.B., 1982. Analysis of palaeomagnetic inclination data. Geophysical Journal International, 69(2):307–319. **https://doi.org/10.1111/j.1365-246X.1982.tb04950.x**

Neumann, E.-R., Svensen, H., Galerne, C.Y., and Planke, S., 2011. Multistage evolution of dolerites in the Karoo large igneous province, central South Africa. Journal of Petrology, 52(5):959–984. **https://doi.org/10.1093/petrology/egr011**

Ogg, J.G., 2020. Geomagnetic Polarity Time Scale. In Gradstein, F.M., Ogg, J.G., Schmitz, M., and Ogg, G. (Eds.), Geologic Time Scale 2020. Amsterdam (Elsevier), 159–192. **https://doi.org/10.1016/B978-0-12-824360-2.00005-X**

Park, A.F., 1990. Contact (thermal) metamorphism. In Sen, G. (Ed.), Petrology: Principles and Practice. Boston, MA (Springer US), 106–108. **https://doi.org/10.1007/0-387-30845-8_42**

Pearce, M.A., 2000. Palynology and chemostratigraphy of the Cenomanian to lower Campanian chalk of southern and eastern England [PhD dissertation]. Kingston University, London. **https://eprints.kingston.ac.uk/id/eprint/20657/**

Perch-Nielsen, K., 1985. Mesozoic calcareous nannofossils. In Bolli, H.M., Saunders, J.B., and Perch-Nielsen, K. (Eds.), Plankton Stratigraphy (Volume 1). Cambridge, UK (Cambridge University Press), 329–426.

Philpotts, A.R., and Lewis, C.L., 1987. Pipe vesicles—an alternate model for their origin. Geology, 15(10):971–974. **https://doi.org/10.1130/0091-7613(1987)15<971:PVAMFT>2.0.CO;2**

Quirein, J.A., Gardner, J.S., and Watson, J.T., 1982. Combined natural gamma ray spectral/litho-density measurements applied to complex lithologies. Presented at the SPE Annual Technical Conference and Exhibition, New Orleans, LA, 26–29 September 1982. **https://doi.org/10.2118/11143-MS**

Self-Trail, J.M., Powars, D.S., Watkins, D.K., and Wandless, G.A., 2012. Calcareous nannofossil assemblage changes across the Paleocene–Eocene Thermal Maximum: evidence from a shelf setting. Marine Micropaleontology, 92–93:61–80. **https://doi.org/10.1016/j.marmicro.2012.05.003**

Shervais, J.W., 2022. The petrogenesis of modern and ophiolitic lavas reconsidered: Ti-V and Nb-Th. Geoscience Frontiers, 13(2):101319. **https://doi.org/10.1016/j.gsf.2021.101319**

Sissingh, W., 1977. Biostratigraphy of Cretaceous calcareous nannoplankton. Geologie en Mijnbouw, 56:37–65.
Skilling, I.P., White, J.D.L., and McPhie, J., 2002. Peperite: a review of magma–sediment mingling. Journal of Volcanology and Geothermal Research, 114(1–2):1–17. **https://doi.org/10.1016/S0377-0273(01)00278-5**
Tauxe, L., 2010. Essentials of Paleomagnetism: Oakland, CA (University of California Press).
Thomas, E., 2007. Cenozoic mass extinctions in the deep sea: what perturbs the largest habitat on Earth? In Monechi, S., Coccioni, R., and Rampino, M. (Eds.), Large Ecosystem Perturbations: Causes and Consequences. 424: (Special Paper - Geological Society of America). **https://doi.org/10.1130/2007.2424(01)**
Uenzelmann-Neben, G., Bohaty, S.M., Childress, L.B., Archontikis, O.A., Batenburg, S.J., Bijl, P.K., Burkett, A.M., Cawthra, H.C., Chanda, P., Coenen, J.J., Dallanave, E., Davidson, P.C., Doiron, K.E., Geldmacher, J., Gürer, D., Haynes, S.J., Herrle, J.O., Ichiyama, Y., Jana, D., Jones, M.M., Kato, C., Kulhanek, D.K., Li, J., Liu, J., McManus, J., Minakov, A.N., Penman, D.E., Sprain, C.J., Tessin, A.C., Wagner, T., and Westerhold, T., 2023a. Expedition 392 methods. In Uenzelmann-Neben, G., Bohaty, S.M., Childress, L.B., and the Expedition 392 Scientists, Agulhas Plateau Cretaceous Climate. Proceedings of the International Ocean Discovery Program, 392: College Station, TX (International Ocean Discovery Program). **https://doi.org/10.14379/iodp.proc.392.102.2023**
Uenzelmann-Neben, G., Bohaty, S.M., Childress, L.B., Archontikis, O.A., Batenburg, S.J., Bijl, P.K., Burkett, A.M., Cawthra, H.C., Chanda, P., Coenen, J.J., Dallanave, E., Davidson, P.C., Doiron, K.E., Geldmacher, J., Gürer, D., Haynes, S.J., Herrle, J.O., Ichiyama, Y., Jana, D., Jones, M.M., Kato, C., Kulhanek, D.K., Li, J., Liu, J., McManus, J., Minakov, A.N., Penman, D.E., Sprain, C.J., Tessin, A.C., Wagner, T., and Westerhold, T., 2023b. Expedition 392 summary. In Uenzelmann-Neben, G., Bohaty, S.M., Childress, L.B., and the Expedition 392 Scientists, Agulhas Plateau Cretaceous Climate. Proceedings of the International Ocean Discovery Program, 392: College Station, TX (International Ocean Discovery Program). **https://doi.org/10.14379/iodp.proc.392.101.2023**